AD-A188 690 PASSIVE AUTONOMOUS INFRARED SENSOR TECHNOLOGY(U) 1/2
HONEYWELL SYSTEMS AND RESEARCH CENTER MINNEAPOLIS MN
F SADJADI OCT 87 87SRC17 DAAL02-85-C-0134

UNCLASSIFIED F/G 17/5.1 NL

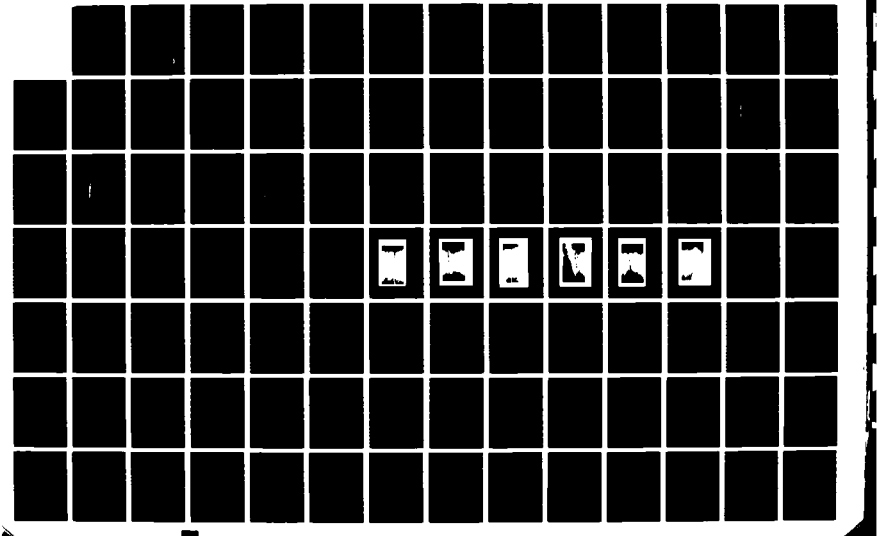

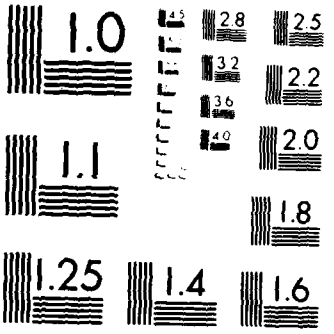

MICROCOPY RESOLUTION TEST CHART
NATIONAL BUREAU OF STANDARDS-1963-A

Passive Autonomous Infrared Sensor Technology

Final Report
Contract No. DAAL02-85-C-0134

October 1987

Prepared for

Defense Advanced Research Projects Agency (DoD)
US Army Center for Night Vision and Electro-Optics
Fort Belvoir, Virginia 22060

Prepared by

Honeywell
Systems and Research Center
3660 Technology Drive
P.O. Box 1361
MN65-2300
Minneapolis, Minnesota 55440

REPORT DOCUMENTATION PAGE

1a. REPORT SECURITY CLASSIFICATION Unclassified	1b. RESTRICTIVE MARKINGS –
2a. SECURITY CLASSIFICATION AUTHORITY –	3. DISTRIBUTION/AVAILABILITY OF REPORT
2b. DECLASSIFICATION/DOWNGRADING SCHEDULE –	
4. PERFORMING ORGANIZATION REPORT NUMBER(S) 87SRC17	5. MONITORING ORGANIZATION REPORT NUMBER(S)
6a. NAME OF PERFORMING ORGANIZATION Honeywell Systems and Research Center 6b. OFFICE SYMBOL (If applicable)	7a. NAME OF MONITORING ORGANIZATION US Army Center for Night Vision and Electro-Optics
6c. ADDRESS (City, State, and ZIP Code) 3660 Technology Drive, P.O. Box 1361 Minneapolis, Minnesota 55440	7c. ADDRESS (City, State, and ZIP Code) Fort Belvoir, Virginia 22060
8a. NAME OF FUNDING/SPONSORING ORGANIZATION Defense Advanced Research Projects Agency (DOD) 8b. OFFICE SYMBOL (If applicable)	9. PROCUREMENT INSTRUMENT IDENTIFICATION NUMBER Contract No. DAAL02-85-C-0134
8c. ADDRESS (City, State, and ZIP Code) Arlington, Virginia 22209-2308	10. SOURCE OF FUNDING NUMBERS PROGRAM ELEMENT NO. / PROJECT NO. / TASK NO / WORK UNIT ACCESSION NO
11. TITLE (Include Security Classification) Passive Autonomous Infrared Sensor Technology	
12. PERSONAL AUTHOR(S) Firooz Sadjadi	
13a. TYPE OF REPORT Final 13b. TIME COVERED FROM 8/9/85 TO 5/9/87	14. DATE OF REPORT (Year, Month, Day) 1987 October 15. PAGE COUNT 139
16. SUPPLEMENTARY NOTATION	

17 COSATI CODES		
FIELD	GROUP	SUB-GROUP

18. SUBJECT TERMS (Continue on reverse if necessary and identify by block number)

Artificial Intelligence
ATR Design
ATR Evaluations
Automatic Target Recognizer (ATR)
Background Adaptive Convexity Operator Region Extractor (BACORE)
Clutter Rejection
Computer Vision
(continued)

19. ABSTRACT (Continue on reverse if necessary and identify by block number)

This study was conducted in response to the DoD's need for establishing understanding of algorithm's modules for passive infrared sensors and seekers and establishing a standardized systematic procedure for applying this understanding to DoD applications. We quantified the performances of Honeywell's Background Adaptive Convexity Operator Region Extractor (BACORE) detection and segmentation modules, as functions of a set of image metrics for both single-frame and multiframe processing. We established an understanding of the behavior of the BACORE's internal parameters. We characterized several sets of stationary and sequential imagery and extracted TIR^2, $TBIR^2$, ESR, and range for each target. We generated a set of performance models for multi-frame processing BACORE that could be used to predict the behavior of BACORE in image metric space. A similar study was conducted for another of Honeywell's segmentors, namely Texture Boundary Locator (TBL), and its performances were quantified. Finally, a comparison of TBL and BACORE on the same data base and same number of frames was made.

20. DISTRIBUTION/AVAILABILITY OF ABSTRACT ☐ UNCLASSIFIED/UNLIMITED ☒ SAME AS RPT. ☐ DTIC USERS	21. ABSTRACT SECURITY CLASSIFICATION Unclassified
22a. NAME OF RESPONSIBLE INDIVIDUAL Firooz Sadjadi	22b. TELEPHONE (Include Area Code) 612-782-7543 22c. OFFICE SYMBOL

DD FORM 1473, 84 MAR

83 APR edition may be used until exhausted
All other editions are obsolete

18. Subject Terms (continued)

Detection
Forward-Looking Infrared
Image Metrics
Image Understanding
Performance Optimization
Segmentation
Texture-Based Segmentation
Texture Boundary Locator (TBL)

CONTENTS

CONTENTS (continued)

CONTENTS (concluded)

LIST OF ILLUSTRATIONS

LIST OF ILLUSTRATIONS (continued)

LIST OF ILLUSTRATIONS (continued)

LIST OF ILLUSTRATIONS (continued)

LIST OF ILLUSTRATIONS (concluded)

LIST OF TABLES

SECTION 1

INTRODUCTION

This is the Final Technical Report for the Passive Autonomous Infrared Sensor Technology Program, Contract No. DAAL02-85-C-0134. The report covers the investigation of two of Honeywell's detection and segmentation algorithms as applied to automatic target recognizers (ATRs). The contract period was from August 9, 1985 to May 9, 1987.

1.1 BACKGROUND

ATR technology is entering a crit . phase of the technology cycle. ATR functions are now being incorporated as a requirement in several defense systems like the Advanced Attack Helicopter (AAH), and Light Helicopter Experimental (LHX). These systems will impose increasingly demanding requirements on ATR performance.

During the course of ATR evolution, numerous algorithms have been developed and tested. However, the algorithms are limited to a very small scope of applications. Outside this limited scenario, many ATRs fail their performance requirements. For future systems, the ATR algorithms should be able to maintain optimal performance under a variety of applications, such as scenarios, environments, countermeasures, clutter density, and others.

For these reasons, the Defense Advanced Research Projects Agency (DARPA) has initiated an effort to establish an improved procedure with standards of measurement for investigating ATR algorithm performance.

The PAIRSTECH Project is part of this larger DARPA program that includes active infrared and MMW sensors, but as the name implies, the PAIRSTECH Project focuses on image processing in the thermal infrared, initially 8 to 12 μm for tactical air-to-ground applications.

1.2 PROBLEM DESCRIPTION

Two broad problems are addressed in the overall PAIRSTECH Project: 1) how to investigate the ATR as a whole and 2) how to evaluate the performance of ATRs on realistic and varied data to determine and compare both the capabilities and limits of the existing ATR systems. The first problem is addressed by breaking the ATR system into separate modules and investigating each module individually. The modules that were agreed upon by the ATR

community are detection, segmentation, feature extraction, and classification. The second problem was dealt with by:

- Characterizing images in terms of image metrics–Image metrics are a small set of parameters that are designed to capture the variations that exist among different images due to variations in targets, background sensor, and other parameters.

- Developing standard performance measure definitions, so that the performance of different ATR systems can be compared

- Tabulating the performance measures of each module in terms of image metrics

1.3 PROGRAM OBJECTIVES

This project mainly deals with the evaluation of only two modules from one of Honeywell's ATR systems: Multi-Target Acquisition Processor (MTAP). It is to be noted that MTAP is an integrated system that, when broken into different isolated modules like BACORE segmentation and detection, may produce suboptimum results.

The objectives of this contract were

- To evaluate Honeywell's Background Adaptive Convexity Operator Region Expander (BACORE) segmentor and post-segment Moving Target Detection (MTD), Multi-Target Tracking (MTT), and Archival Scene Model (ASM) as integral parts of BACORE multi-frame processing on real, ground-truthed FLIR data; to characterize data by image variables; to conduct a parametric investigation of the operators; to develop algorithm models; and to quantify algorithm performance by image variables

- To perform all of the necessary work to modify Honeywell's Texture Boundary Locator (TBL) segmentor software so that it interfaces and integrates with the BACORE subsystem; and to conduct comparative studies and experiments to evaluate the two segmentors under the same mission conditions (i.e., same image data, same number of frames)

Sections 2 through 6 address in detail these objectives. Section 2 of this report discusses the image metrics, the performance measures, and the data bases that were used in this investigation.

Section 3 describes the BACORE investigation. This includes both single-frame and sequential-frame experiments, and performance modeling.

Section 4 discusses the TBL investigations.

Section 5 presents a comparison of BACORE single-frame performance against the TBL performance results.

Section 6 presents the conclusion and a summary of the results.

1.4 KEY RESULTS

As mentioned above, the objectives of the PAIRSTECH Project were data characterization, performance evaluation for BACORE and TBL, modeling of BACORE, and comparison of TBL and BACORE on the same data bases and for the same number of frames. The data characterization task was the task of extracting image metrics from the imagery. The metrics that we used were those recommended by the ATRWG and ERIM, namely, target interference ratio squared (TIR^2), target-to-background interference ratio squared ($TBIR^2$), and edge strength ratio (ESR). The performance evaluation measures that were used again were those recommended by ATRWG and ERIM, namely, probability of detection, false alarm rate, and segmentation accuracy. Note that only the detection and segmentation modules of the MTAP were funded. The measure of segmentation accuracy was again the one that was recommended by ATRWG and ERIM, namely, the normalized areas of overlap between the segmented and the ground truthed targets.

The performance measures were obtained for detection and segmentation modules of both BACORE single-frame and multi-frame processors and the TBL algorithm.

For each frame of data, a set of performance plots as functions of TIR^2, $TBIR^2$, ESR, and range was obtained. Moreover, we quantized the metric space uniformly and tabulated the statistics of the performance measures for each metric bin.

What do all these data lead to? Using the available data from multi-frame BACORE, we generated models from performance measures as functions of image metrics and range. A refinement of these models can be used for predicting the behavior of BACORE in metric domains. It is conceivable that similar modeling could be done for TBL and single-frame BACORE.

As part of this project, we obtained insight into the behavior of BACORE algorithm parameters. The number of internal parameters that were sensitive to variations in imagery was found to be one-half of the original set. This will be useful in any future automatic setting of the parameters.

For the TBL, the extensive sensitivity analysis showed quantitatively that the performance of TBL (segmentation accuracy) can be effectively optimized by choosing a proper set of parameters. However, it was found that each target in the image has its own optimum set of parameters. This observation will be useful for any future use of TBL or for its improvement.

The overall performance values of TBL and BACORE single-frame processing were not impressive. The average segmentation accuracy was found to be around 0.35 out of a maximum of 1. This can be justified partly by the way in which ground truthing was done by ERIM, and partly by the way segmentation accuracy was defined.

The role of MTAP clutter rejection was shown to be dubious at best. Even though this module reduced FAR, it also diminished P_D to a large extent. In one data base (29-palm), it reduced P_D from 0.72 before clutter rejection to 0.02 after clutter rejection.

The BACORE multi-frame algorithm was found to be much better than single-frame BACORE and TBL. However, for multi-frame work, a different data base was used and ground truthing was done by us. In almost every category, BACORE algorithms outperformed TBL. However, for single-frame BACORE, these advantages were very small.

False alarm rate was found to be around 1 to 3 per frame for both multi- and single-frame BACORE after the clutter rejection module. However, before the clutter rejection, the value of FAR was very high.

In conclusion, PAIRSTECH has provided valuable information about the behavior of BACORE and TBL on relatively large and varied data bases. For the first time, we tabulated the performance measures as functions of image metrics. Image metrics are still a developing concept, and it remains to be seen what could be a good set of metrics to truly characterize varied imagery. As a result of funding limitations, we were not able to deeply analyze the wealth of information that we have gathered. It is crucial that the experience of PAIRSTECH be used in future designs of algorithms to create "better" ATRs or in the modification of existing algorithms.

SECTION 2

IMAGE METRICS, PERFORMANCE MEASURES, AND DATA BASES

2.1 IMAGE METRICS

The target metrics that we used were target interference ratio squared (TIR^2), target background interference ratio squared ($TBIR^2$), and edge strength ratio (ESR) as defined by ERIM. TIR^2 is defined as:

$$TIR^2 = \frac{\left(\frac{1}{N_o}\sum_{i=1}^{N_o} x_{oi} - \frac{1}{N_b}\sum_{i=1}^{N_b} x_{bi}\right)^2}{\frac{1}{N_b}\sum_{i=1}^{N_b} x_{bi}^2 - \left(\frac{1}{N_b}\sum_{i=1}^{N_b} x_{bi}\right)^2} = \frac{\left(\bar{x}_o - \bar{x}_b\right)^2}{\sigma_b^2} \tag{1}$$

where N_o = the number of pixels in the object

x_{oi} = the intensity level of the i-th pixel in the object

N_b = the number of pixels in the background

x_{bi} = the intensity level of the i-th pixel in the background

The background used in this computation is a local window around the minimum bounding rectangle of the target.

$TBIR^2$ is defined similarly:

$$TBIR^2 = \frac{\left(\bar{x}_o - \bar{x}_b\right)^2}{\sigma_o \cdot \sigma_b} \tag{2}$$

Edge strength ratio (ESR) is defined as the filtered, range-compensated Sobel operator output divided by local background variance.

2.2 PERFORMANCE MEASURES

For BACORE single-frame, BACORE multi-frame and TBL, a set of performance measures is defined that characterizes the desired measures in these algorithms. These are: probability of detection, false alarm rate (FAR), and segmentation accuracy.

Probability of detection (P_D) is defined as:

$$P_D = \frac{\text{Number of Ground Truth Targets Detected}}{\text{Number of Ground Truth Targets}} \quad (3)$$

False alarm rate (FAR) per frame performance is defined as:

$$\text{FAR Performance} = \frac{\text{Total Number of Clutter Regions Declared Target}}{\text{Total Number of Frames}} \quad (4)$$

Segmentation accuracy (SA) is defined as:

$$SA = \frac{\text{Number of Pixels of (Segmented Region Ground Truth Region)}}{\text{Number of Pixels of (Ground Truth) U (Segmented Region)}} \quad (5)$$

For BACORE, two sets of P_D and FAR can be defined; one set that is calculated at an early stage of the algorithm is referred to as region of interest (ROI) set, and the second set that is obtained at the output of segmentation and clutter rejection stage is referred to as post segment (PS) set. For TBL, since there is no ROI stage, only PS set is obtained.

2.3 DATA BASES

As part of the PAIRSTECH program, we had access to relatively large data bases, each exhibiting a wide spectrum of targets at various ranges, clutter conditions and viewing angles. The data bases that were used in our experiments were the following:

1. 29-Palm Data Base--This data base consisted of two different sets each containing 32 frames. There were about 184 targets in this data base.

2. Texas Instrument (TI) data base--This data base consisted of three different sets. Two of them contained 45 frames and the remaining one contained 46 frames. There was a total of 378 targets in this data base.

Both of these data bases have ground truth data available which consisted of the wireframe model of the targets at their appropriate locations on separate frames for every frame.

3. Texas Instrument Test Data Base--This data base consisted of 136 frames of unground truthed data.

4. 29-Palm Test Data Base--This data base consisted of 64 frames of unground truthed data.

The last two sets were used only to perform detection and segmentation test experiments. The results of these tests were submitted to ERIM for their evaluation experiments.

5. Honeywell MSN1712 Multi-Frame Data Base--This data base consisted of six sequences of multi-frame data. Each sequence had 20 frames each and six targets per frame, with the exception of sequence 5, which had five targets per frame. This data base was characterized and ground truthed manually by trained experts in our laboratory.

SECTION 3

BACORE INVESTIGATION

Honeywell's BACORE algorithm, shown schematically in Figure 3-1, is well documented in various reports elsewhere (Reference 1). However, for the sake of completeness, a brief description of BACORE is made in the next section.

3.1 A BRIEF DESCRIPTION OF BACORE

Figure 3-2 shows a more detailed description of detection and segmentation modules of BACORE, which are part of the BRITT statistical segmentation (BST) module of the Honeywell's BRITT/MTAP simulation.

The BST single-frame processing algorithm accepts as input an image, a range map and a set of control parameters, and generates as output a set of feature vectors that characterizes the bright convex segments which were detected by the algorithm. The algorithm is composed of a two-pass segmenter and a feature extractor. The segmenter developed in BRITT Phase I involves three operations: background adaption, a convexity operator, and region extraction, and is thus known as the BACORE segmenter. The first pass, which includes background adaption and the convexity operator, is generally referred to as "detection." Region extraction, the second pass, is generally referred to as "segmentation." Detection identifies rectangular subwindows of the full image that enclose convex bright regions. These regions are identified by virtue of the fact that they exhibit a locally focussed gradient within the region interior. This first pass produces regions of interest (ROI), general regions of an image upon which more analysis is performed during the second pass, segmentation. Segmentation extracts segments, each of which has an exact shape and outline, that correspond to the regions of interest located during detection.

The algorithm first performs subwindow selection and target size normalization, which can substantially reduce the throughput requirements of detection. Subwindow selection chooses a selected portion of the field of view for ROI detection on a rotating basis. During target size normalization the subwindow is undersampled (oversampled) to maintain approximately the same target size in pixels.

The next step is to detect ROI in the normalized subwindow. Locally-adaptive background subtraction is performed, which diminishes bland areas and enhances bright areas. (Note: The terms background adaption and background subtraction are used interchangeably; background "adaption" is achieved by subtracting out the background). This is followed by globally-adaptive bright and edge detection. Bright detection applies a fixed threshold to generate a bright image, and edge detection applies an eight-direction compass gradient operator to the background-subtracted image and thresholds the resulting image to form the edge image. The bright and edge images are logically ANDed together to form the bright/edge coincidence image. Then the convexity operator

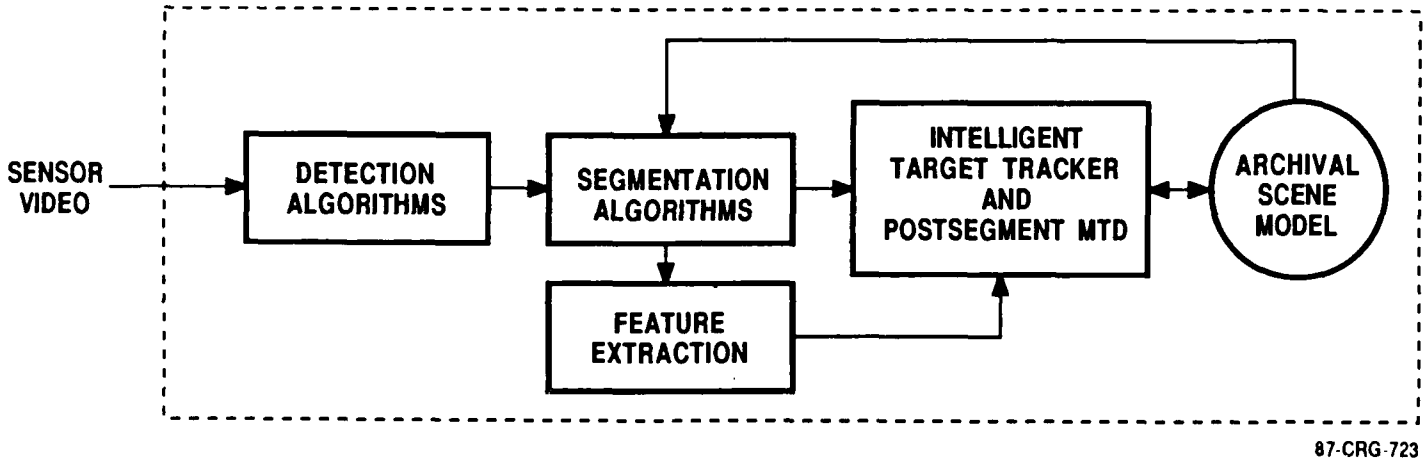

Figure 3-1. A Schematic Description of BACORE Subsystem Configuration

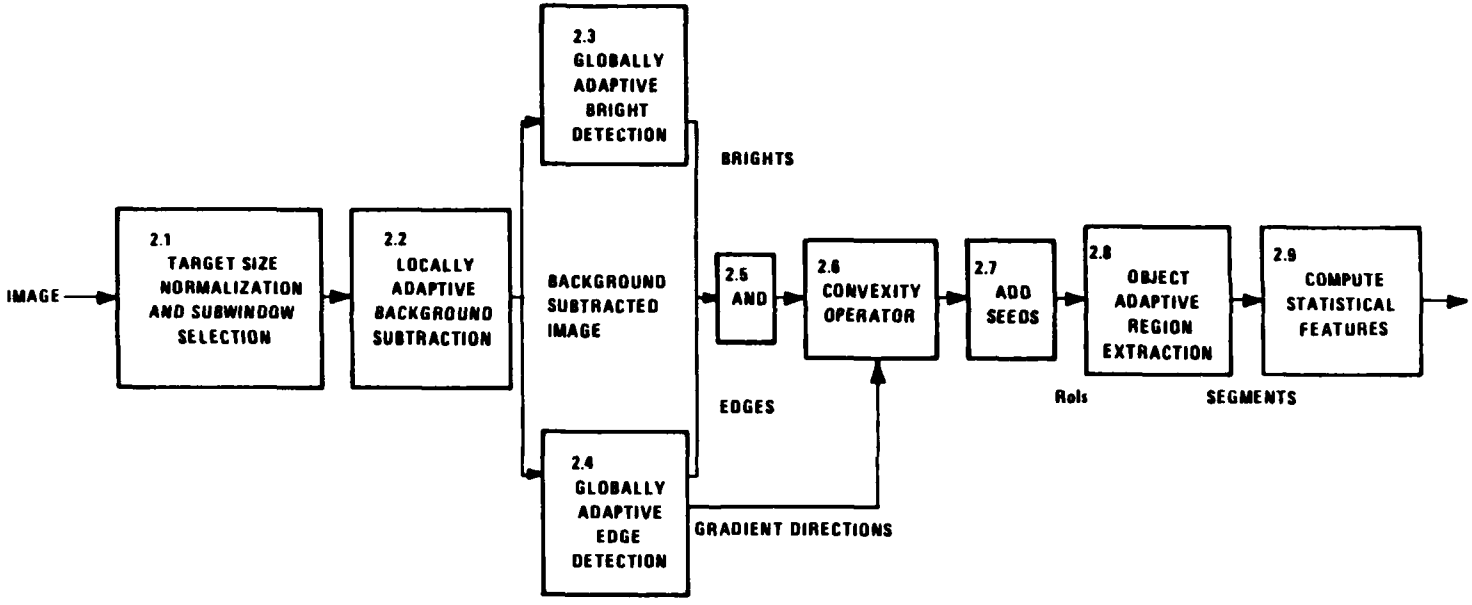

Figure 3-2. A Block Diagram of BST

detects convex regions by looking for areas where local gradients are focused and the segment size is comparable to a target size. Other ROI outside the subwindow are identified as stored from previous frames in the ASM. These positions are seeded into the ROI image output from detection, thus a full frame with all ROI is obtained.

The objective of region extraction is to define the exact shape and outline of the segments which correspond to the located ROI. The search for specific segment outlines uses a histogram approach that effectively considers all possible intensity thresholds within a window around the ROI, and chooses a "reasonable" one for determining the segment's shape based on gradients in the window. A minimum bounding rectangle is generated for each of the extracted segments, along with a chain-coded representation of the segment perimeter and a binary mask of the segment silhouette.

After the two-pass segmentation processing has finished, a set of statistical features that characterize each of the located segments is computed. This is accomplished by first calculating the moments through third order of both the intensity image and the binary image of the segment. The raw moments are then centralized and normalized, and finally a set of invariant moments is calculated that is independent of any translation, rotation, or scaling of the segment within the image plane.

The output of the BST is next fed to the single-frame clutter rejection module (SRJ). The purpose of the single-frame clutter rejection (SRJ) algorithm is to eliminate from further consideration those segments deemed to be clutter, by either a piece-wise linear (PWL) classifier or the combination of a PWL classifier and a Bayes classifier. The algorithm classifies a segment based on its associated feature vector in a feature vector file (produced by the BRITT statistics algorithm BST). This feature vectors consist of features extracted from segments segmented in the current frame only, hence, the term "single-frame." The segments determined to be clutters are eliminated from further processing by not passing their silhouettes from the input silhouette file (also produced by BST) to the output silhouette file. This is significant because the multi-target tracking (MTT) algorithm, following SRJ, will only track those segments whose silhouettes are found in output silhouette file.

Figure 3-3 demonstrates the functional flow of the SRJ package. In Figure 3-3 the archival scene model (ASM) is used to store the current frame feature vectors and silhouettes.

3.2 PERFORMANCE OF SINGLE-FRAME BACORE ON COMBINED TI AND 29-PALM DATA BASES

3.2.1 SA vs. TIR^2

Figure 3-4 shows the variations of SA as functions of TIR^2. In the first bin ($4 \times 10^{-6} \leq TIR^2 \leq 139$), SA has an average value of 0.37 and standard deviation of 0.24. In the second bin ($139 < TIR^2 \leq 277$), SA has an average value of 0.34

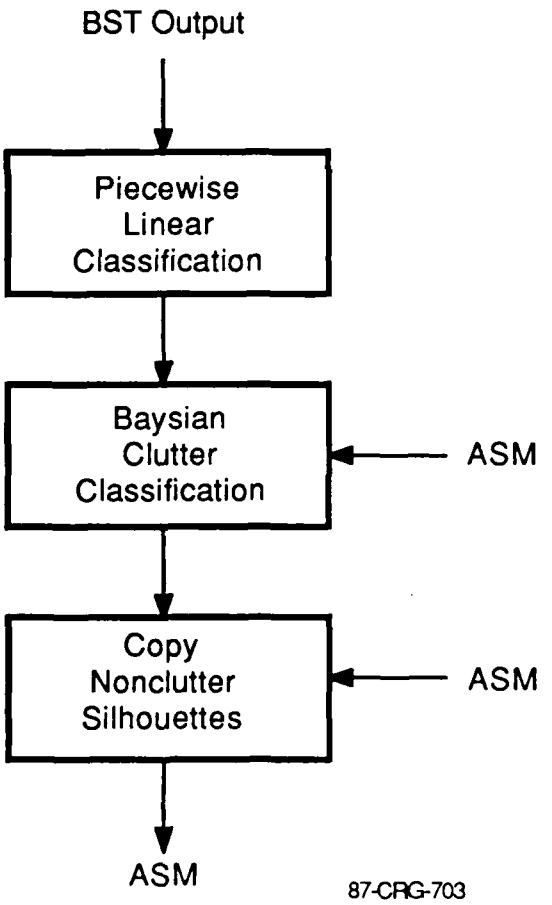

Figure 3-3. Functional Block Diagram of SRJ Processing

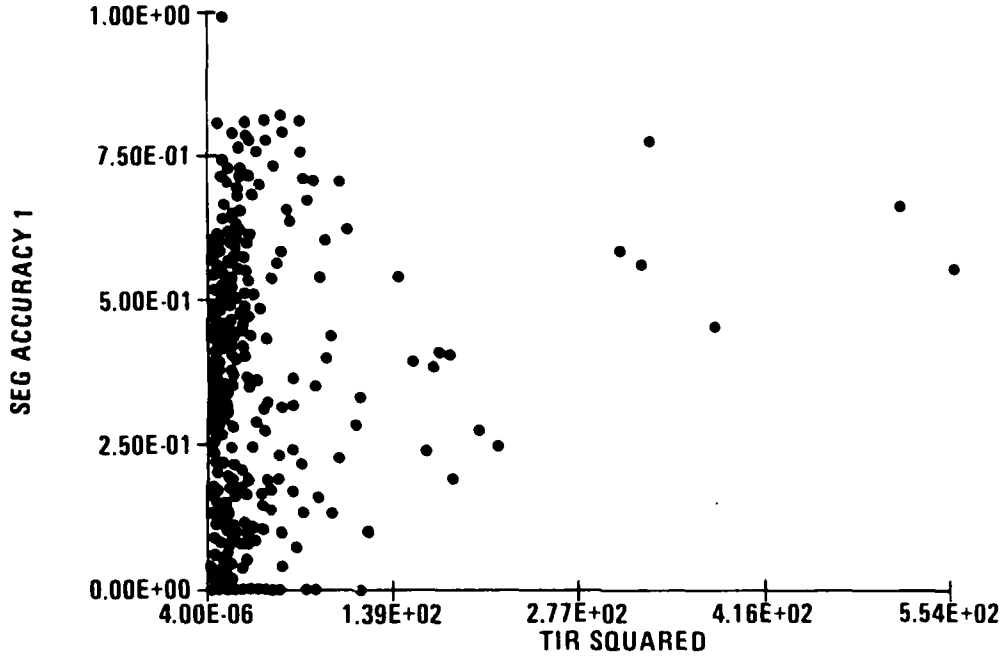

Figure 3-4. Segmentation Accuracy vs. TIR^2 (complete data set)–Full Range of TIR^2

and standard deviation of 0.10. In the third bin ($277<TIR^2\leq416$), SA has an average value of 0.59 and standard deviations of 0.11. In the fourth bin ($416<TIR^2\leq554$), SA has an average value of 0.61 and standard deviation of 0.05. By expanding the range of TIR^2 between 0 and 150, furthermore, as shown in Figure 3-5, one obtains the following. In the first sub-bin ($0\leq TIR^2\leq37.5$), SA has an average value of 0.36 and standard deviation of 0.24. In the second sub-bin ($37.5<TIR^2\leq75$), SA has an average value of 0.42 and standard deviation of 0.26. In the third sub-bin ($75<TIR^2\leq113$), SA has a average value of 0.42 and standard deviation of 0.18. In the fourth sub-bin ($113<TIR^2\leq150$), SA has an average value of 0.32 and standard deviation of 0.22.

3.2.2 SA vs. $TBIR^2$

Figure 3-6 shows the variation of SA as a function of $TBIR^2$. In the first bin ($3x10^{-6}\leq TBIR^2\leq25.5$), SA has an average value of 0.37 and a standard deviation of 0.24. In the second bin ($25.5<TBIR^2\leq51.1$), SA has an average value of 0.45 and a standard deviation of 0.17. In the third bin ($51.1<TBIR^2\leq76.6$), there are no samples. In the fourth bin ($76.6<TBIR^2\leq102$), there is only one sample which has a SA value of 0.25. By expanding the region between 0 and 25, as shown in Figure 3-7, one obtains the following results. In the first sub-bin ($0\leq TBIR^2\leq6.25$), SA has an average value of 0.30 and standard deviation of 0.22. In the second sub-bin ($6.25<TBIR^2\leq12.5$), SA has an average value of 0.51 and standard deviation of 0.22. In the third sub-bin ($12.5<TBIR^2\leq18.8$), SA has an average value of 0.55 and standard deviation of 0.19. Finally, in the fourth sub-bin ($18.8<TBIR^2\leq25.0$), SA has an average value of 0.53 and standard deviation of 0.14.

3.2.3 SA vs. ESR

Figure 3-8 shows the variation of SA as a function of ESR. In the first bin ($9.44x10\leq ESR\leq1810$), SA has an average value of 0.37 and standard deviation of 0.24. In the second bin ($1810\leq ESR\leq3620$), SA has an average value of 0.28 and standard deviation of 0.09. In the third bin ($3620<ESR\leq5420$), SA has an average value of 0.51 and standard deviation of 0.05. In the fourth bin ($5420<ESR\leq7230$), SA has an average value of 0.66 and standard deviation of 0.09. By expanding the ESR region between 0 to 1500, furthermore, as shown in Figure 3-9, one obtains the following results. In the first sub-bin ($0\leq ESR\leq375$), SA has an average value of 0.35 and standard deviation of 0.24. In the second sub bin ($375<ESR\leq750$), SA has an average value of 0.44 and standard deviation of 0.24. In the third sub-bin ($750<ESR\leq1130$), SA has an average value of 0.41 and standard deviation of 0.22. Finally, in the fourth sub-bin ($1130<ESR\leq1500$), SA has an average value of 0.48 and standard deviation of 0.21.

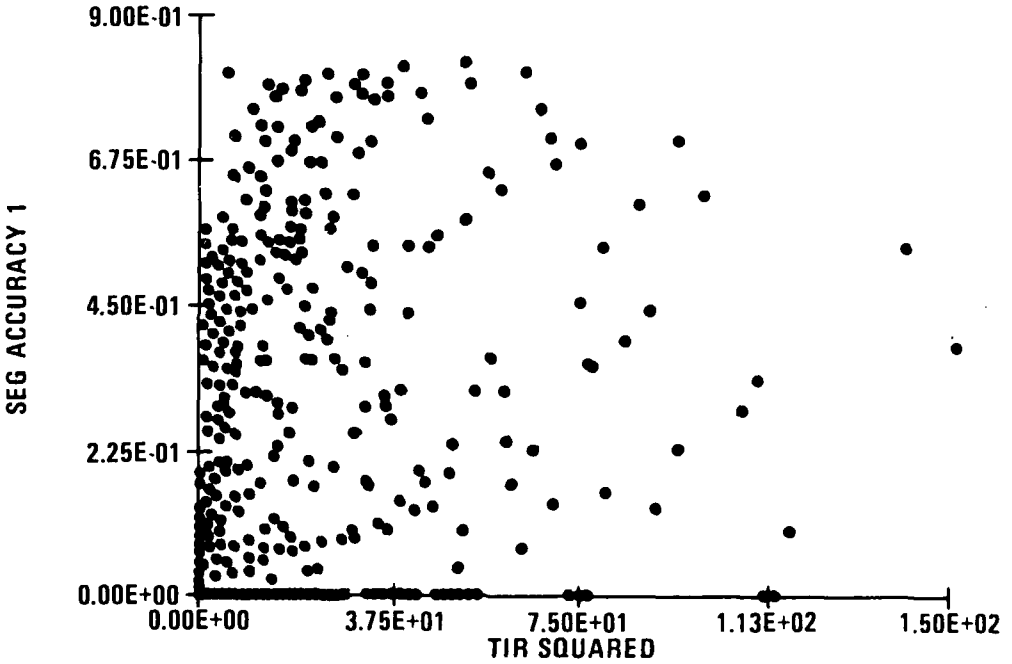

Figure 3-5. Segmentation Accuracy vs. TIR^2 (complete data set)–Subset of TIR^2

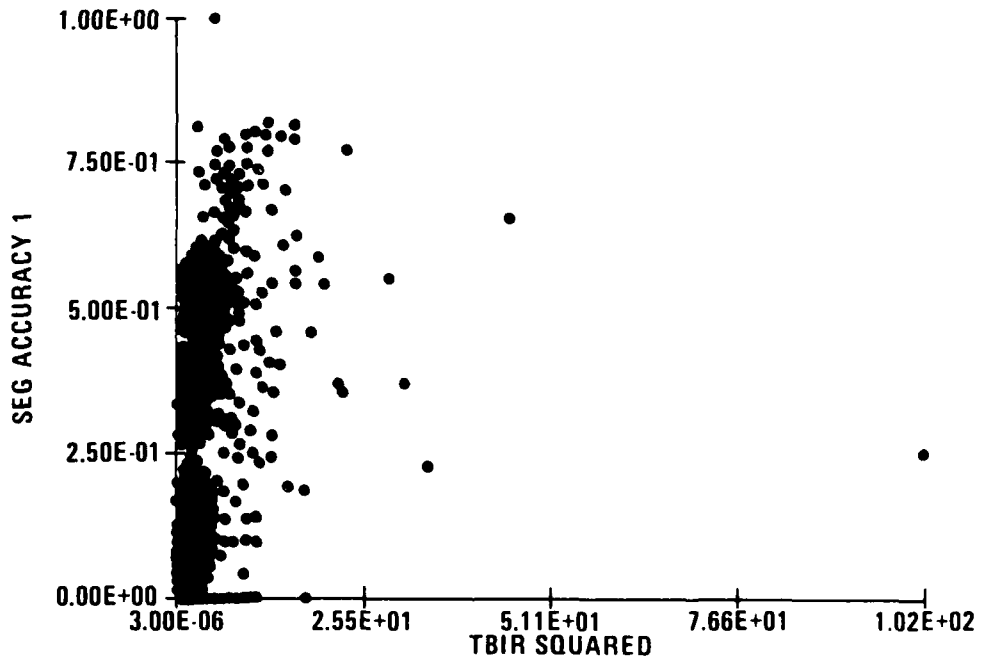

Figure 3-6. Segmentation Accuracy vs. $TBIR^2$ (complete data set)–Full Range of $TBIR^2$

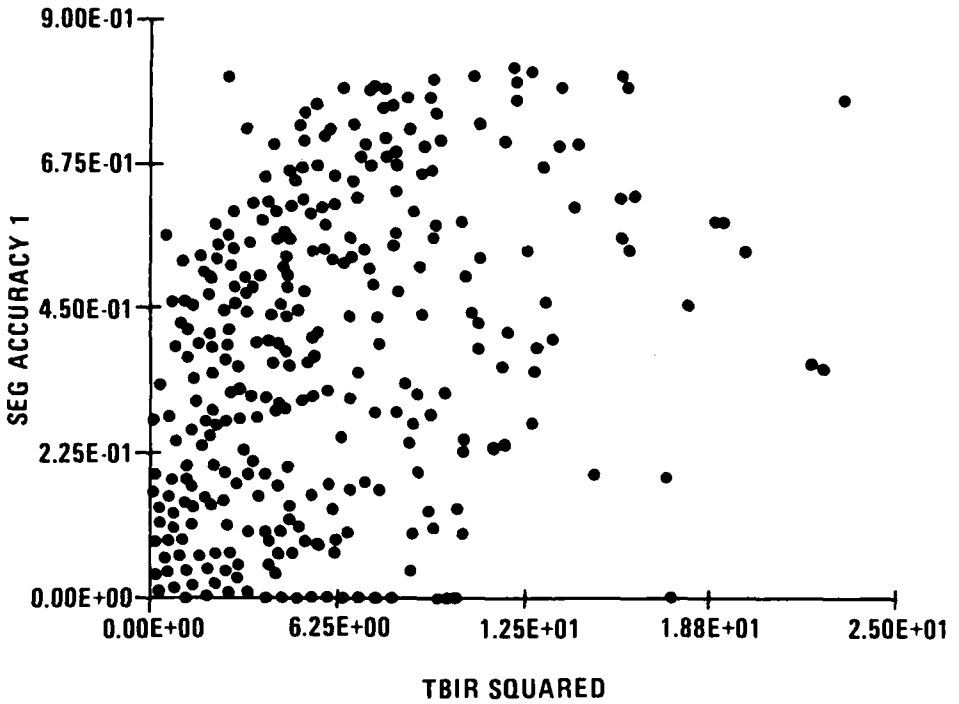

Figure 3-7. Segmentation Accuracy vs. $TBIR^2$ (complete data set)–Subset of $TBIR^2$

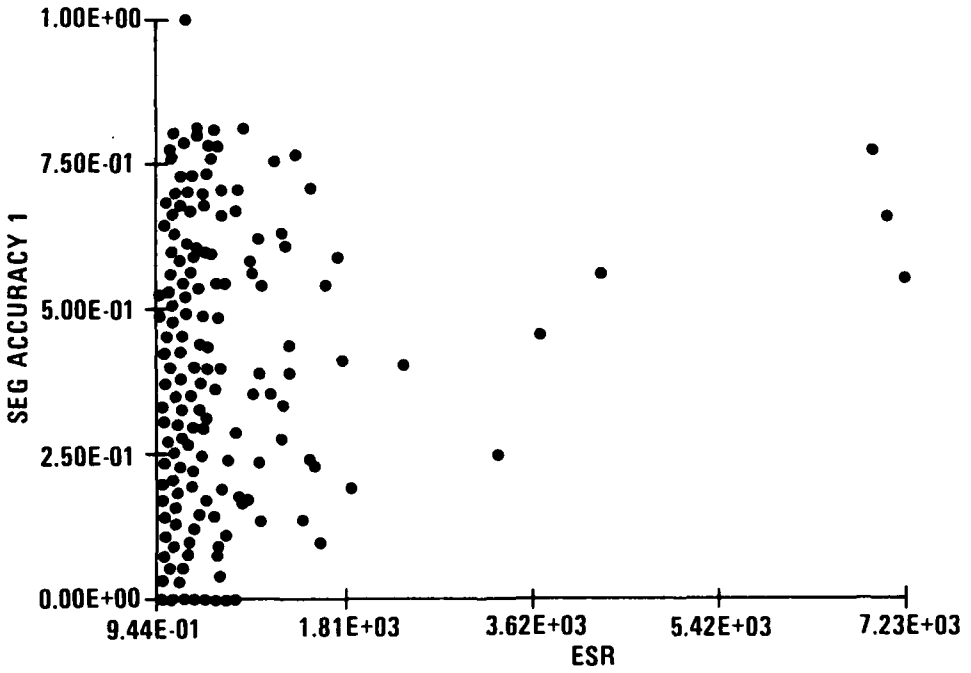

Figure 3-8. Segmentation Accuracy vs. ESR (complete data set)–Full Range of ESR

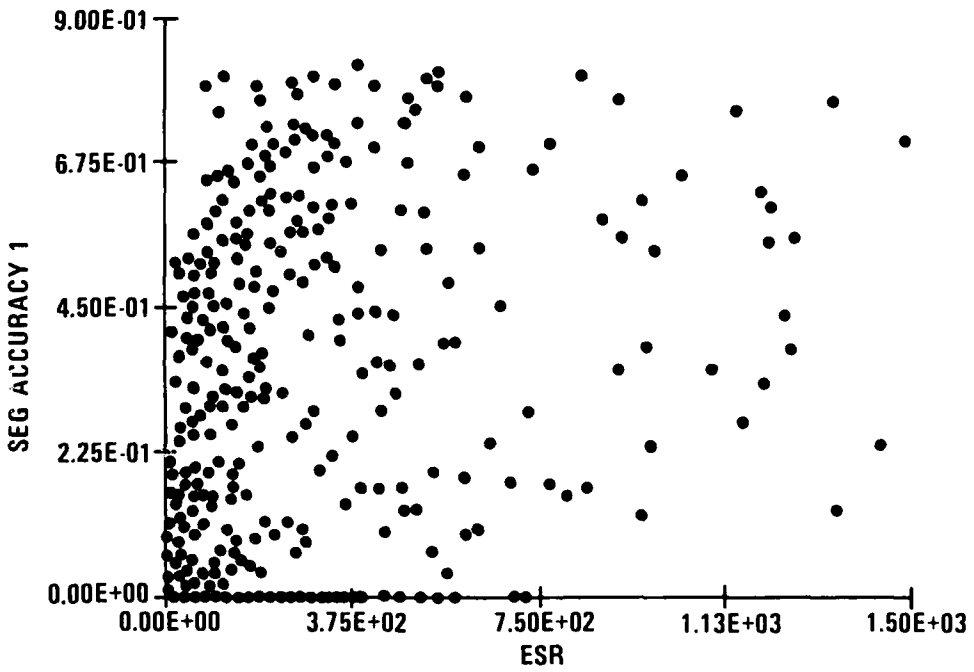

Figure 3-9. Segmentation Accuracy vs. ESR (complete data set)–Subset of ESR

3.2.4 SA vs. Range

Figure 3-10 shows the variation of SA as a function of range. SA attains its highest value of 1.0 at the range value of 7710 and then drops to around 0.8 at the range value of 10100.

3.2.5 P_D (ROI) vs. TIR^2

Figure 3-11 shows the variation of P_D (ROI) as a function of TIR^2. As TIR^2 increases, P_D tends to increase and attains the value of 1 for all TIR^2 values higher than 100.

3.2.6 P_D (ROI) vs. $TBIR^2$

Figure 3-12 shows the variation of P_D (ROI) as a function of $TBIR^2$. As $TBIR^2$ increases, P_D tends to increase and attains the value of 1 for all $TBIR^2$ values larger than 15.

3.2.7 P_D (ROI) vs. ESR

Figure 3-13 shows the variations of P_D (ROI) as a function of ESR. As ESR increases, P_D tends to increase and attains the value of 1 for all ESR values larger than 1000.

3.2.8 P_D (ROI) vs. Range

Figure 3-14 shows variation of P_D (ROI) as a function of range. As range increases, average P_D tends to increase and attains value of 1 at range values of 4900 to 7700. Then it tends to decrease.

3.2.9 P_D (post segment) vs. TIR^2

Figure 3-15 shows variation of P_D (post segment) as a function of TIR^2. As TIR^2 increases P_D tends to increase and attains value of 1 for all TIR^2 values larger than 130.

3.2.10 P_D (post segment) vs. $TBIR^2$

Figure 3-16 shows variation of P_D (post segment) as a function of $TBIR^2$. As $TBIR^2$ increases P_D tends to increase and attains value of 1 for all values of $TBIR^2$ larger than 20.

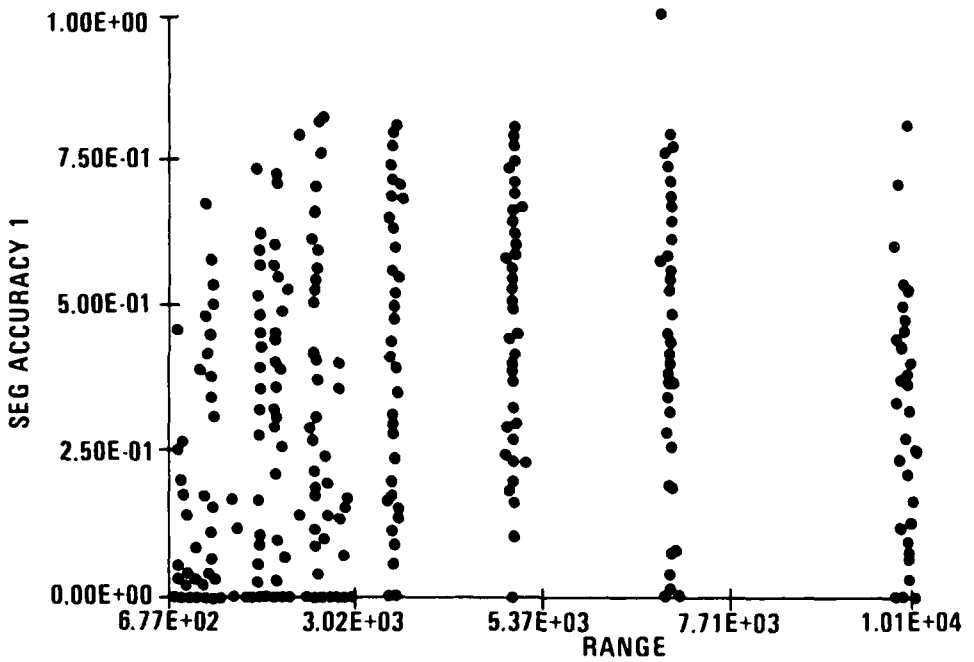

Figure 3-10. Segmentation Accuracy vs. Range in Meters (complete data set)

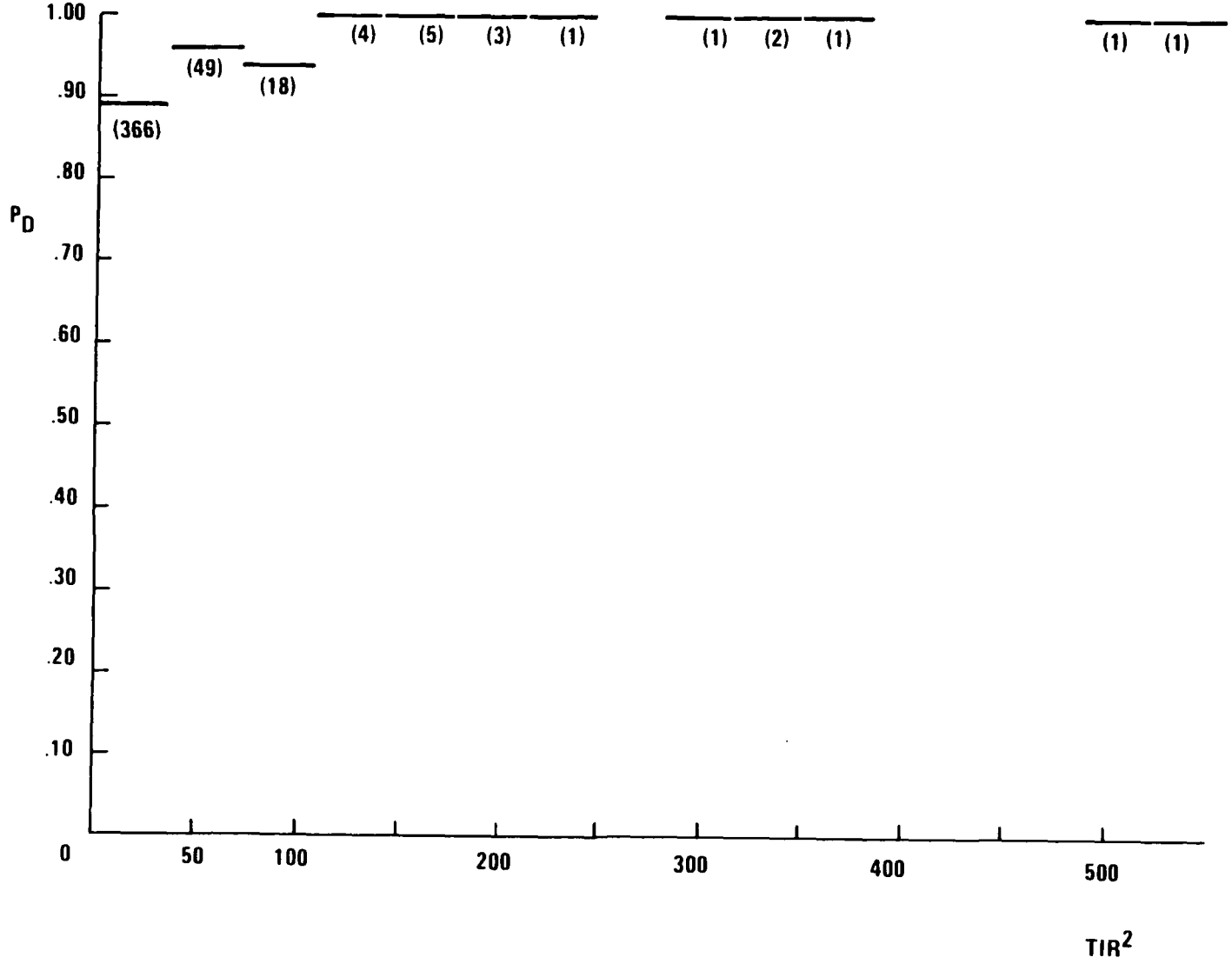

Figure 3-11. ROI P_D vs. TIR^2 (complete data set) 87-CRG-575

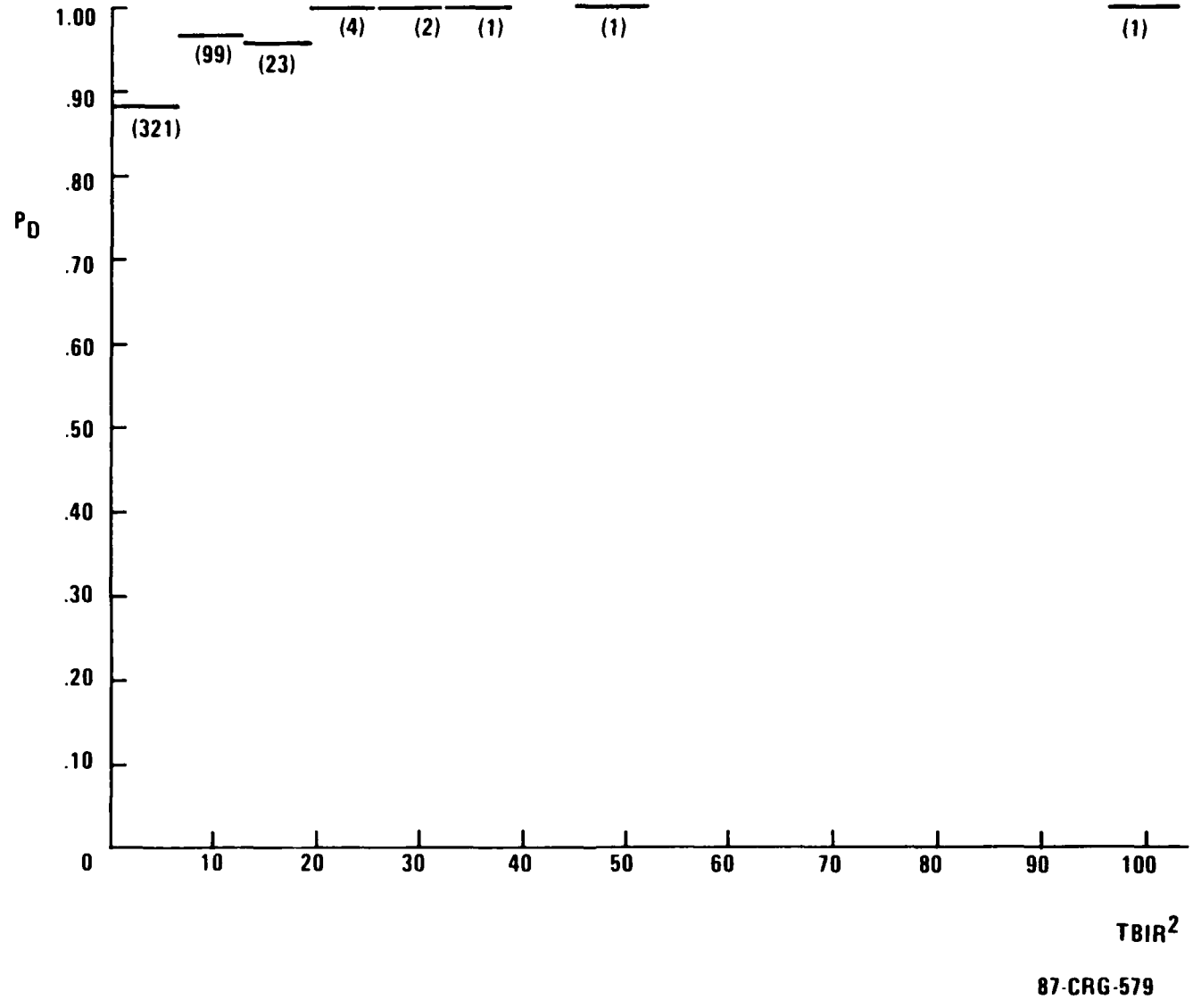

Figure 3-12. ROI P_D vs. $TBIR^2$ (complete data set)

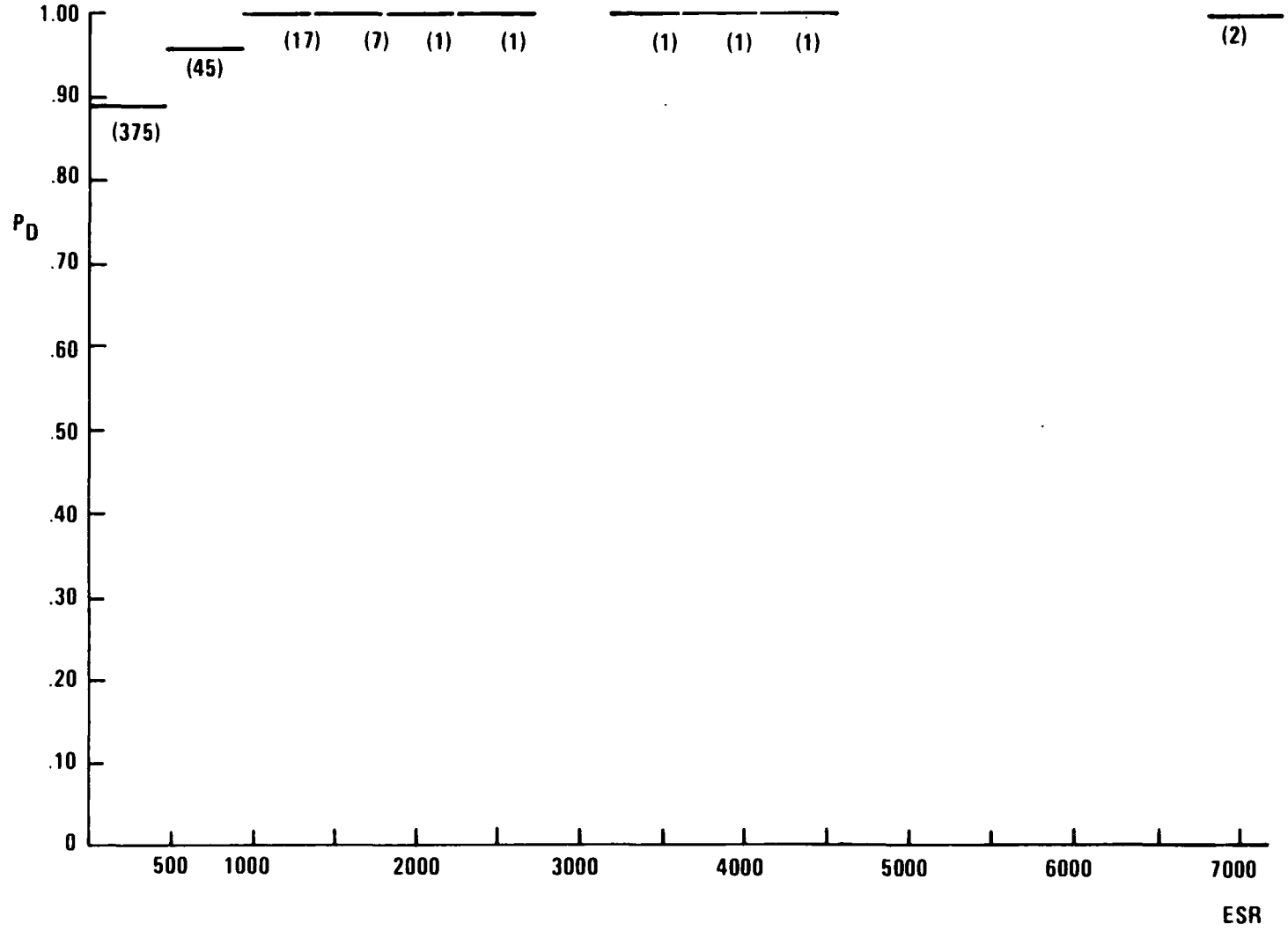

Figure 3-13. ROI P_D vs. ESR (complete data set)

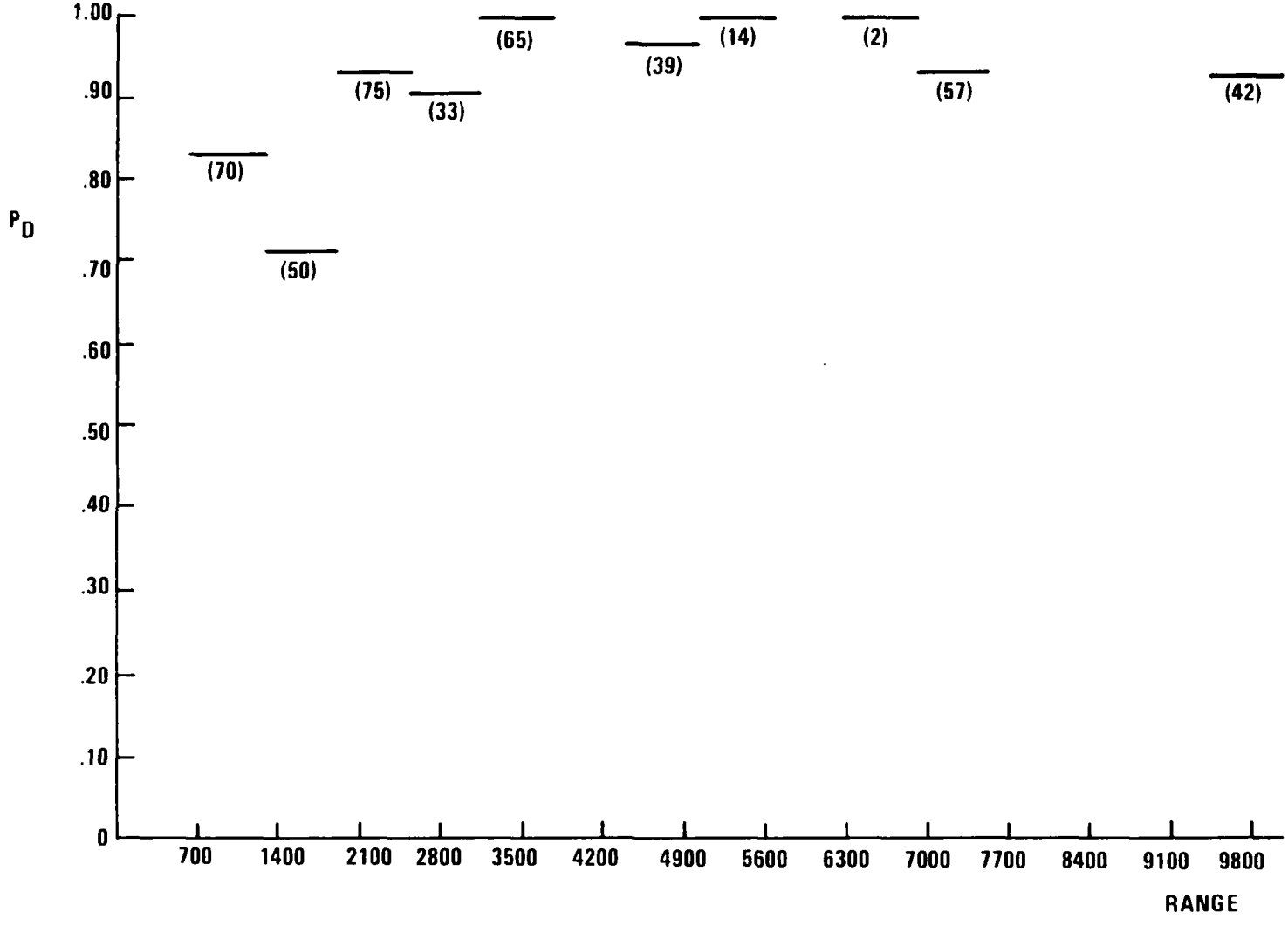

Figure 3-14. ROI P_D vs. Range (complete data set)

87-CRG-587

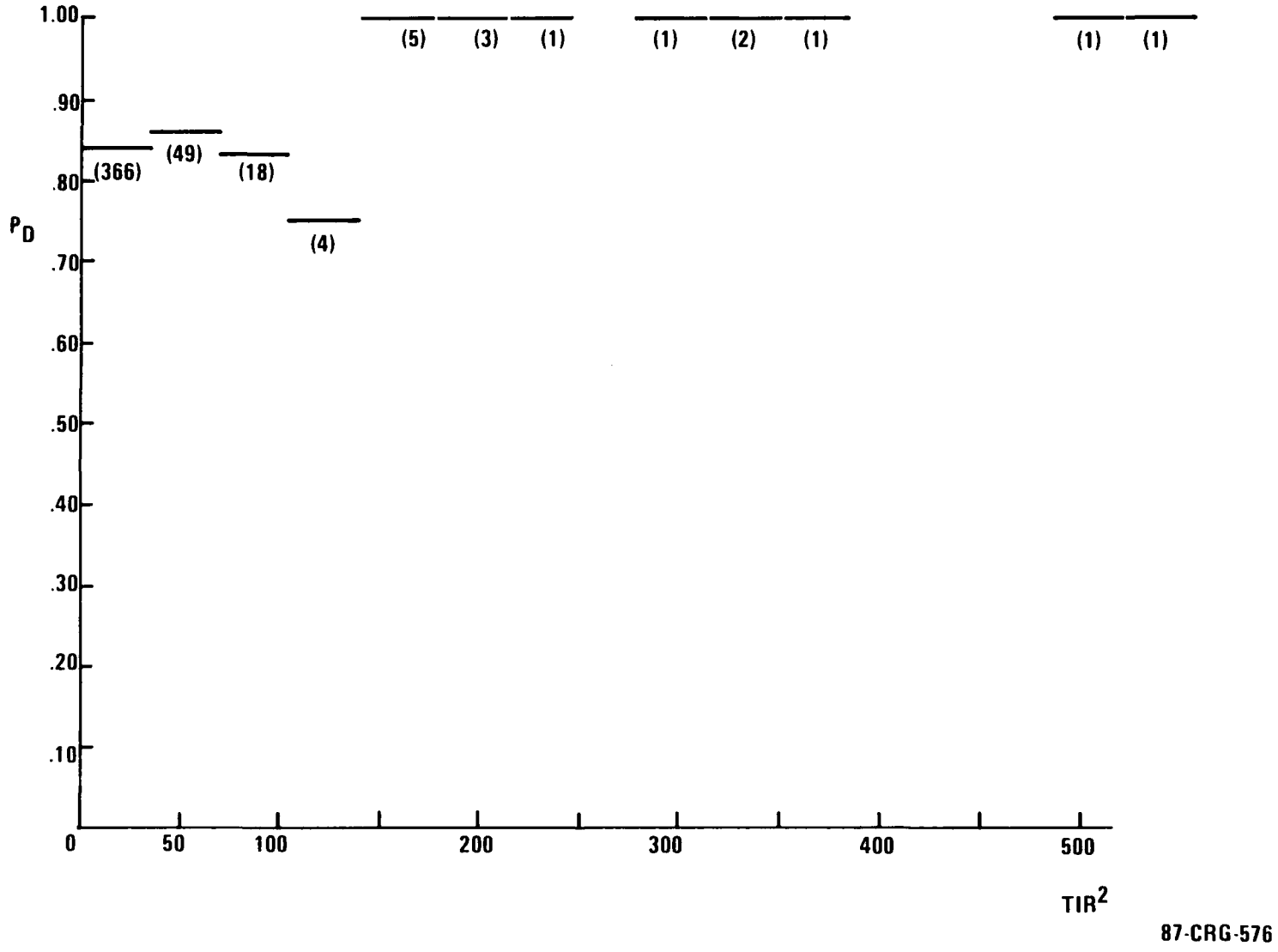

Figure 3-15. Segmentation P_D vs. TIR^2 (complete data set)

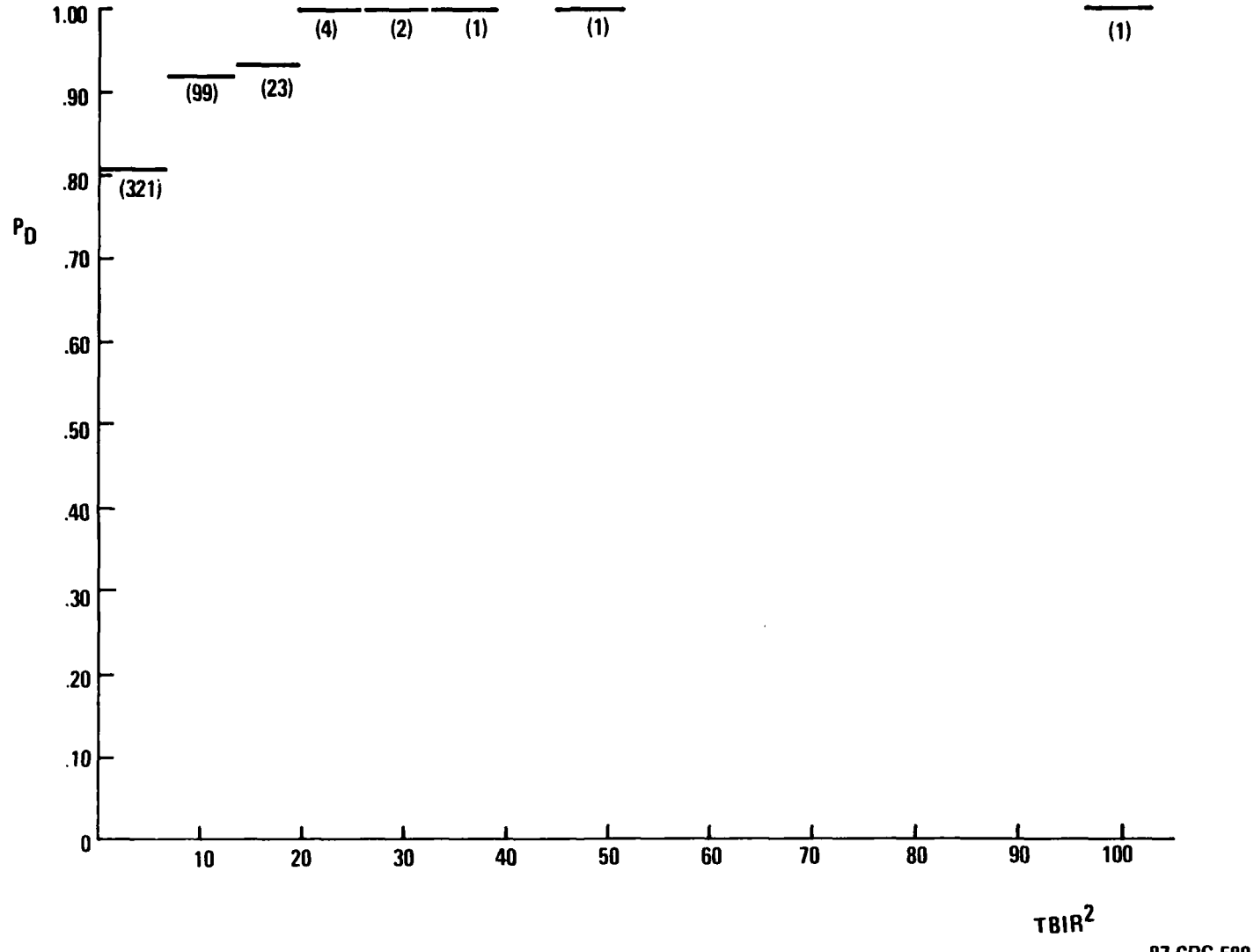

Figure 3-16. Segmentation P_D vs. $TBIR^2$ (complete data set)

3.2.11 P_D (post segment) vs. ESR

Figure 3-17 shows variation of P_D (post segment) as a function of ESR. As ESR increases P_D tends to increase and attains a value of 1 for all values of ESR larger than 1000.

3.2.12 P_D (post segment) vs. Range

Figure 3-18 shows variation of P_D (post segment) as a function of range. Average P_D tend to increase a range increases. It attains a value of 1 at range values betw n 4900 to 7700. Then it tends to decrease.

3.2.13 P_D (post segment and clutter rejection) vs. TIR^2

Figure 3-19 shows variation of P_D (post segment and clutter rejection) as a function of TIR^2. As TIR^2 increases, P_D increases and attains a value of 1 for all TIR^2 greater than 150.

3.2.14 P_D (post segment and clutter rejection) vs. $TBIR^2$

Figure 3-20 shows variation of P_D (post segment and clutter rejection as a function of $TBIR^2$. As $TBIR^2$ increases P_D tends to increase and attains a value of 1 for all values of $TBIR^2$ larger than 20.

3.2.15 P_D (post segment and clutter rejection) vs. ESR

Figure 3-21 shows variation of P_D as a function of ESR. As ESR increases, P_D tends to increase and attains a value of 1 for all values of ESR larger than 1800.

3.2.16 P_D (post segment and clutter rejection) vs. Range

Figure 3-22 shows variation of P_D as a function of range. As range increases average P_D tends to increase and attains its highest average value of 1 for range values between 4900 and 7300. Then it decreases.

3.3 PERFORMANCE OF BACORE MULTI-FRAME PROCESSING ALGORITHM VS. METRICS

We processed six sequential data sets, 20 frames each, from the MSN1712 Honeywell data base. Figures 3-23 to 3-28 show a set of representative frames from each of the six sequences. The image metrics TIR^2, $TBIR^2$ and ESR have been computed on every frame. The ground truthing necessary in computing these metrics was performed by a trained operator.

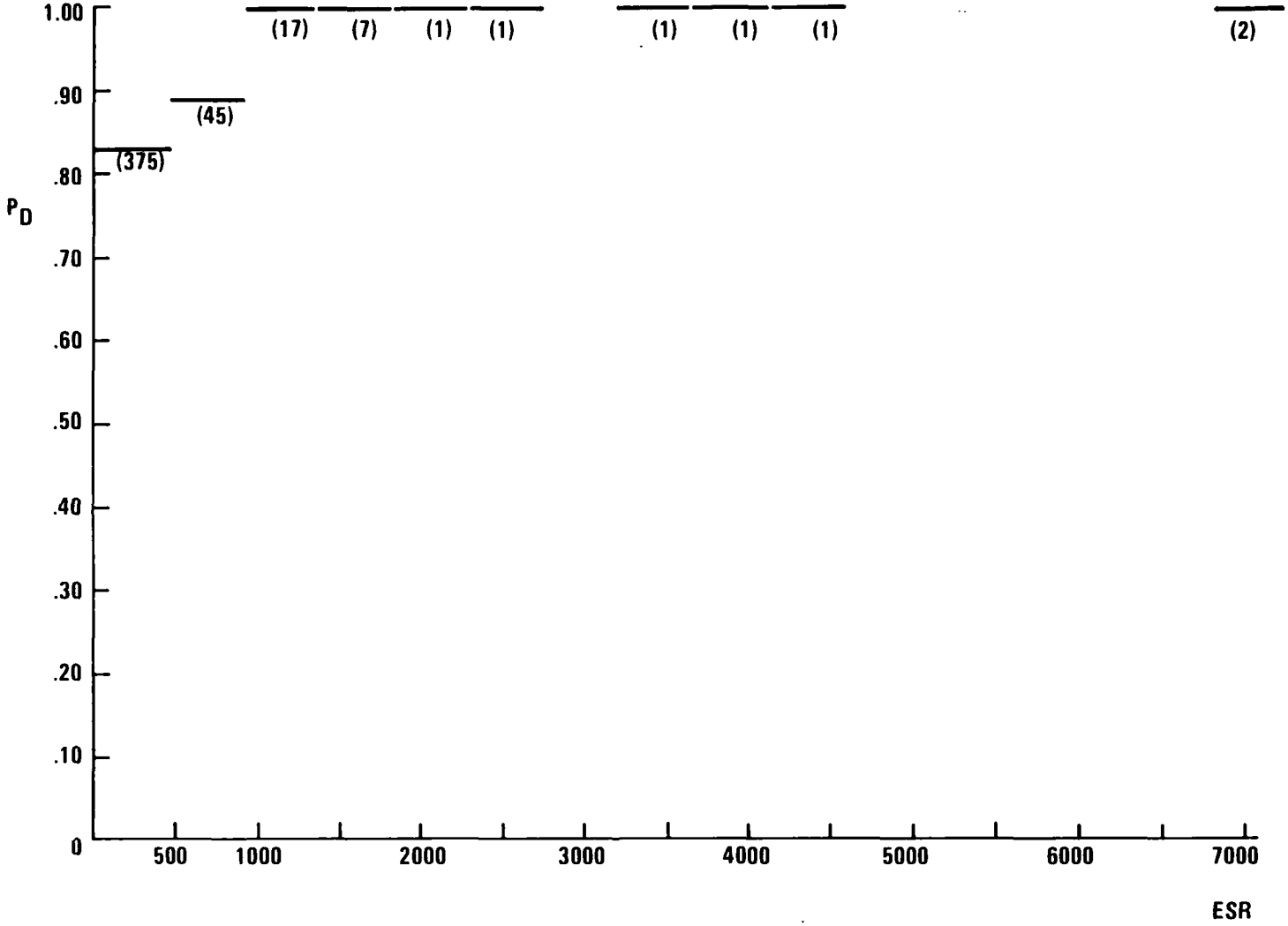

Figure 3-17. Segmentation P_D vs. ESR (complete data set)

87-CRG-584

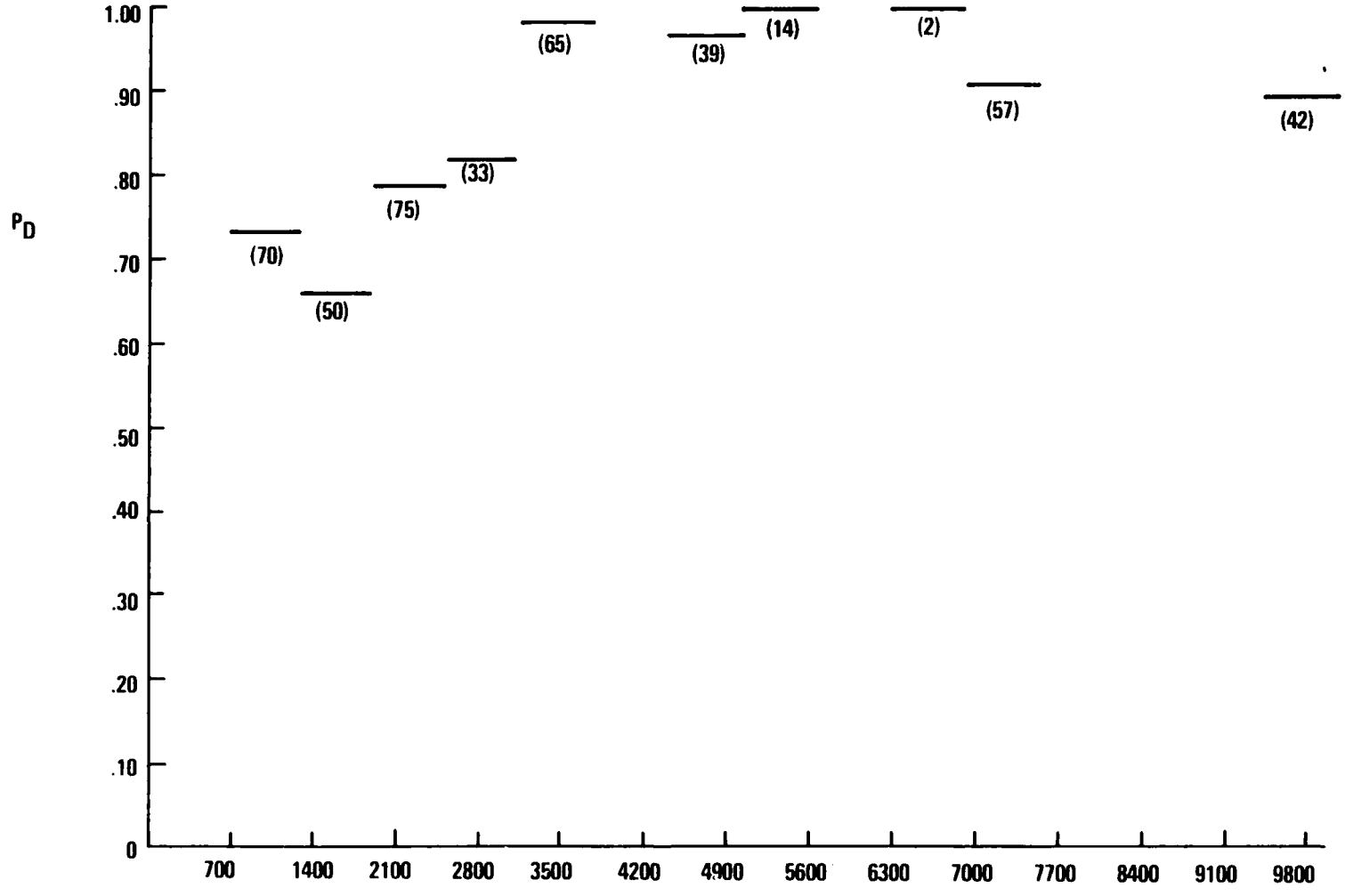

Figure 3-18. Segmentation P_D vs. Range in Meters (complete data set)

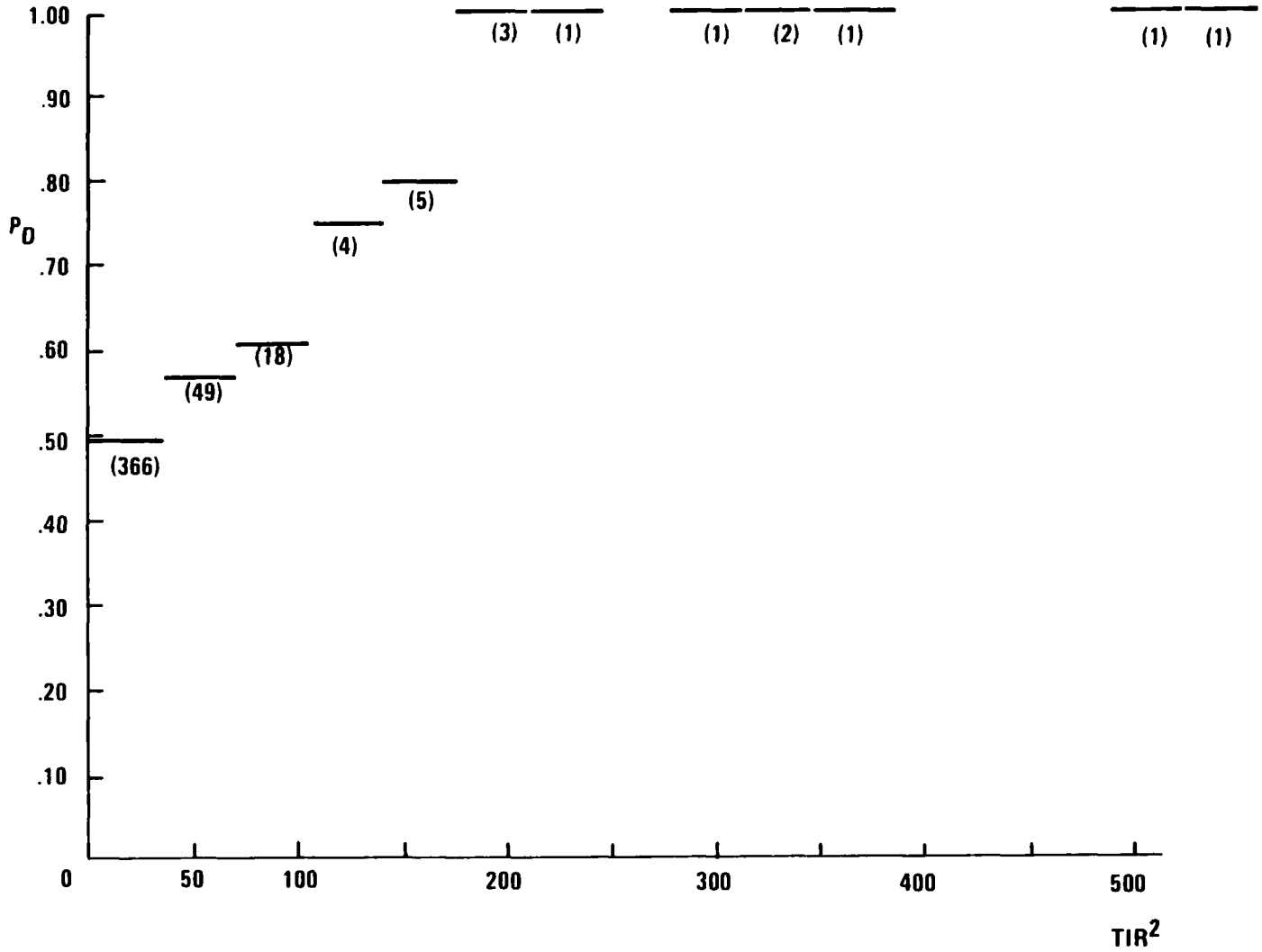

Figure 3-19. Post Clutter Rejection P_D vs. TIR^2 (complete data set) 87-CRG-577

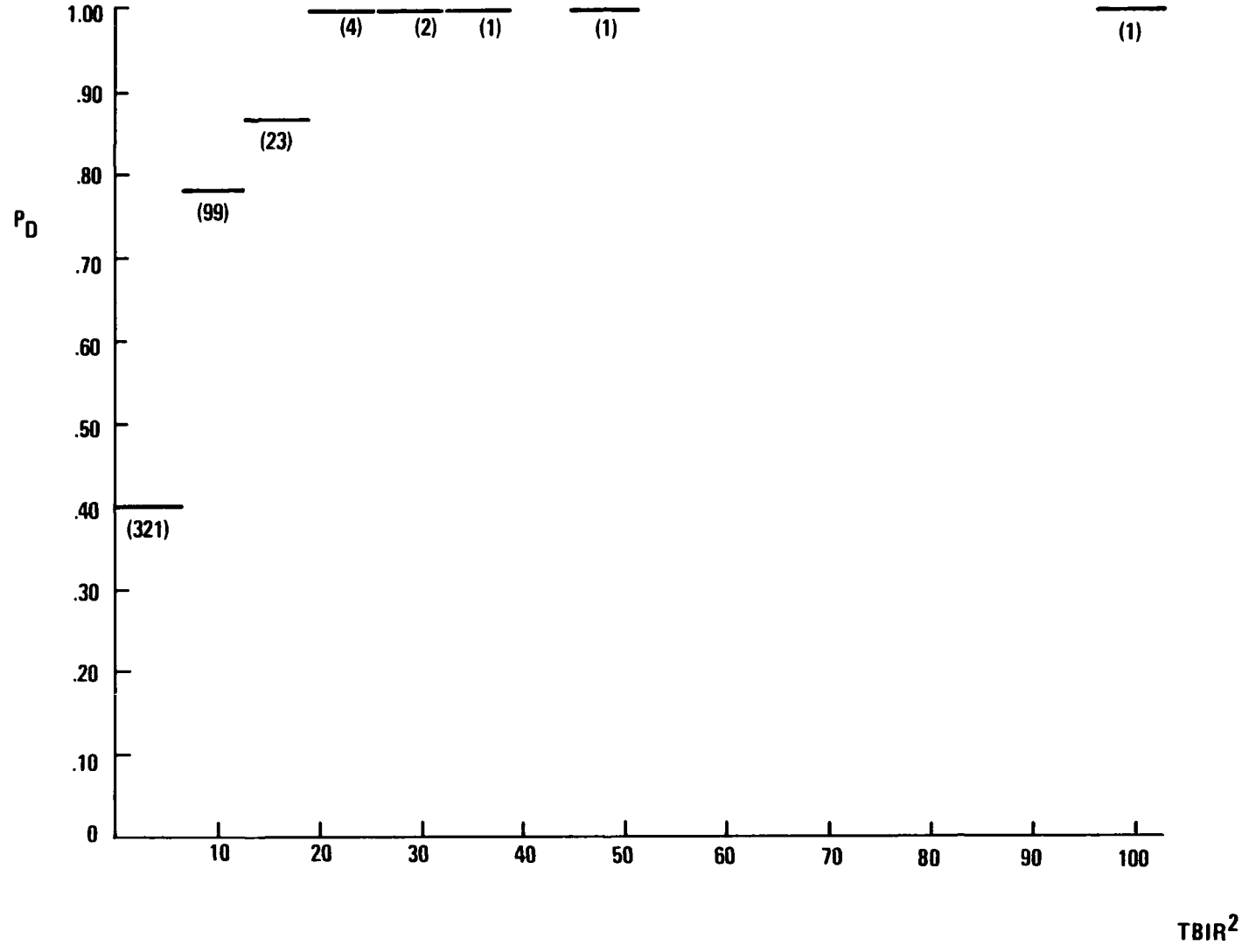

Figure 3-20. Post Clutter Rejection P_D vs. $TBIR^2$ (complete data set) 87-CRG-581

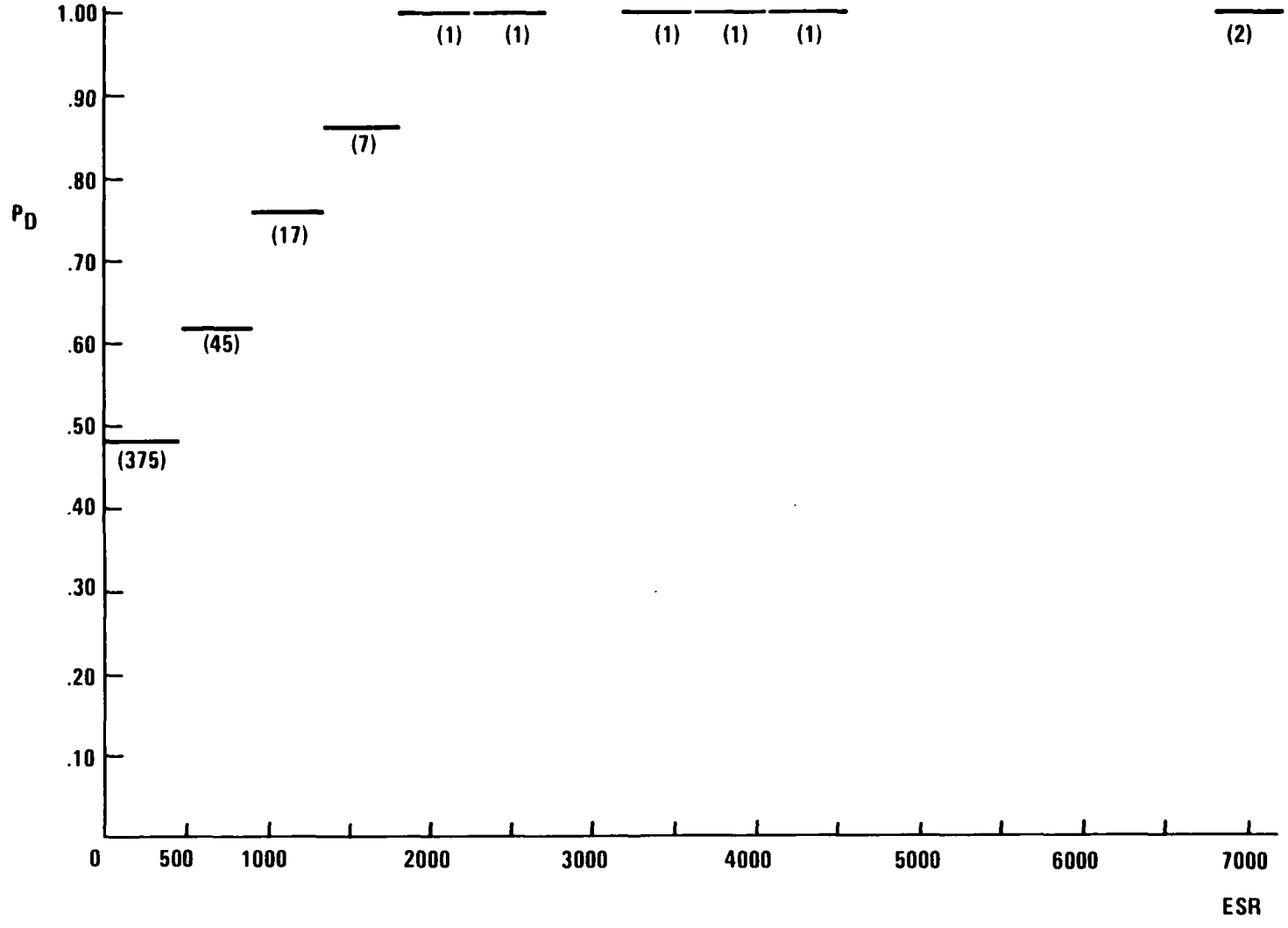

Figure 3-21. Post Clutter Rejection P_D vs. ESR (complete data set)

87-CRG-585

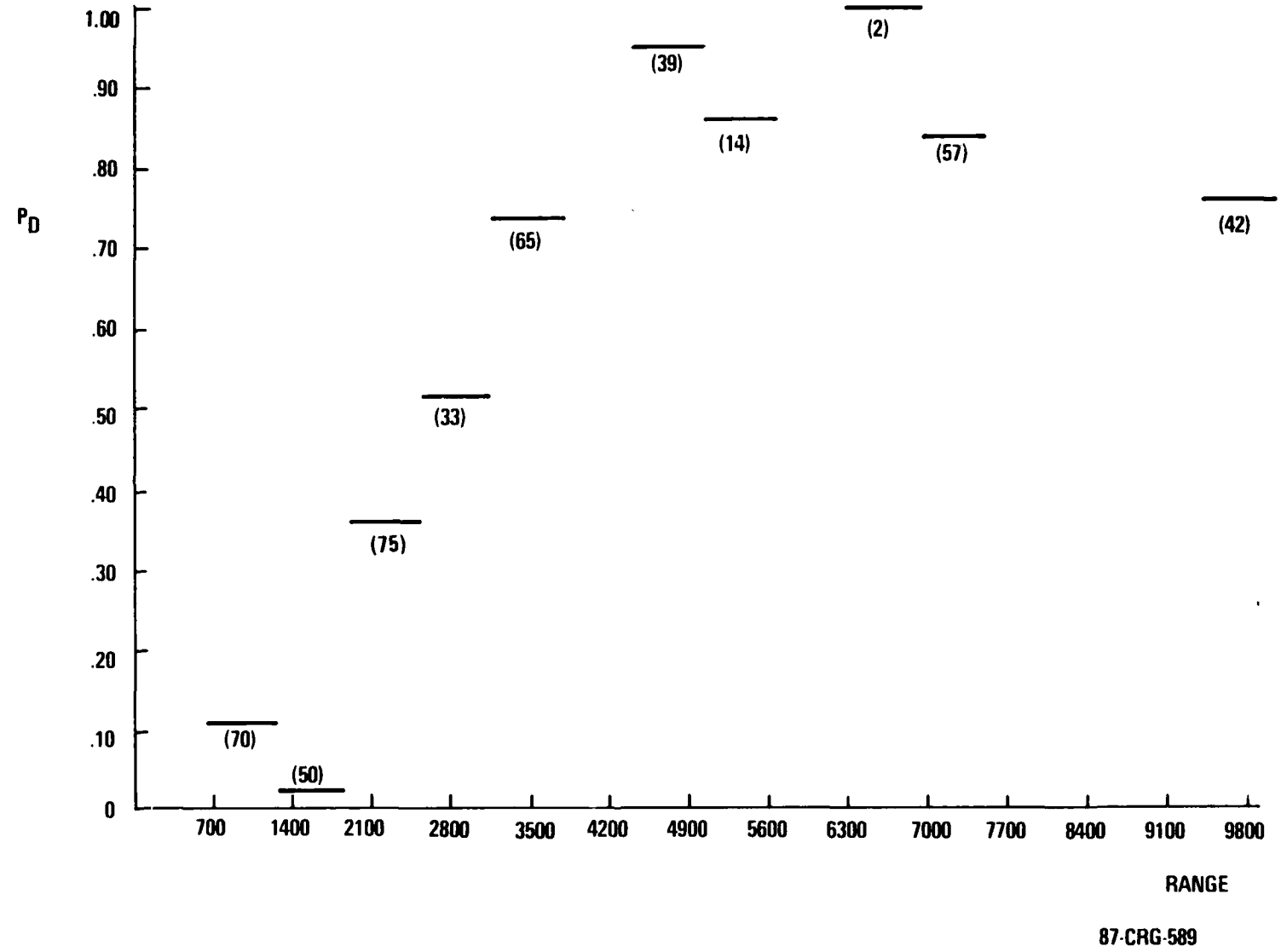

Figure 3-22. Post Clutter Rejection P_D vs. Range in Meters (complete data set)

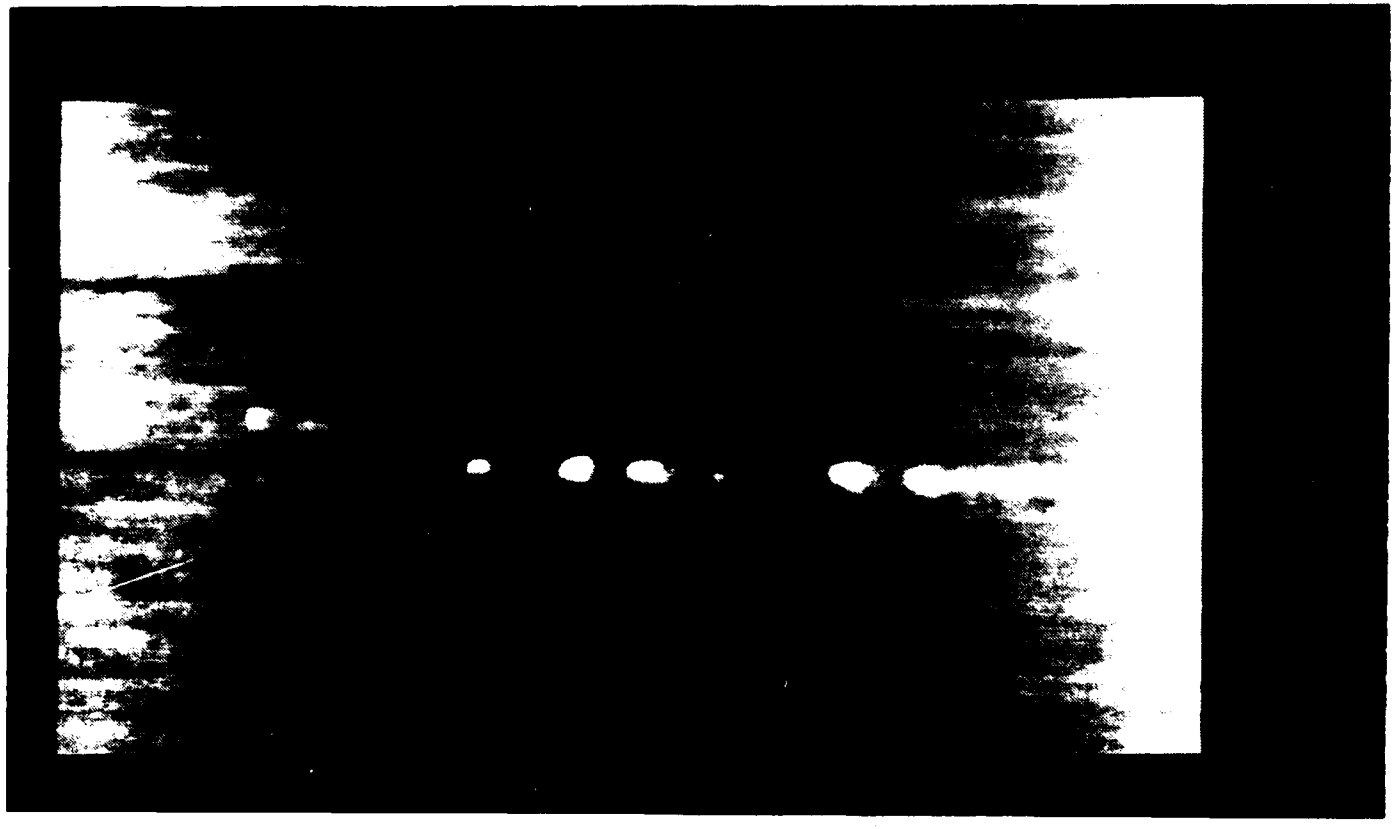

Figure 3-23. Representative Frame from Sequence 1 of MSN1712 Data Base

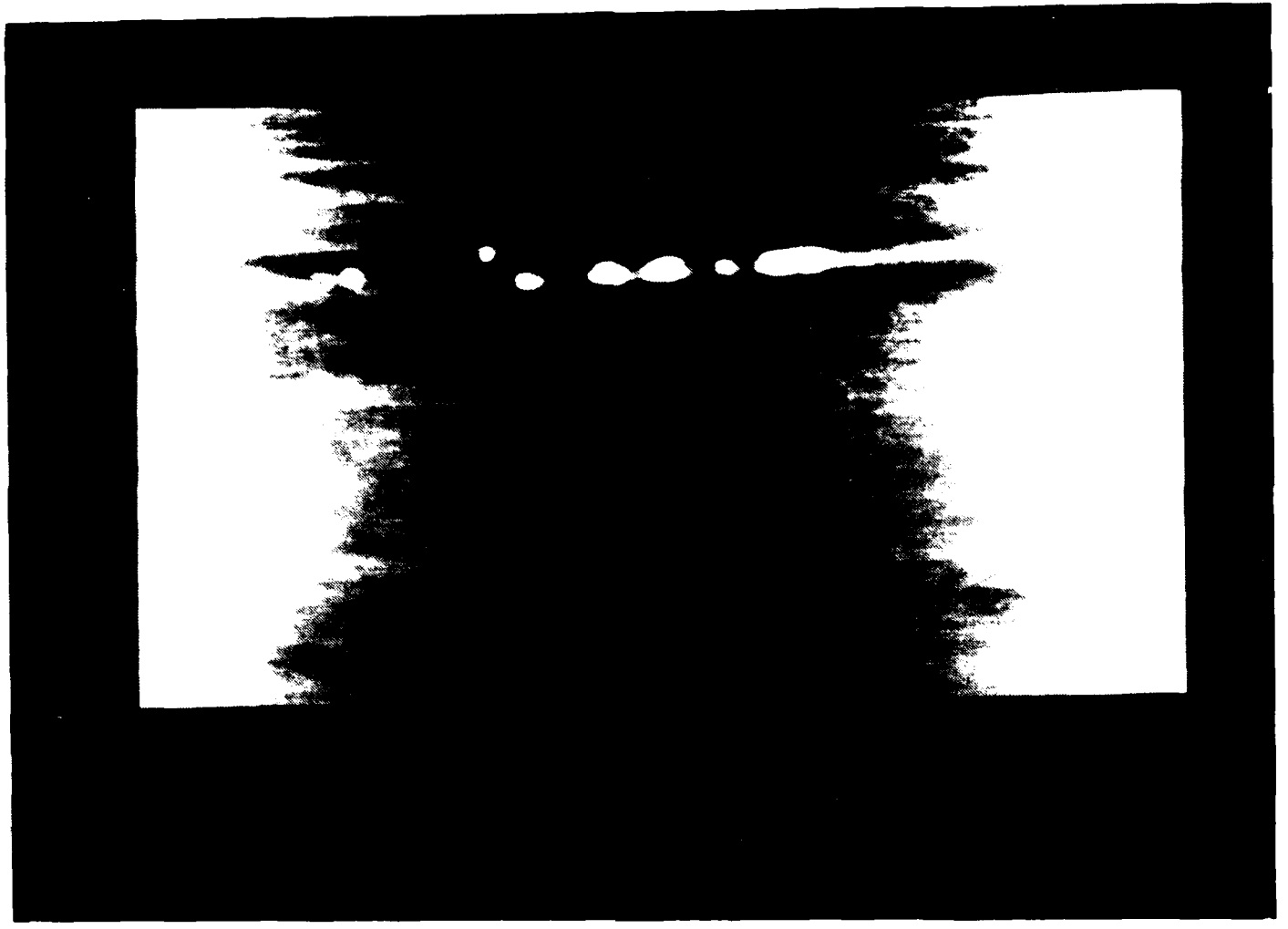

Figure 3-24. Representative Frame from Sequence 2 of MSN1712 Data Base

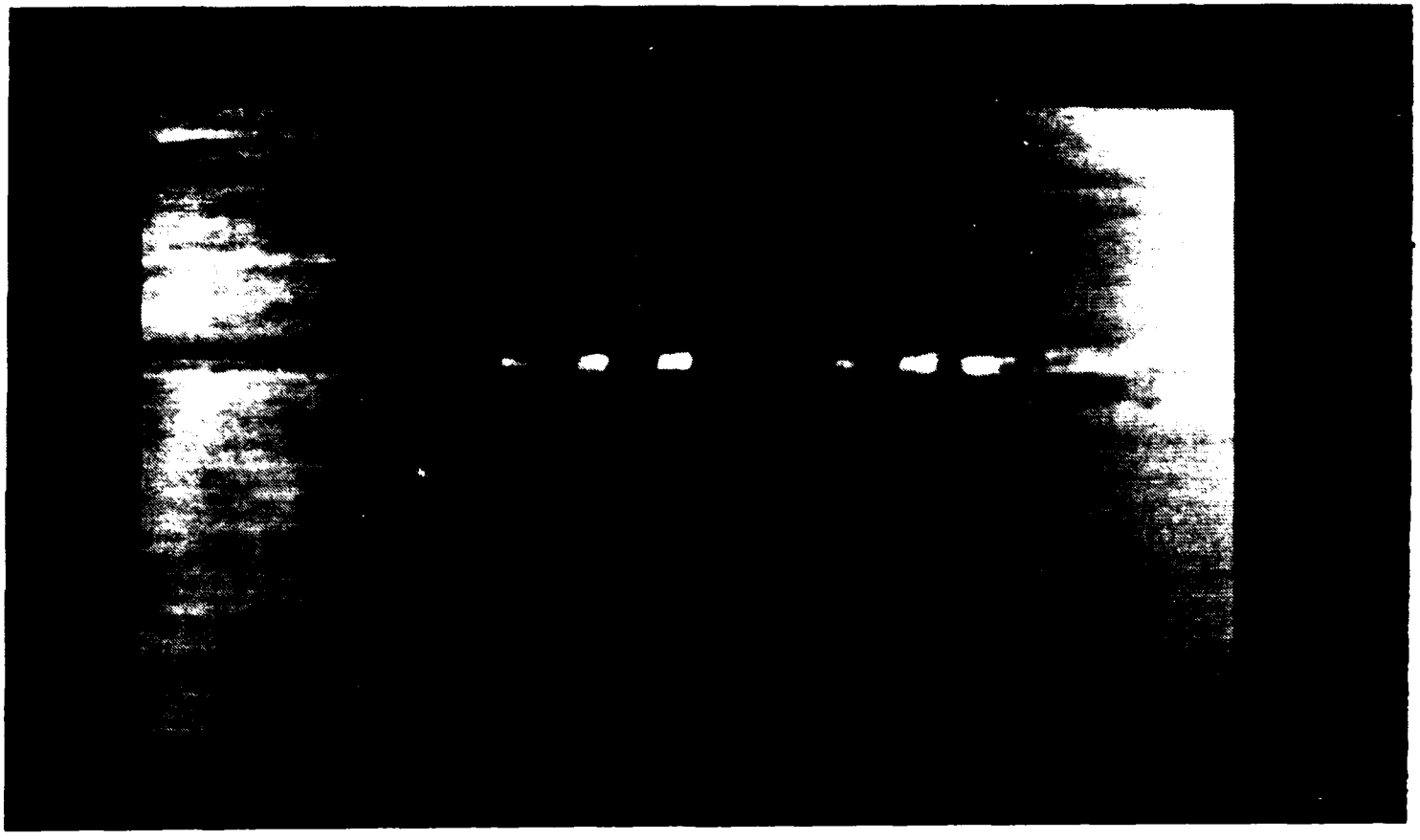

Figure 3-25. Representative Frame from Sequence 3 of MSN1712 Data Base

Figure 3-26. Representative Frame from Sequence 4 of MSN1712 Data Base

Figure 3-27. Representative Frame from Sequence 5 of MSN1712 Data Base

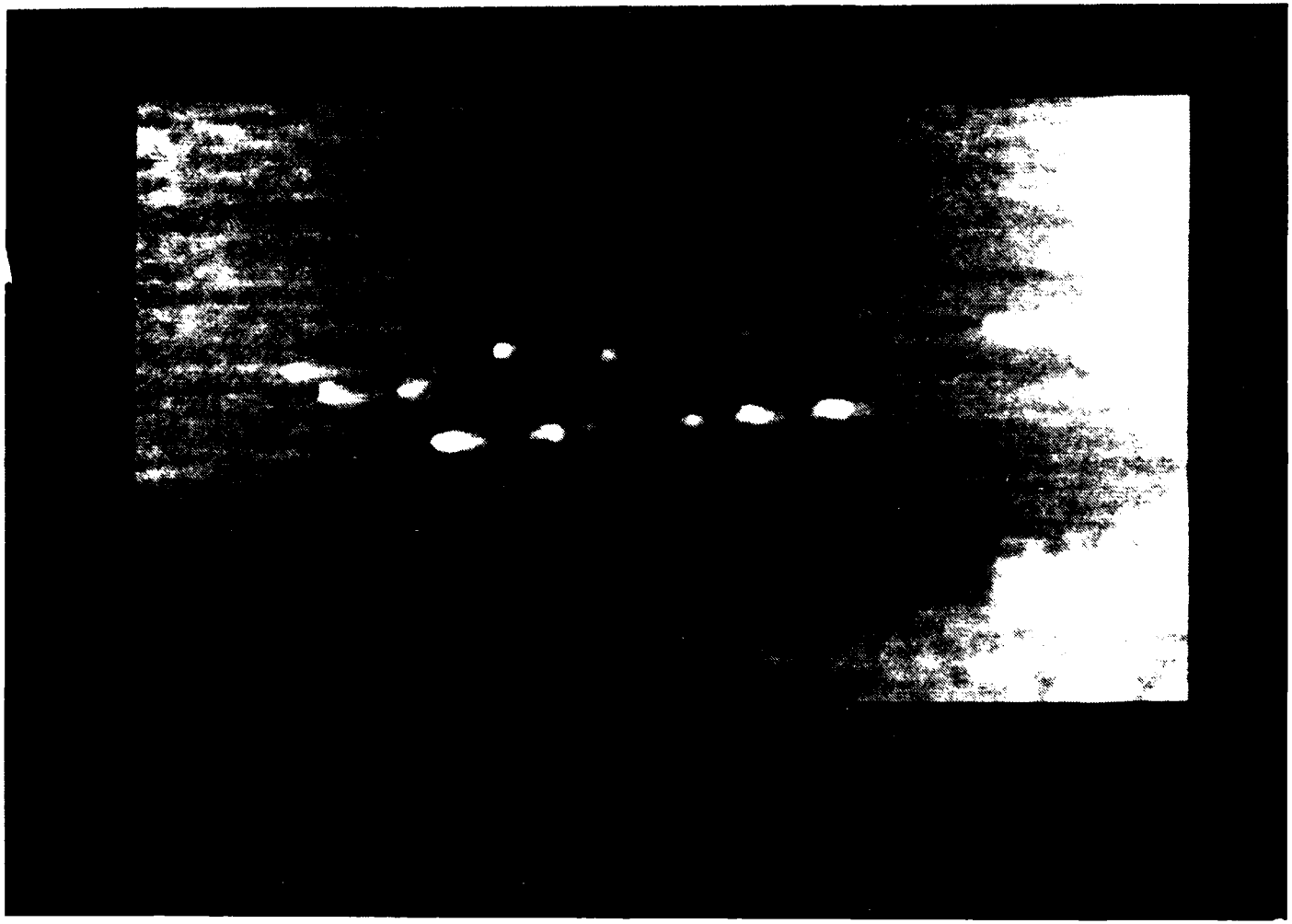

Figure 3-28. Representative Frame from Sequence 6 of MSN1712 Data Base

Figures 3-29 and 3-30 show that sequences 1 and 2 basically span the same metric space as defined by TIR^2 and ESR. In addition, sequence 2 contains 36 targets that do not overlap in metric space with those in the sequence 1. The detection rate for sequences 1 and 2 are 100% and 83%, respectively. These results are considerable improvements over single-frame processing because of the tracking module included in the multi-frame algorithm. The tracker was able to coast a target, based on previous frame data, even though in the current frame, the target in questions has a low contrast. The detection for sequence 2 was not as good as sequence 1 because several targets were too small.

Figures 3-31, 3-32, and 3-33 show segmentation accuracy (SA) versus the three metrics TIR^2, $TBIR^2$ and ESR, respectively, for sequence 1. No detected targets had less than 45% segmentation accuracy, while some were segmented at 86%.

Figures 3-34, 3-35, and 3-36 show segmentation accuracy versus TIR^2, $TBIR^2$, and ESR for sequence 2. The range of SA values are similar to those of the previous sequence. The range of TIR^2 for sequence 3 was from 0 to 18.9. For sequence 4, the range of TIR^2 was from 0 to numbers >100. For sequence 5, this range was from 0 to 29.6. And, finally, for sequence 6, the range of TIR^2 was from 0 to 68.4, with most of the values of TIR2 clustered around 0. This clustering around 0 was due to the fact that the value of background variance was large and the difference of mean intensities of target and background was small. Figures 3-37, 3-40, 3-43, and 3-46 show the ranges of TIR^2 and the corresponding SA values for sequences 3 through 6, respectively.

The range of the $TBIR^2$, as can be seen from Figures 3-38, 3-41, 3-44, and 3-47, varied from 0 to 8.97 in sequence 3 and from 0 to numbers >100 for sequence 4. For sequence 5, $TBIR^2$ varied from 0 to a large number ≥ 100. However the target corresponding to large $TBIR^2$ values was not detected, and Figure 3-38 shows the results of $TBIR^2 \leq 15$. And finally, for sequence 6, $TBIR^2$ varied from 0 to numbers ≥ 100. In the above, all values of $TBIR^2$ and TIR^2 that were larger or equal to 100 were put equal to 100 to reduce the dynamic range for display purposes.

The range of ESR, as can be seen from Figures 3-39, 3-42, 3-45, and 3-48, varied from 0 to 2660 in the third sequence. ESR varied from 13.4 to 4220 for the fourth sequence. It varied from 0 to 451 in the fifth sequence. The variation of ESR was from 0 to 2000 in the sixth sequence.

Figures 3-37 to 3-38 show the variations of the segmentation accuracy measure vs. target interference ratio squared (TIR^2), target background interference ratio squared ($TBIR^2$) and edge strength ratio (ESR). Segmentation accuracy values of 0 correspond to the cases when the ground truth and segmented targets did not overlap.

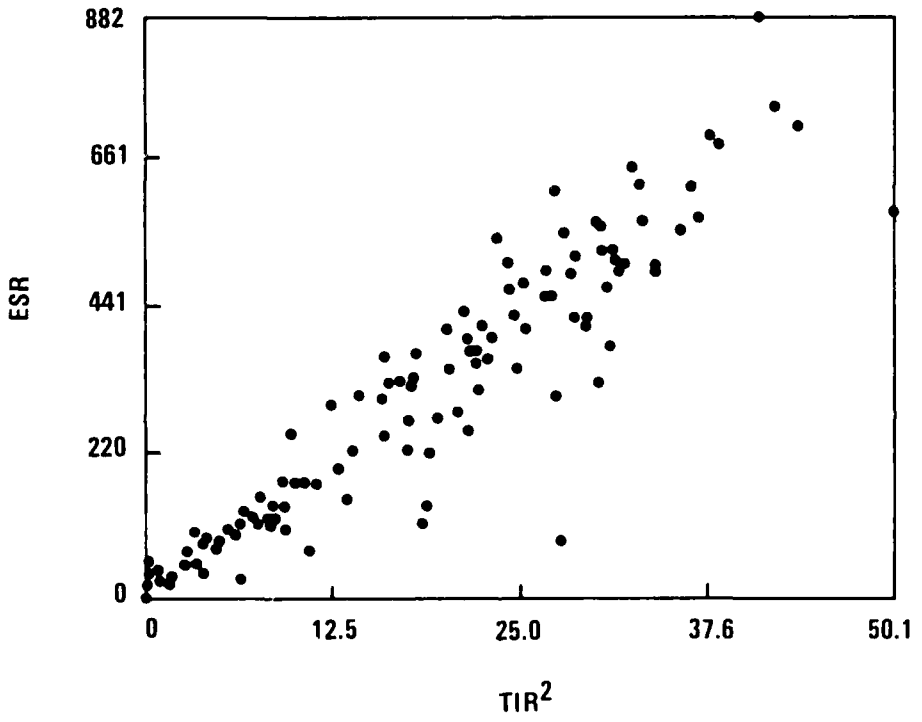

Figure 3-29. TIR^2 and ESR Values of Targets in Sequence 1

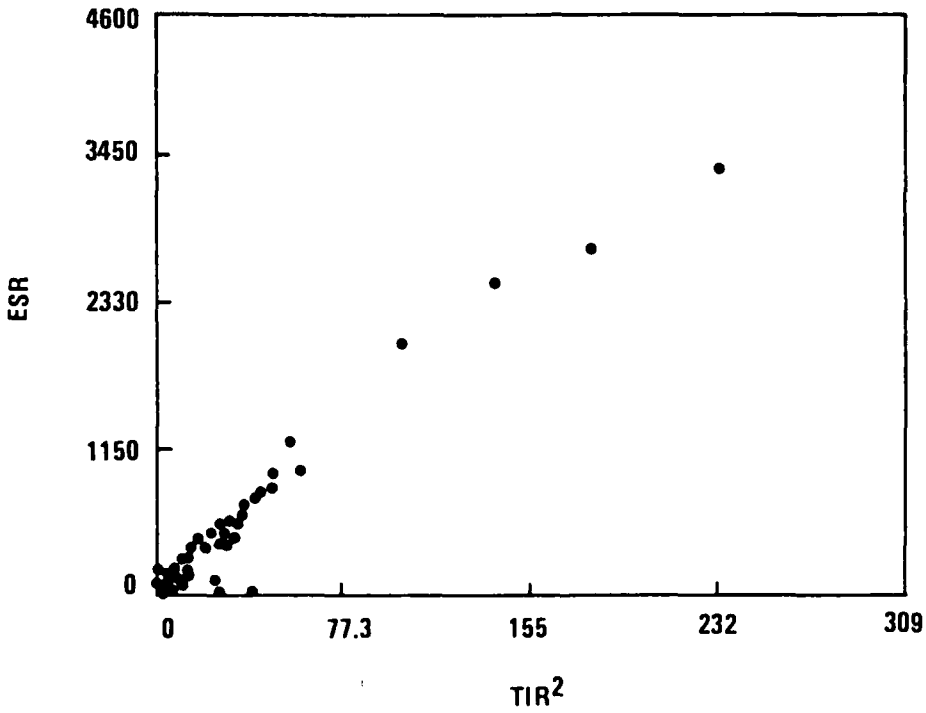

Figure 3-30. TIR^2 and ESR Values of Targets in Sequence 2

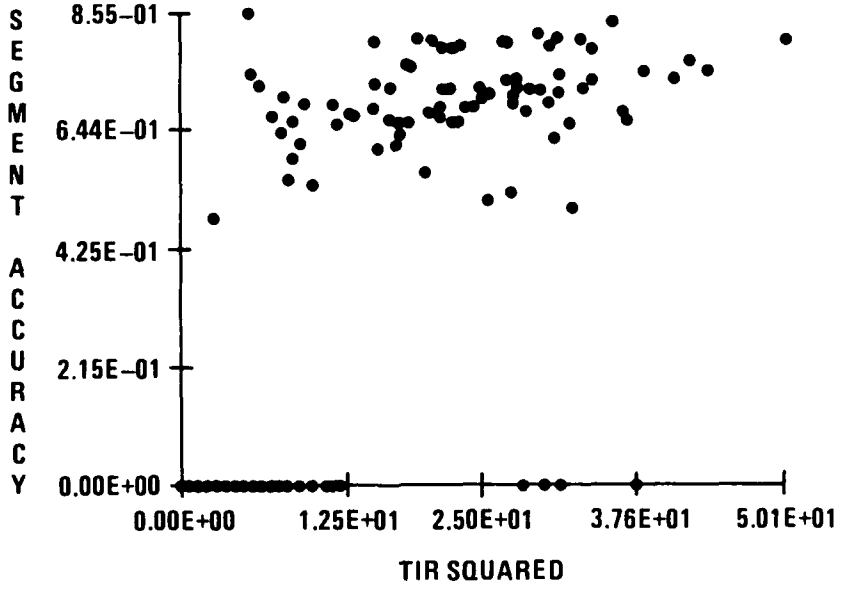

Figure 3-31. Segmentation Accuracy as a Function of TIR^2 (sequence 1)

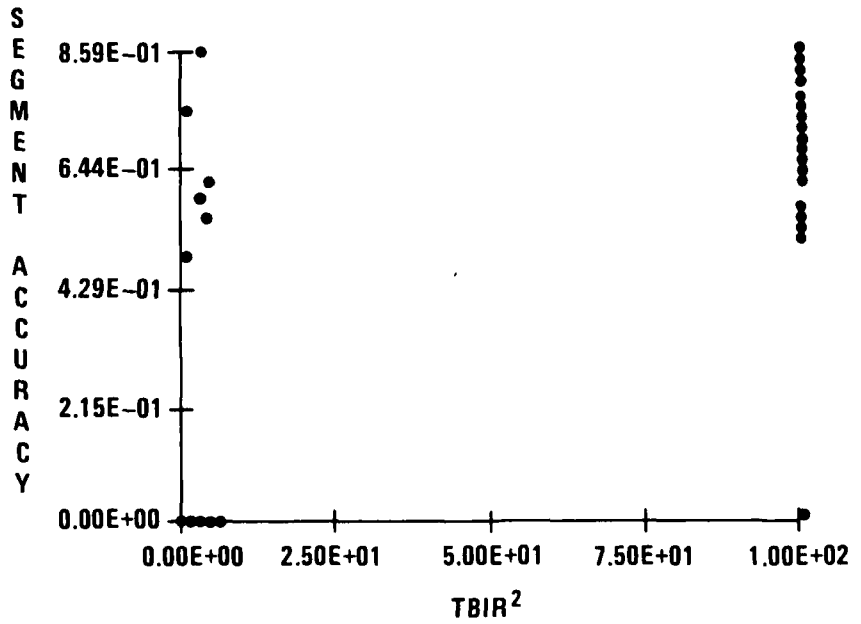

Figure 3-32. Segmentation Accuracy as a Function of $TBIR^2$ (sequence 1)

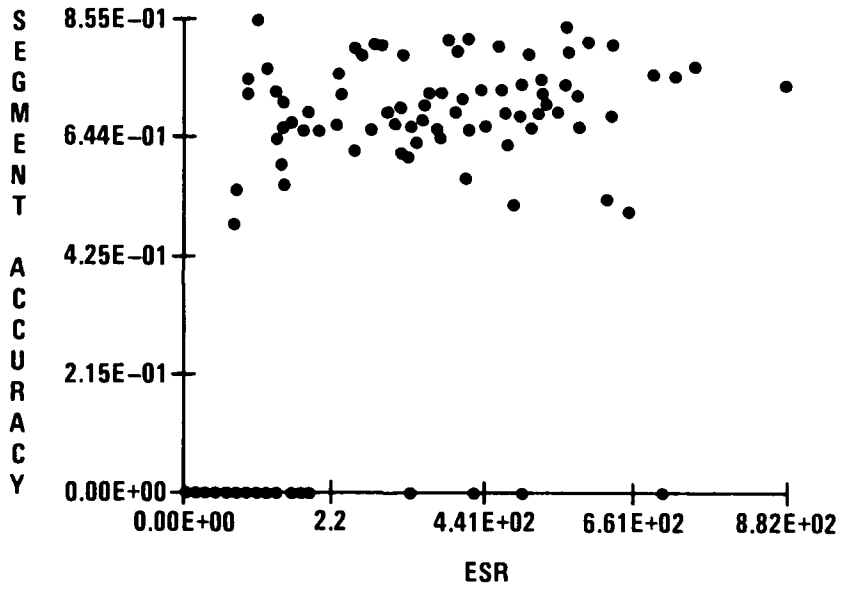

Figure 3-33. Segmentation Accuracy as a Function of ESR (sequence 1)

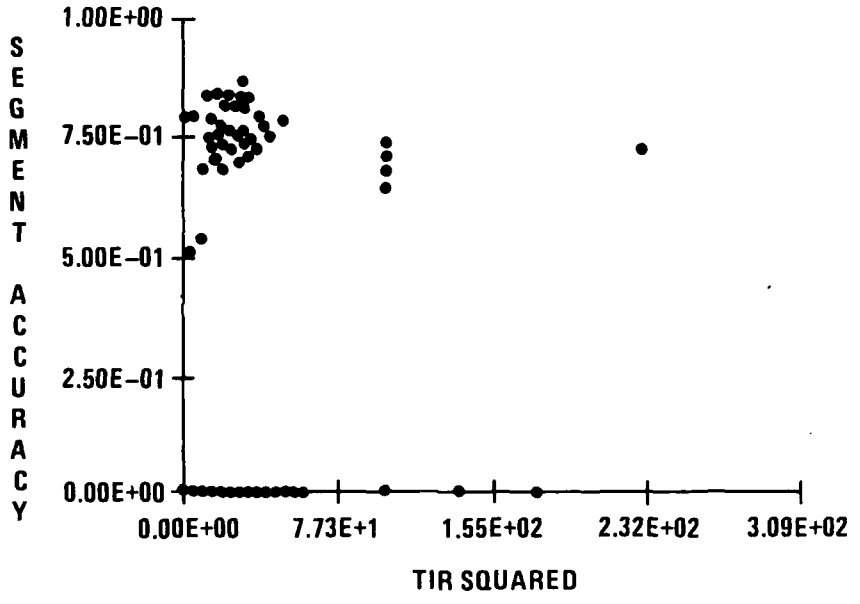

Figure 3-34. Segmentation Accuracy as a Function of TIR^2 (sequence 2)

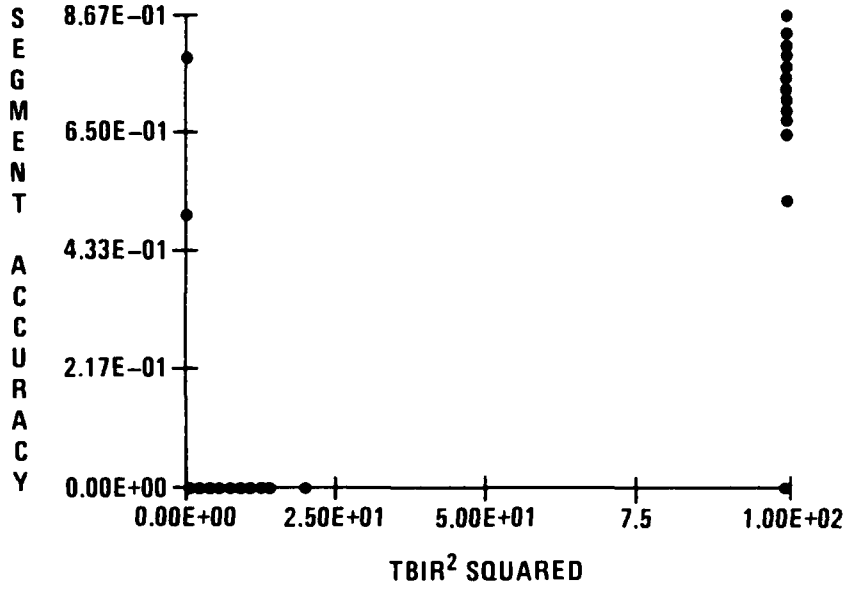

Figure 3-35. Segmentation Accuracy as a Function of $TBIR^2$ (sequence 2)

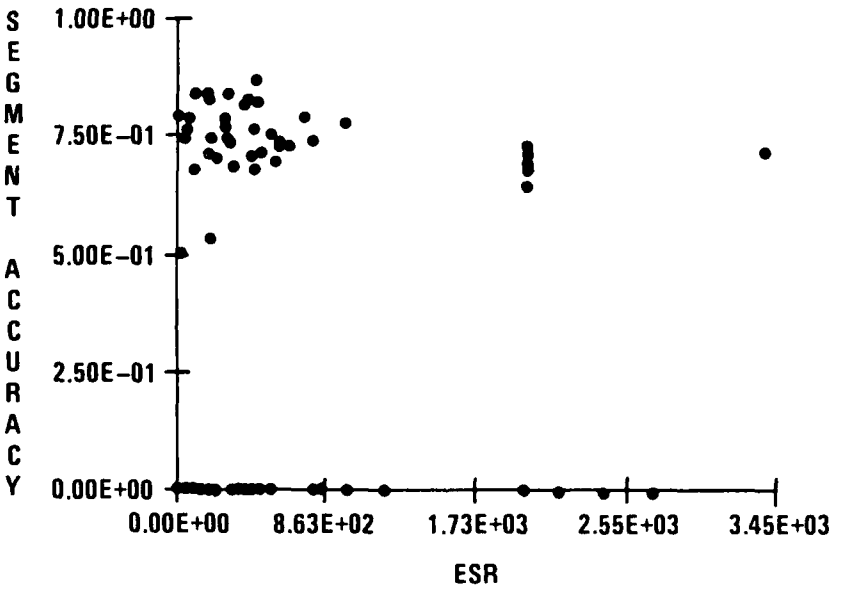

Figure 3-36. Segmentation Accuracy as a Function of ESR (sequence 2)

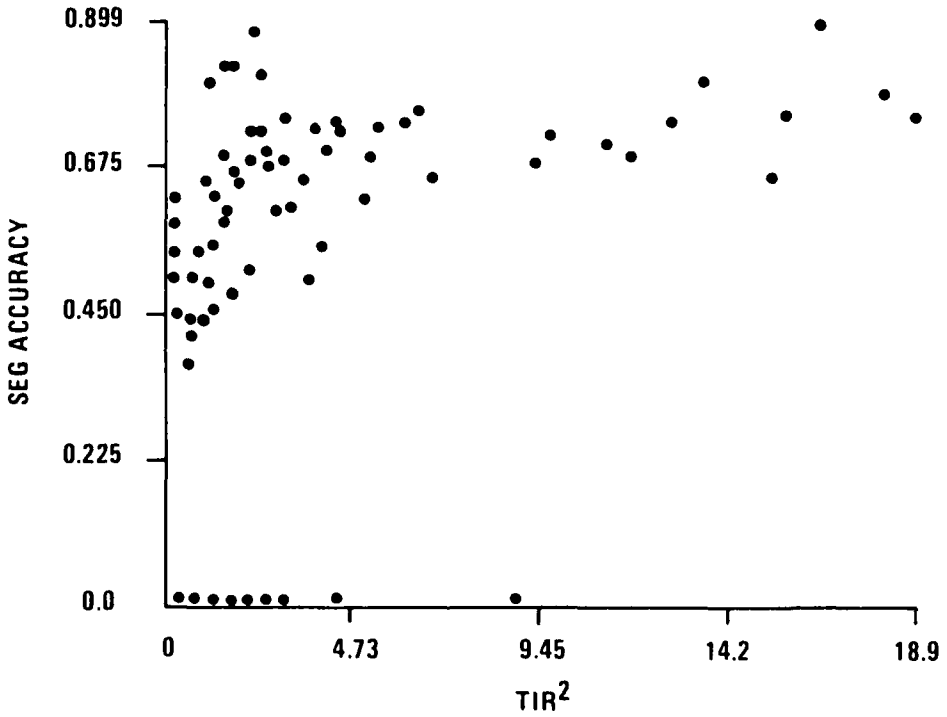

Figure 3-37. Variations of Segmentation Accuracy as TIR^2 Varies for Sequence 3 of the Honeywell MSN1712 Data Base

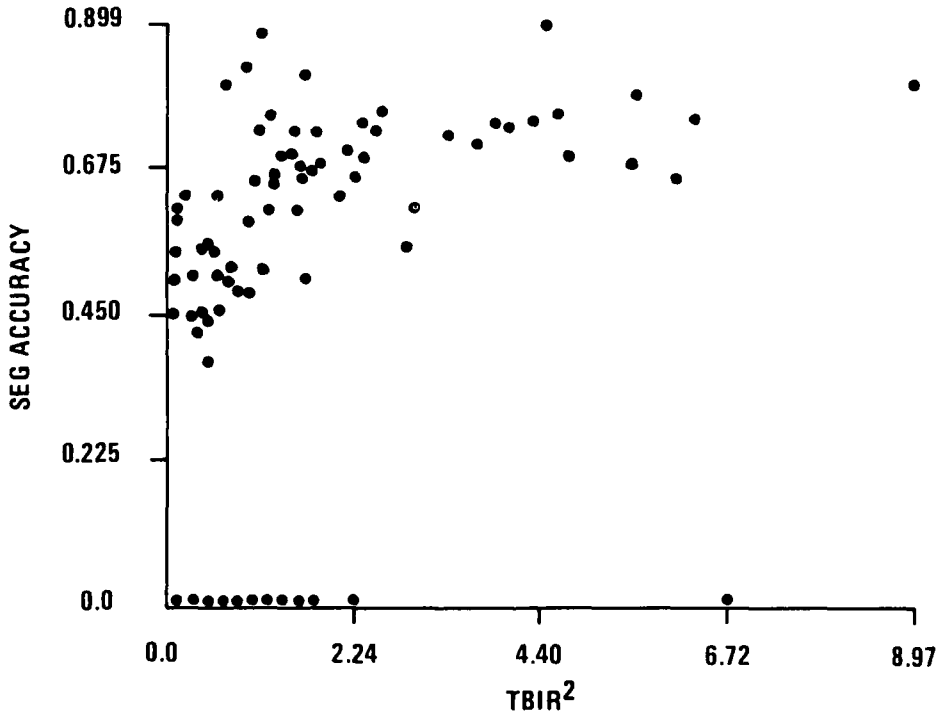

Figure 3-38. Variations of Segmentation Accuracy as $TBIR^2$ Varies for Sequence 3 of the Honeywell MSN1712 Data Base

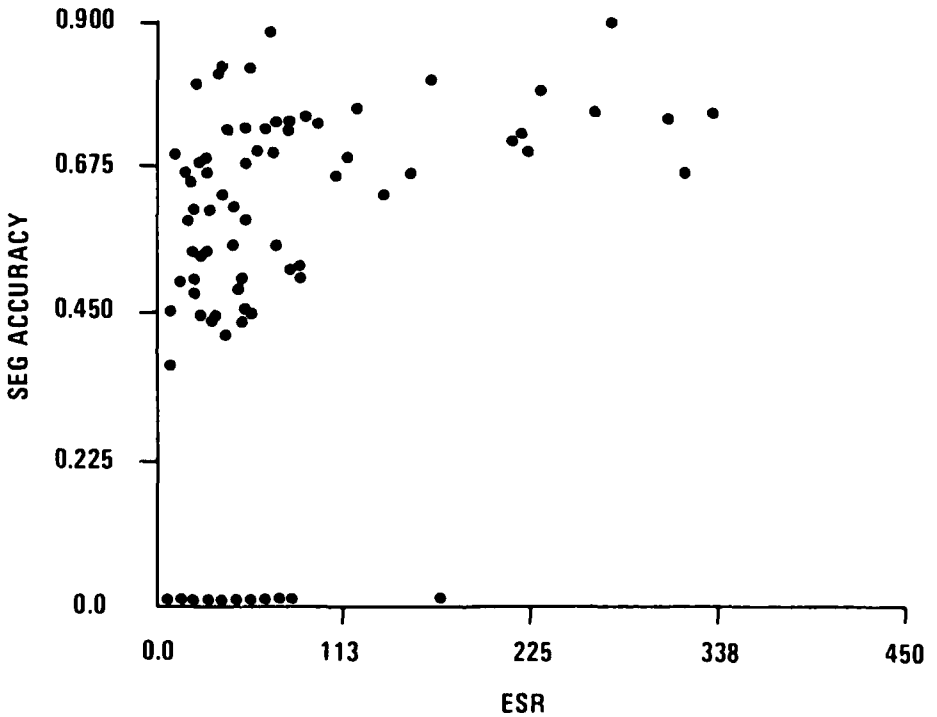

Figure 3-39. Variations of Segmentation Accuracy as ESR Varies for Sequence 3 of the Honeywell MSN1712 Data Base

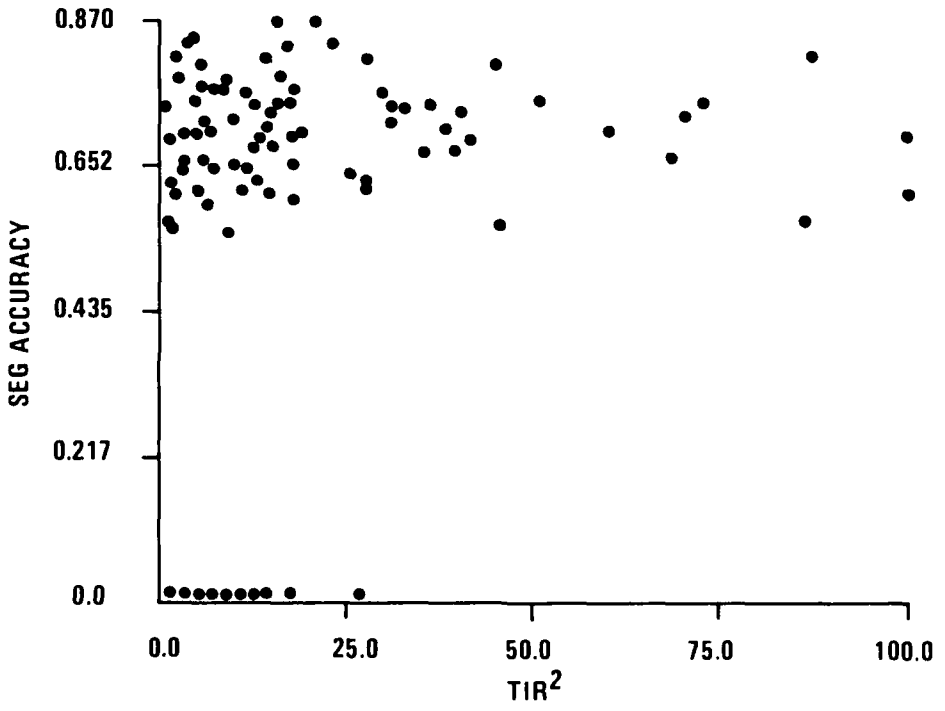

Figure 3-40. Variations of Segmentation Accuracy as TIR^2 Varies for Sequence 4 of the Honeywell MSN1712 Data Base

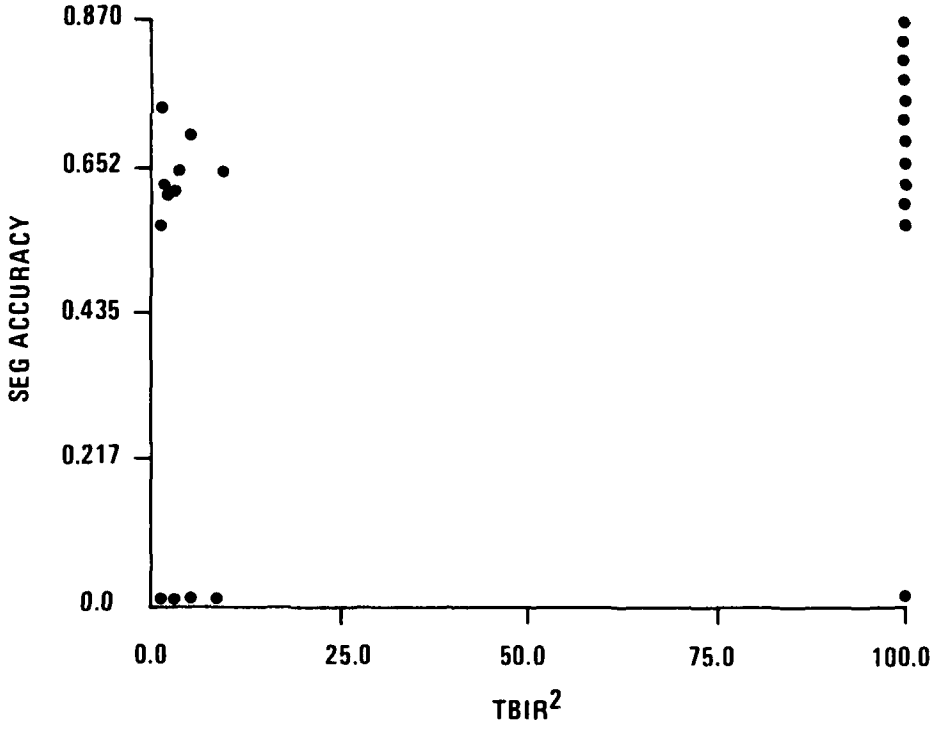

Figure 3-41. Variations of Segmentation Accuracy as $TBIR^2$ Varies for Sequence 4 of the Honeywell MSN1712 Data Base

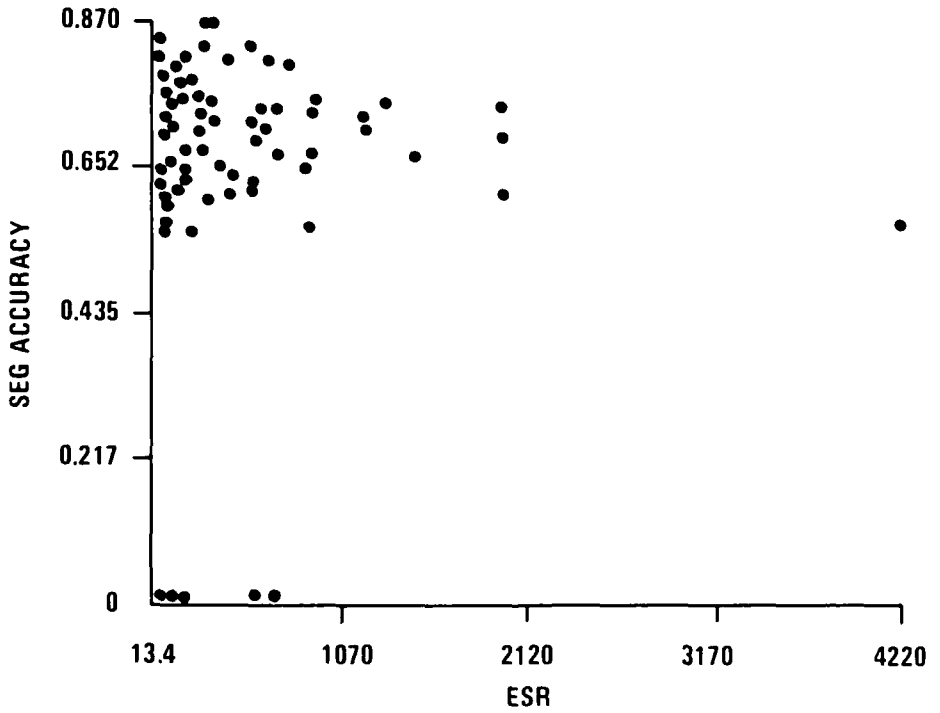

Figure 3-42. Variations of Segmentation Accuracy as ESR Varies for Sequence 4 of the Honeywell MSN1712 Data Base

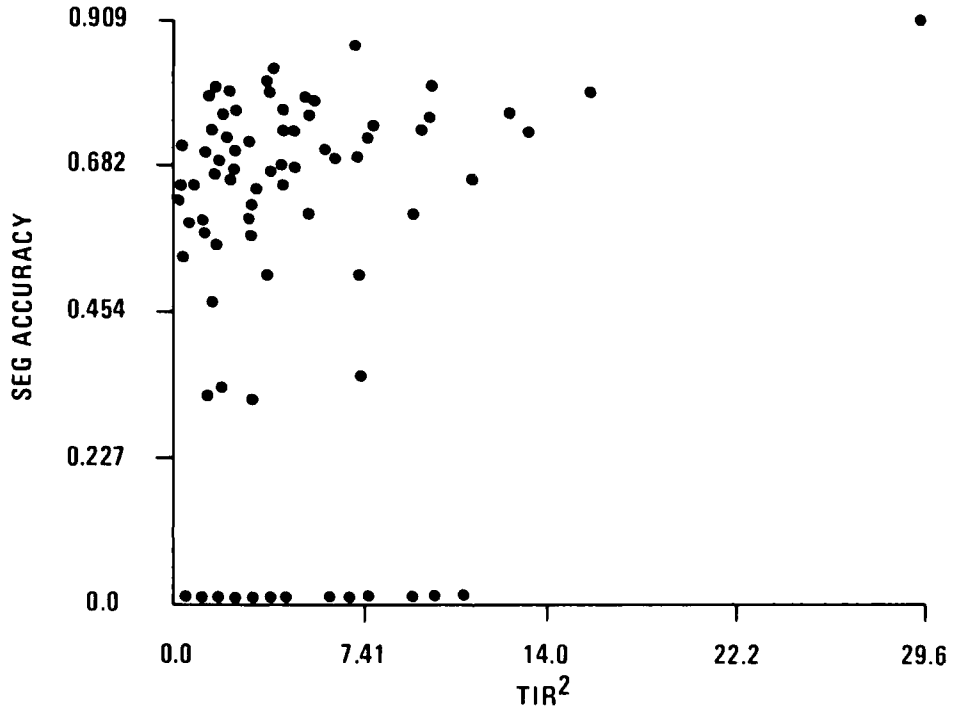

Figure 3-43. Variations of Segmentation Accuracy as TIR^2 Varies for Sequence 5 of the Honeywell MSN1712 Data Base

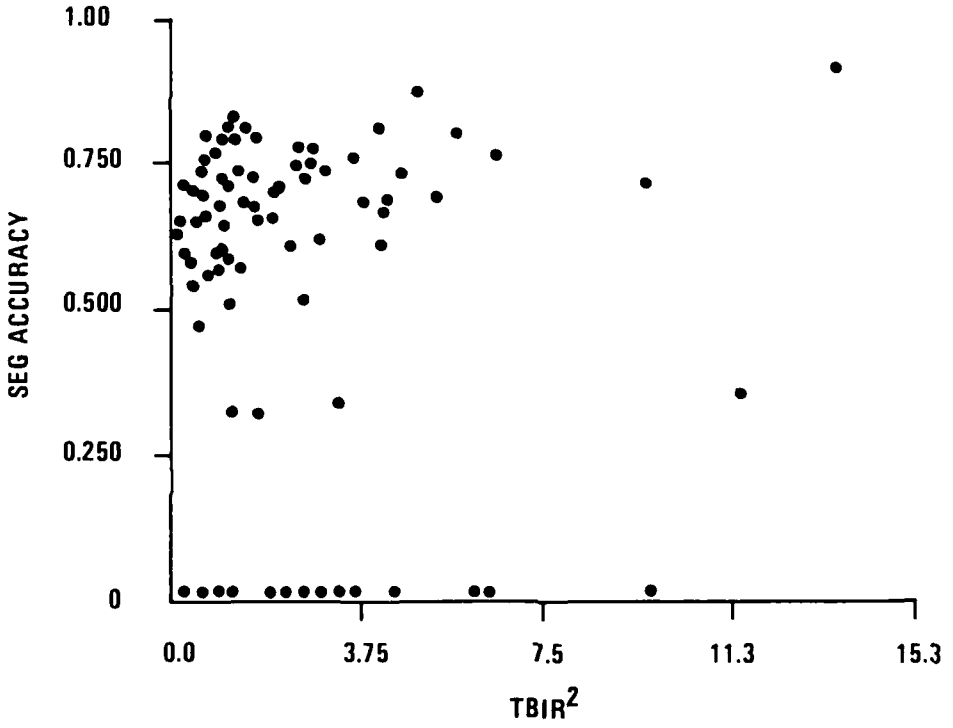

Figure 3-44. Variations of Segmentation Accuracy as $TBIR^2$ Varies for Sequence 5 of the Honeywell MSN1712 Data Base

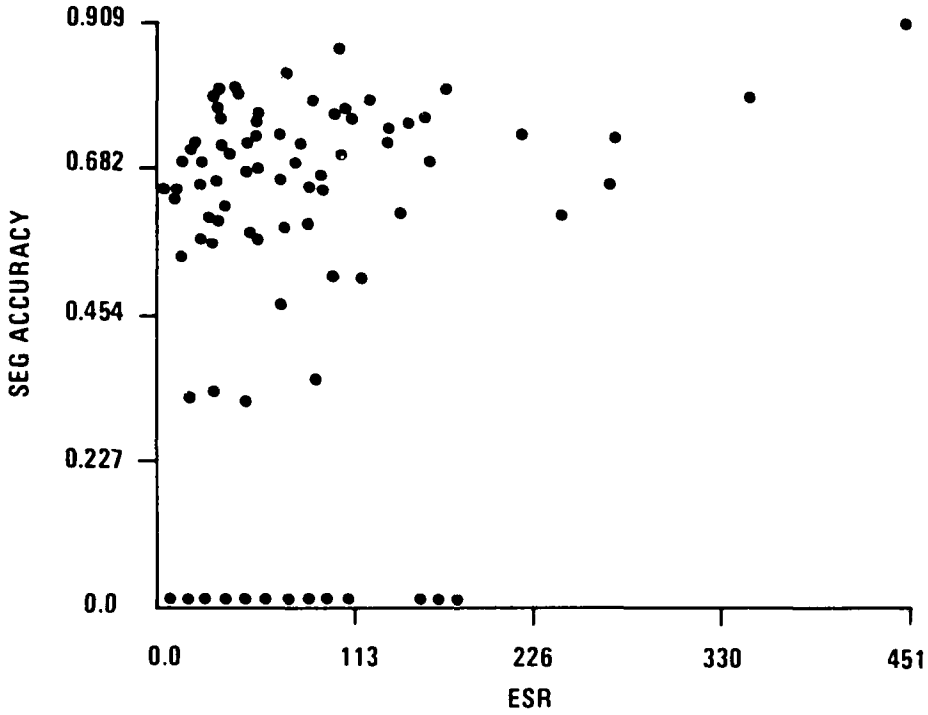

Figure 3-45. Variations of Segmentation Accuracy as ESR Varies for Sequence 5 of the Honeywell MSN1712 Data Base

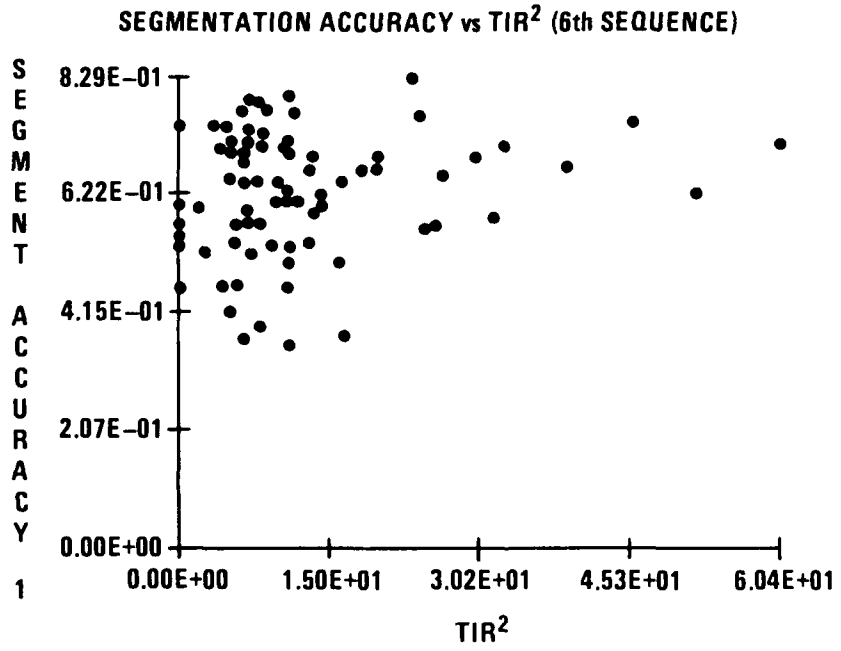

Figure 3-46. Variations of Segmentation Accuracy as TIR^2 Varies for Sequence 6 of the Honeywell MSN1712 Data Base

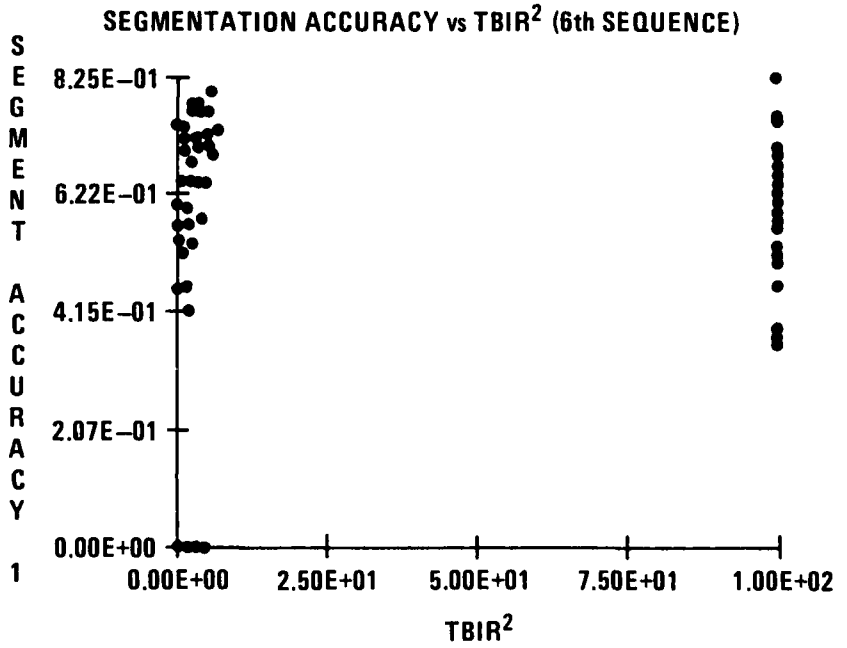

Figure 3-47. Variations of Segmentation Accuracy as $TBIR^2$ Varies for Sequence 6 of the Honeywell MSN1712 Data Base

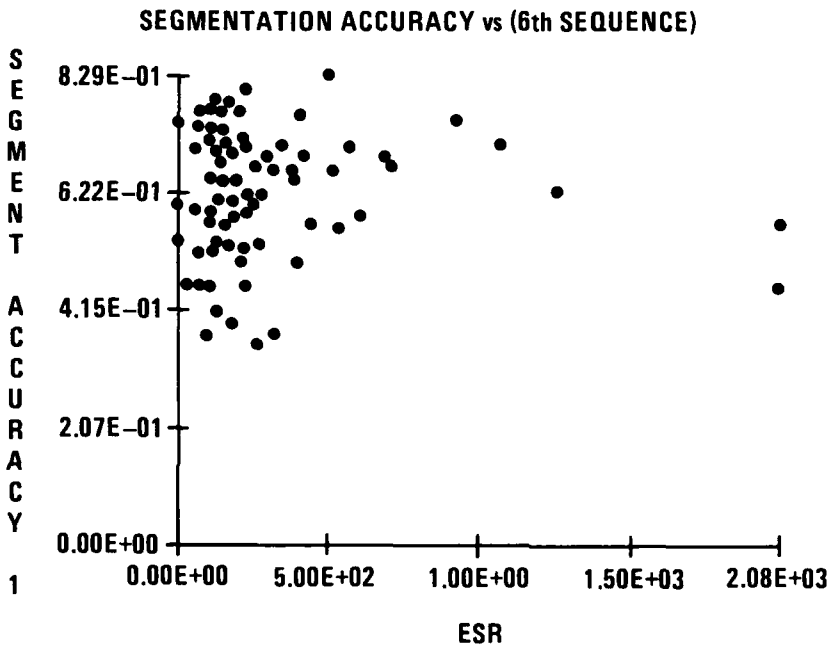

Figure 3-48. Variations of Segmentation Accuracy as ESR Varies for Sequence 6 of the Honeywell MSN1712 Data Base

3.3.1 SA vs. TIR^2

Segmentation accuracy (SA) generally increased as TIR^2 increased. For the third sequence, the mean value of SA varied from 0.60 in the first bin ($0<TIR^2<4.7$) to 0.78 for the last bin ($14.2<TIR^2<18.7$). For sequence 4 of the Honeywell sequential data base, SA mean values increased from 0.71 in the first bin ($0<TIR^2<25$) to 0.72 in the third bin ($50<TIR^2<75$), and then decreased to 0.67 for the last bin ($75<TIR^2<100$). In sequence 5, mean value of SA varied from 0.66 in the first bin ($0<TIR^2<7.41$) to 0.91 in the fourth bin ($22.2<TIR^2<29.6$). In sequence 6 the mean TIR^2 value increased from the value of 0.64 in the first bin ($0<TIR^2<15.1$) to 0.71 in the fourth bin ($45.3<TIR^2<60.4$).

3.3.2 SA vs. $TBIR^2$

The mean segmentation accuracy (SA) for sequence 3 of the Honeywell MSN1712 data base increased from 0.60 in the first bin ($0<TBIR^2<2.24$) to 0.81 in the fourth bin ($6.72<TBIR^2<8.97$). For sequence 5, the mean SA value increased from 0.67 in the first bin ($0<TBIR^2<3.7$) to 0.91 in the fourth bin ($11.3<TBIR^2<15$). For sequence 6 the mean SA value decreased from 0.63 in the first bin ($0<TBIR^2<25$) to 0.59 for the fourth bin ($75<TBIR^2<100$).

In general, the mean SA value increased as $TBIR^2$ increased. However, for sequence 6, this was not the case and the mean SA value decreased as $TBIR^2$ increased.

3.3.3 SA vs. ESR

The mean segmentation accuracy (SA) for sequence 3 of the Honeywell MSN1712 data base was 0.63 for ($0<ESR<662$). For sequence 4 the mean SA decreased from 0.71 in the first bin ($0<ESR<1070$) to 0.57 in the fourth bin ($3170<ESR<4220$). In sequence 5, the mean SA increased from 0.66 in the first bin ($0<ESR<113$) to 0.72 in the second bin ($113<ESR<226$), then dipped down to 0.67 in the third bin ($226<ESR<338$). Finally, the mean SA value went up to 0.85 in the fourth bin ($338<ESR<451$). In sequence 6, the mean SA decreased from 0.63 in the first bin ($0<ESR<25$) to 0.59 in the fourth bin ($75<ESR<100$).

3.3.4 P_D vs. FAR

Figure 3-49 shows the variation of P_D vs. FAR. The numbers inside the parentheses reflect the number of samples that contributed to the derivations of the (P_D, FAR) points. As can be seen, a large number of samples are clustered around FAR < 1 a $P_D > 0.65$.

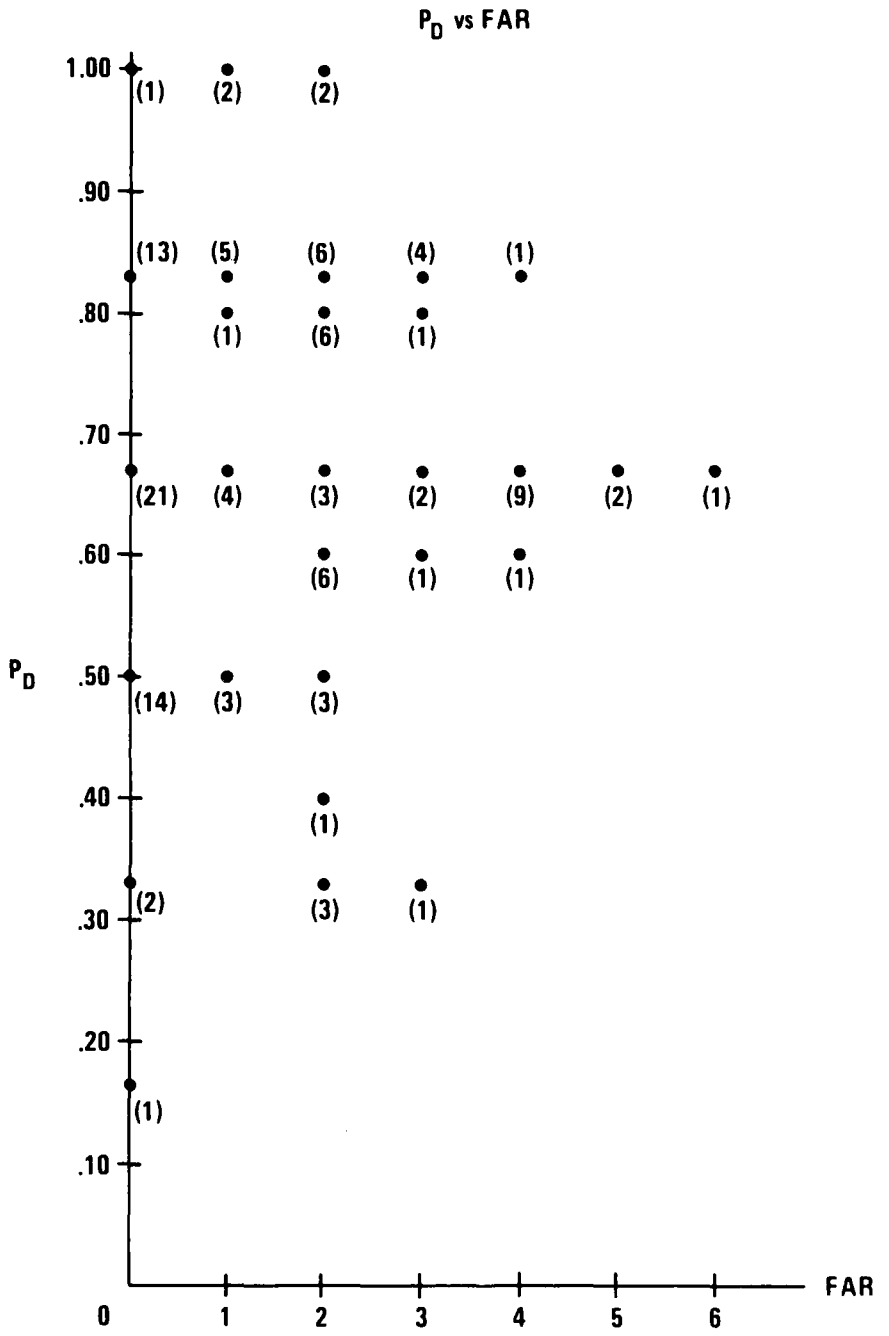

Figure 3-49. Variation of P_D as Function of FAR

3.4 BACORE MODELING

Modeling the performance of BACORE as a function of a set of image metrics is useful in many ways. First, the models can be used to predict the behavior of the algorithms in areas where no data are available, and second, the models can be used to modify and adapt the algorithm parameters to influence the algorithm behaviors in desired ways. We used seven different models to model the performance of the multi-frame BACORE as a function of a set of image metrics. The performance measures that were used were the following:

- Segmentation accuracy vs. TIR^2
- Segmentation accuracy vs. $TBIR^2$
- Segmentation accuracy vs. ESR
- Segmentation accuracy vs. range
- Probability of post segment target detection vs. TIR^2
- Probability of post segment target detection vs. ESR
- Probability of post segment target detection vs. range

In this experiment, "post segment" refers to the output of the clutter rejection module. For the experiment, we used the Honeywell MSN1712 sequential data base. The first three sequences were used for modeling and the last three sequences were to be used for validating the models. In the modeling part, metric space was quantized uniformally into four consecutive bins. An attempt was made to select the same number of samples in each bin. This process was done for each of the sequences. Then polynomials of up to nine degrees were fit into these selected data. The polynomial degrees were chosen in such a way as to produce minimum residual errors.

Figures 3-50 to 3-52 show the models for each of the performance measures as polynomial functions of a set of metrics.

For Segmentation accuracy vs. TIR^2, the derived model is expressed as the following:

$$SA = 0.71 - 2.81\times10^{-3}(TIR^2)+3.67\times10^{-4}(TIR^2)^2 - 9.05\times10^{-6}(TIR^2)^3 +7.47\times10^{-8}(TIR^2)^4+ 1.81\times10^{-10}(TIR^2)^5 \quad (6)$$

The standard deviation of the error was 8.131×10^{-2}. Due to the lack of sufficient data for large TIR^2 values, the model should be considered only for ranges of $TIR^2<150$.

For segmentation accuracy vs. $TBIR^2$, the derived model is expressed as the following:

$$SA = 0.56+3.18\times10^{-2}(TBIR^2) - 3.02 \times 10^{-4} (TBIR^2)^2 \quad (7)$$

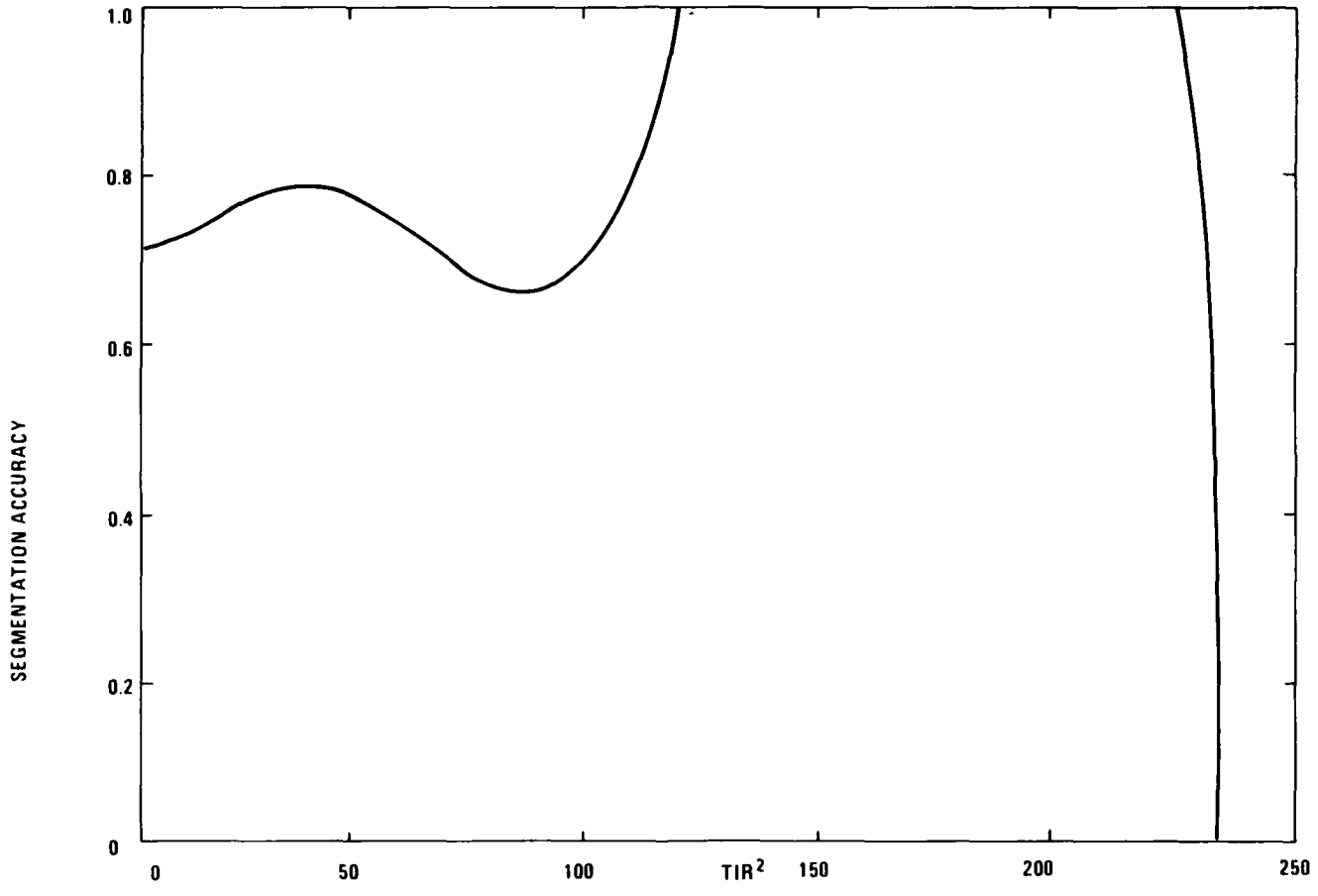

Figure 3-50. Model of SA vs. TIR^2

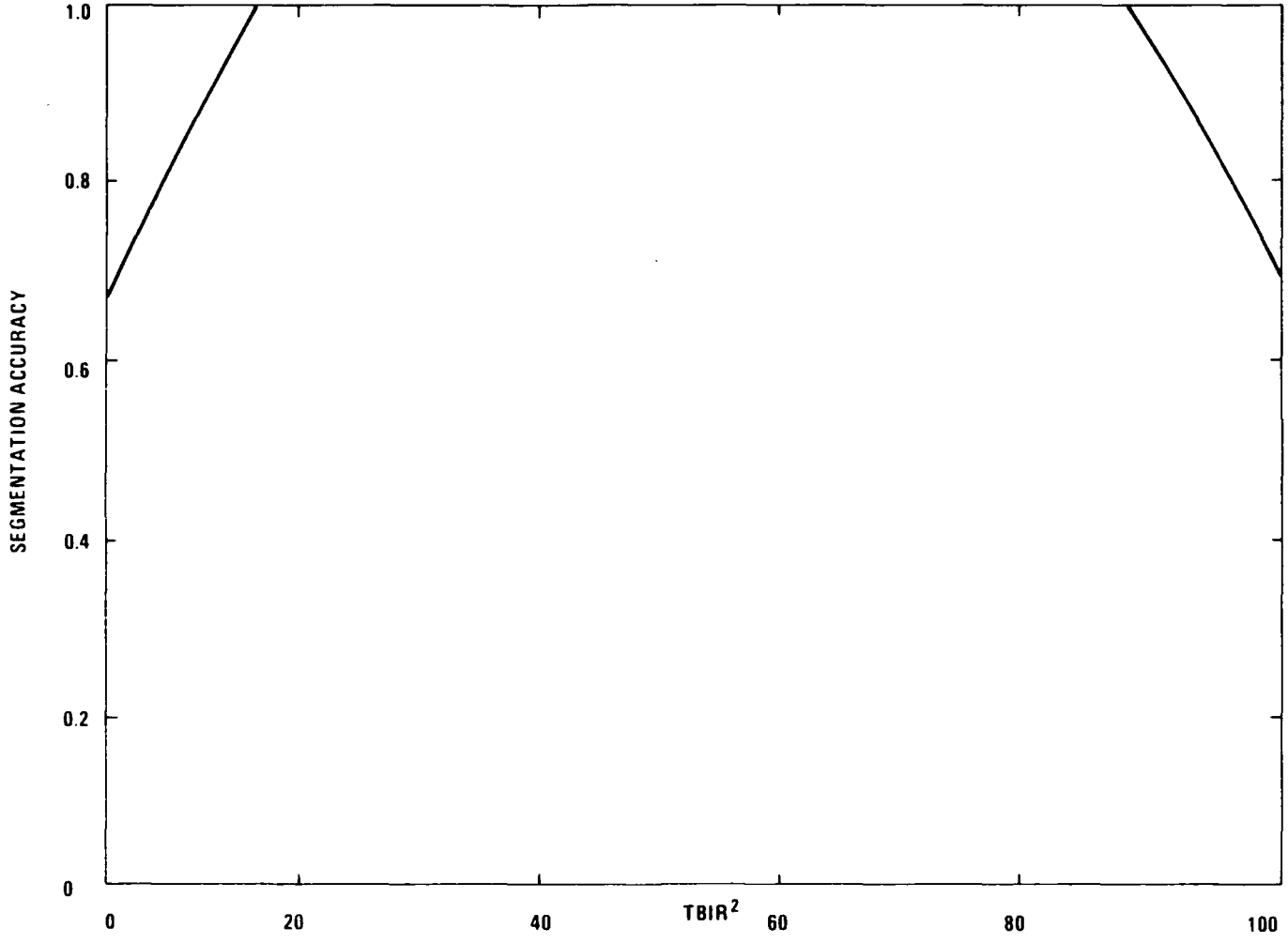

Figure 3-51. Model of SA vs. $TBIR^2$

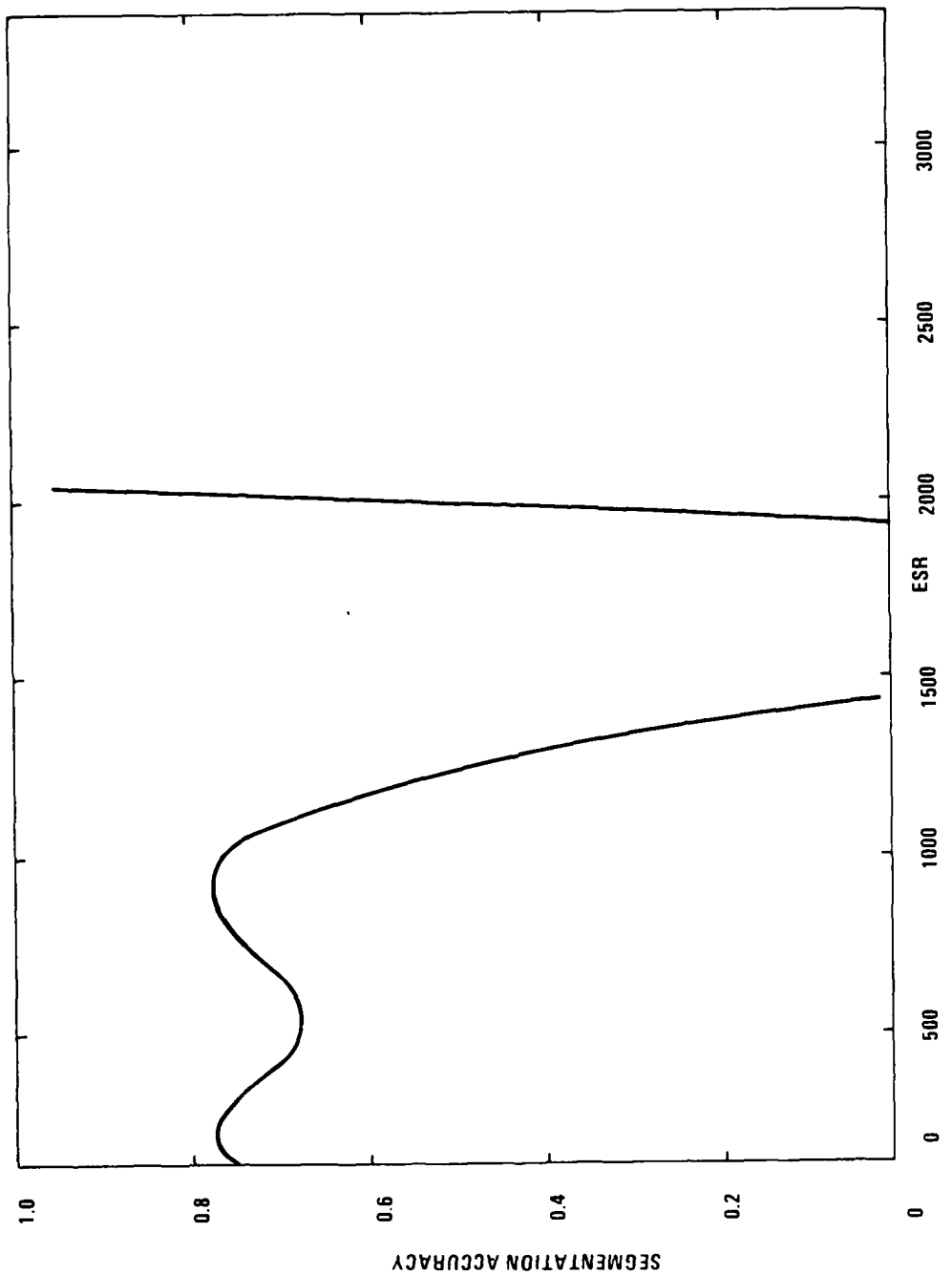

Figure 3-52. Model of SA vs. ESR

The standard deviation of the error was 9.48×10^{-2}. Due to the lack of sufficient data for large $TBIR^2$ values, the model should be considered only for ranges of $TBIR^2 < 150$.

For the segmentation accuracy vs. ESR, the derived model is expressed as the following:

$$SA = 0.40 + 4.72 \times 10^{-3}(ESR) - 2.10 \times 10^{-5}(ESR)^2 + 3.91 \times 10^{-8}(ESR)^3 - 3.33 \times 10^{-11}(ESR)^4 + 1.25 \times 10^{-14}(ESR)^5 - 1.65 \times 10^{-18}(ESR)^6 \quad (8)$$

The standard deviation of the error was 7.62×10^{-2}.

This model shows peculiar behavior around ESR values from 1000 to 2000, where the model falls off and again increases sharply. Due to the lack of sufficient data in regions of ESR>1000, we have to treat the behavior of the algorithm model for ESR>1000 with low confidence. However, more studies need to be performed to explain this phenomenon if indeed future experimentations are to confirm the presence of this unexpected behavior.

For segmentation accuracy vs. range, the derived model is expressed as the following:

$$SA = -3.91 + 1.63 \times 10^{-3}(Range) - 1.42 \times 10^{-7}(Range)^2 \quad (9)$$

The standard deviation of the error was 0.1006. This curve is displayed in Figure 3-53. As expected, the SA increases with range, reaches its optimum at ranges of 5000 to 6000 and then decreases.

For probability of detection vs. TIR^2, the derived model is expressed in the following:

$$P_D = 0.53 + 0.03(ITR^2) - 9.63 \times 10^{-4}(TIR^2)^2 + 7.36 \times 10^{-6}(TIR^2)^3 - 1.71 \times 10^{-8}(TIR^2)^4 \quad (10)$$

The standard deviation of the error was 0.2003215. This curve is displayed in Figure 3-54. The model should be considered at the ranges of $TIR^2 > 150$. SA increases with the increase in TIR^2 and then decreases to less than 0.5 and again increases. The cause of this behavior needs to be explored in the future.

For probability of detection vs. ESR, the derived model is the following:

$$P_D = 0.58 + 1.44 \times 10^{-3}(ESR) - 1.29 \times 10^{-6}(ESR)^2 + 2.67 \times 10^{-10}(ESR)^{+3} \quad (11)$$

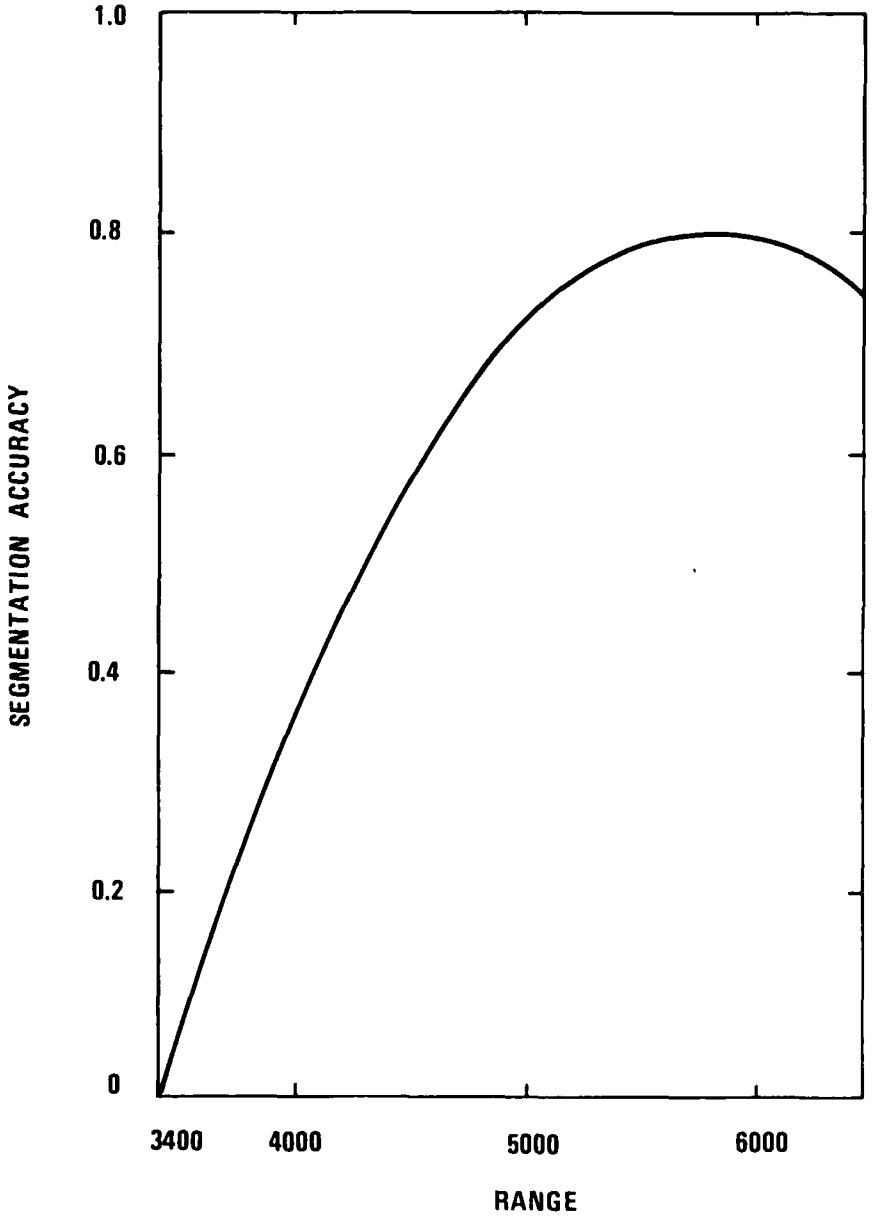

Figure 3-53. Model of SA vs. Range

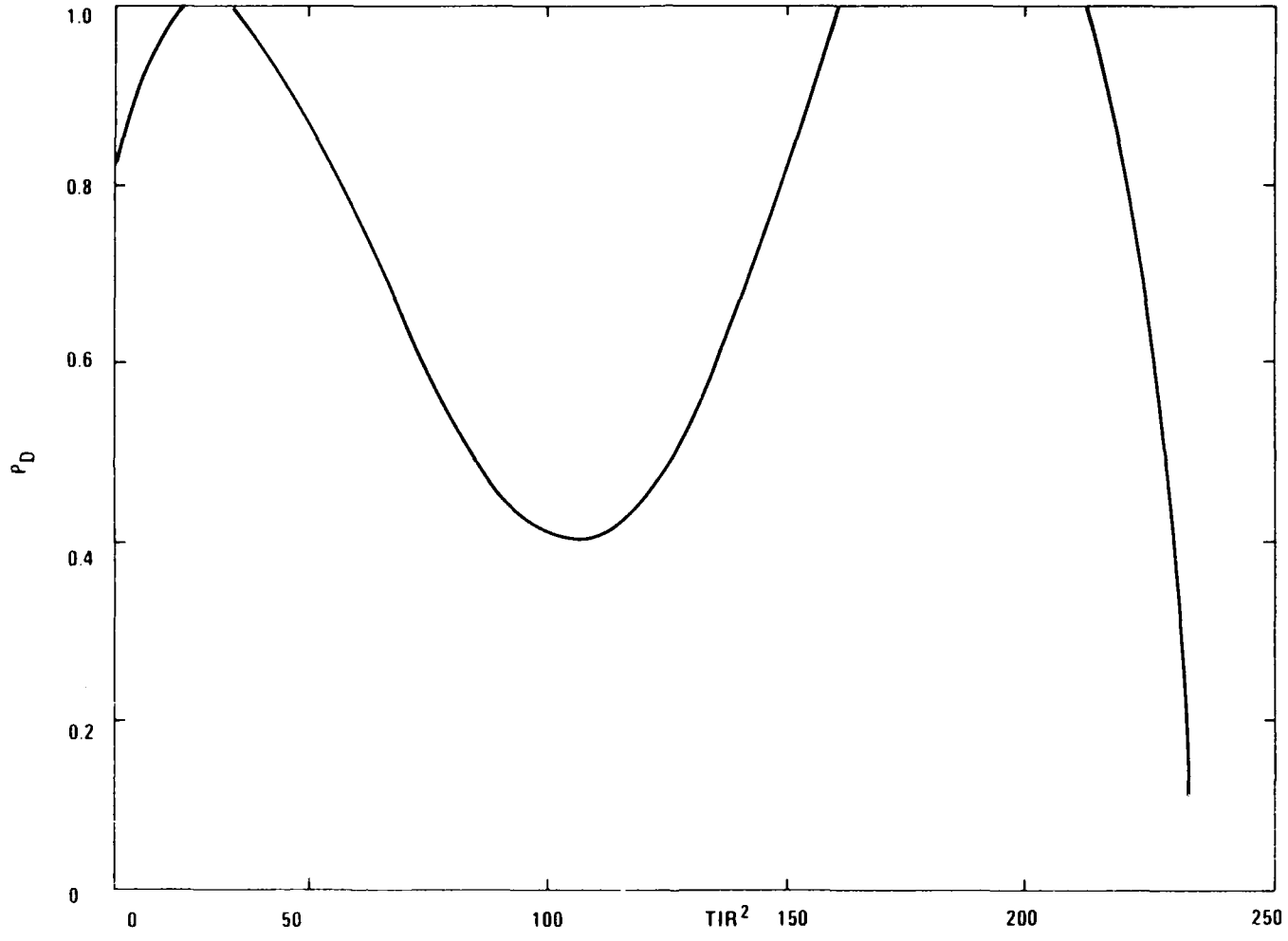

Figure 3-54. Model of P_D vs. TIR^2

The standard deviation of the error was 0.16555466. This curve is displayed in Figure 3-55. Again the P_D value increases, remains high, and then decreases and goes up again. The range of high confidence in the model is <2000 for ESR. Causes of the downward behavior of P_D for ESR values of >1000 need to be explored.

For P_D vs. range, the following expression is derived:

$$P_D = 0.7 \tag{12}$$

The standard deviation of the error was 9.084×10^{-2}. This curve is displayed in Figure 3-56. As can be seen, P_D is insensitive to range vaiues. This is partly due to the fact that range variations for the sequential data were small. Consequently, the only data available were at relatively the same ranges.

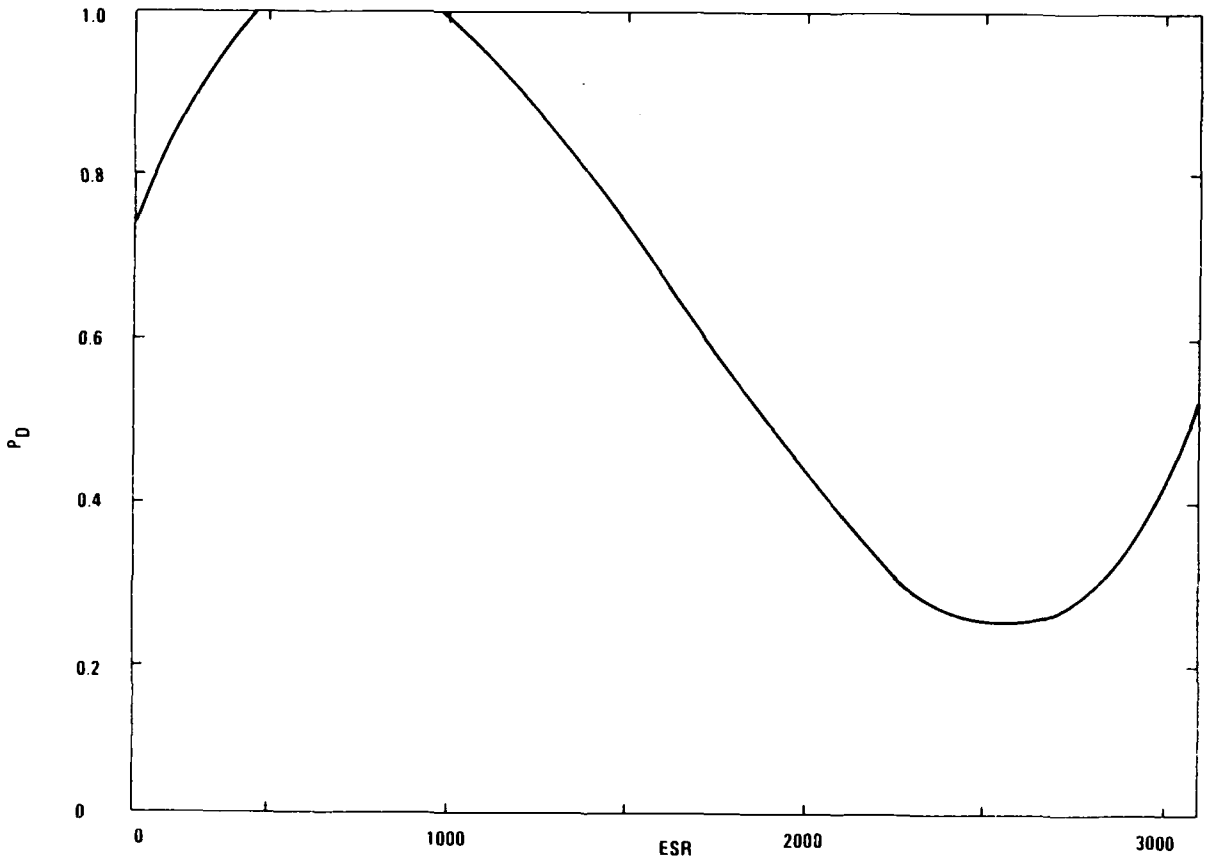

Figure 3-55. Model of P_D vs. ESR

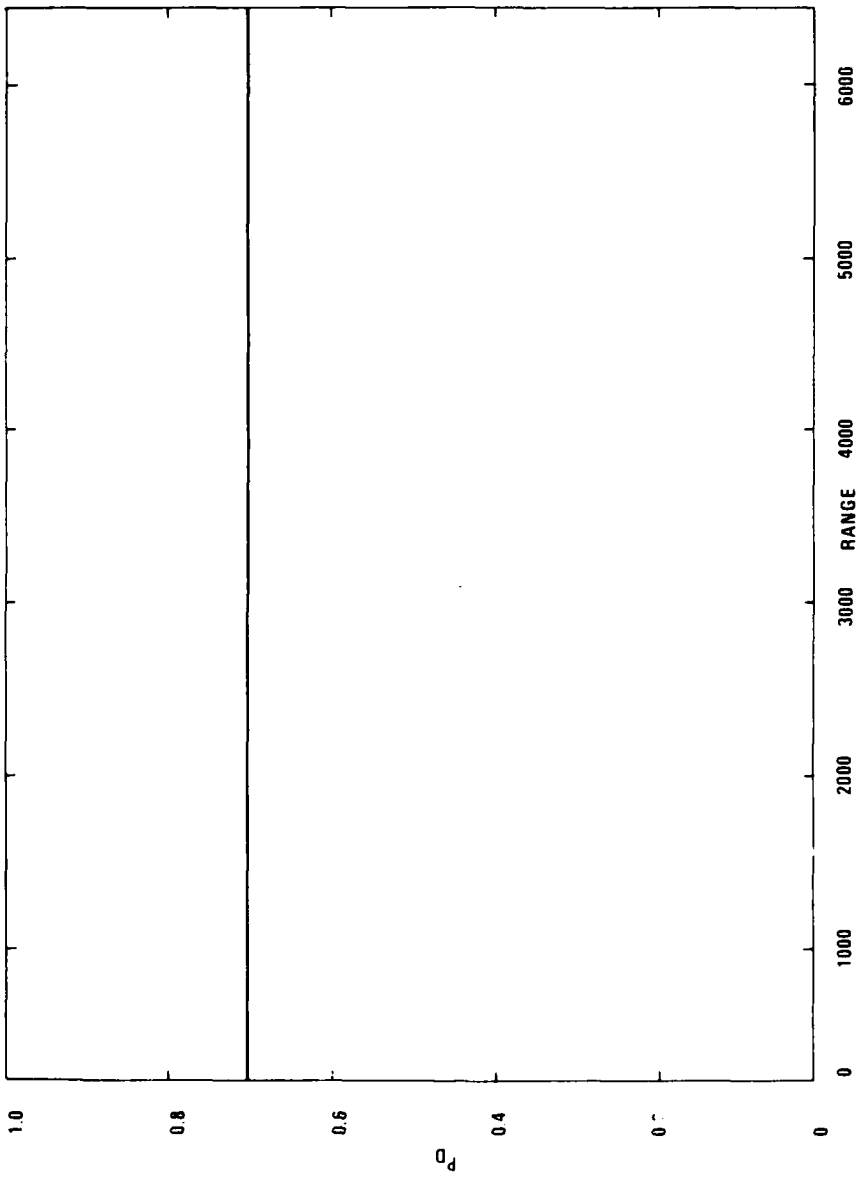

Figure 3-56. Model of P_D vs. Range

SECTION 4

TBL INVESTIGATION

4.1 A BRIEF DESCRIPTION OF TBL

Honeywell's texture boundary locator (TBL) is a texture segmentation algorithm. TBL uses intensity, mean and variance texture measures as the features for region discrimination. It also uses spatial gradient information in the texture domain to aid in the distinction between ranges. Figure 4-1 is the flow diagram of the TBL algorithm. The texture attributes of each pixel, namely the n x n window mean m and the window standard deviation s, are computed. Next, a texture gradient is computed using a window operator in the texture space as follows: A 2k x 2k window is selected. The window about the pixel p looks like:

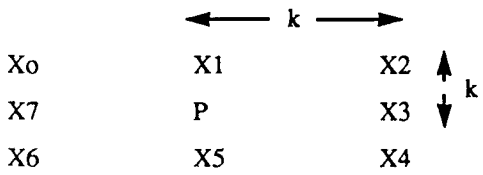

where $X_i = (m_i, s_i)$, the pair determined from an n x n window about the pixel in the X_i location in the original image. The texture measure is calculated by:

$$Tex = \max[(m_i - m_{i+4})^2 + (s_i - s_{i+4})^2]^{1/2} \qquad (13)$$

where $0<i<3$. This measure, a metric in (m,s) space, computes the change in texture at a distance k about the pixel p.

Next, the histogram of the gradient image, which is employed as a global information measure, is used as a threshold to guide prototype selection. Specifically, the threshold is set to select a certain percentage of the high intensity gradient points such that a sufficiently large number of pixels are included. Then edge thinning is applied to locate the prototypes. Finally, a pixel-to-label mapping and connected component analysis generates the segmentation by labeling all pixels inside the prototypes as potential target regions and those outside as other regions.

Three parameters (n, k, p) are needed to operate this algorithm.

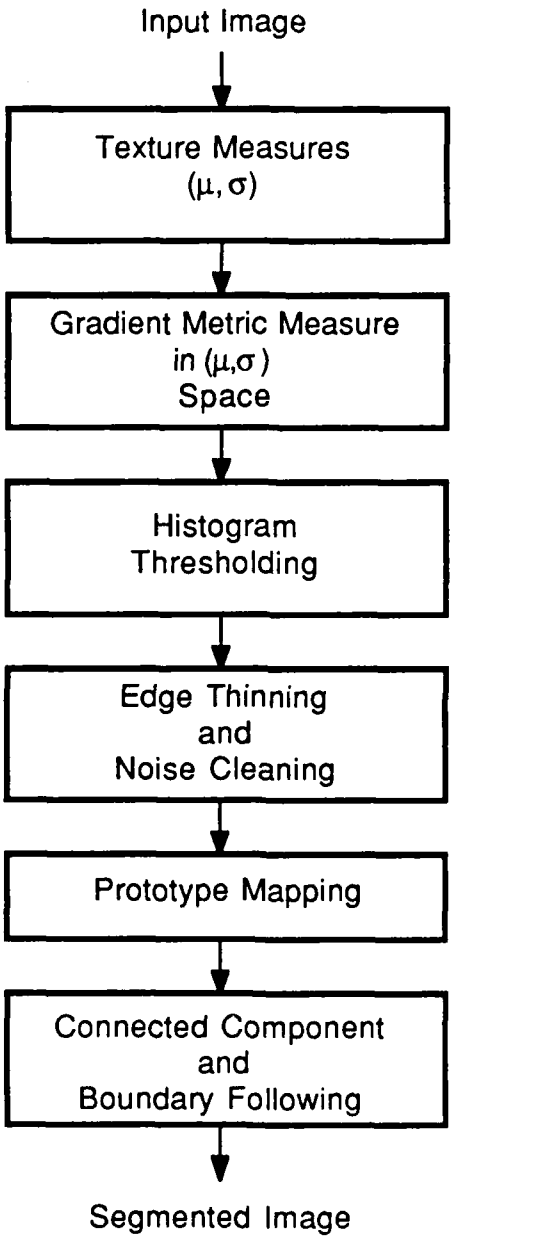

Figure 4-1. Target Boundary Locator Segmentor

4.2 TBL SENSITIVITY ANALYSIS EXPERIMENT

The objective of this experiment is to investigate the variations of the TBL segmentation accuracy as the three parameters are varied. The outcome of this investigation, which provides insight into the sensitivities of the segmentation accuracy with respect to the (n, k, p) set, is used for the appropriate selection of the parameters for a particular data base.

In our first experiment we used the 29-palm data base. The first 28 images in this data base were divided into two major groups based on the similarities of the member of each group. From each group a single typical image was selected. Then a 3x3x4 factorial design was performed, and a total of 36 runs on each frame were made. Figures 4-2 and 4-3 show the selected frames for this study.

The parameters n and k were varied by three different values. The parameter p varied by four different values since past experience had suggested that it was the most sensitive of the three parameters. Figures 4-4, 4-5, and 4-6 show the variations of segmentation accuracy vs. the percent parameter p for three different values of n and k for one of the frames. As can be seen from Figure 4-4, SA achieved a maximum at p = 0.25 for n=4 and k=6. As we increased the value of n from 4 to 5, the maximum SA reached its peak at n=5, k=7 and p = 0.35. Moreover, the value of maximum increased also from about 0.31 to about 0.36. Figure 4-5 shows the effect of increasing n to 6. In this case, SA achieved its highest value of 0.41 at n=6, k=6, & p=0.35. Consequently, the best result was achieved at n=6, k=6, and p=0.35.

Figures 4-7, 4-8, and 4-9 show the variations of SA for the second frame as functions of n, k, and p. SA achieved its highest value of 0.48 at n=6, k=7 or 8, and p=0.15 as seen from Figure 4-9.

Based on the results of this experiment, an average appropriate parameter set was derived. This set was then used for the 28 frames from 29-palm data base.

4.3 TBL PERFORMANCE ON 29-PALM DATABASE

Twenty-eight frames from the 29-palm data base were segmented by the TBL, and the segmentation accuracy performance measures were derived.

Figures 4-10, 4-11, and 4-12 show the variations of the SA values vs. TIR^2, $TBIR^2$ and ESR metrics for the 29-palm data set.

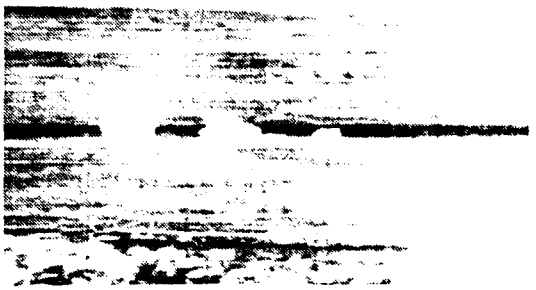

Figure 4-2. First Frame from 29-Palm Used in the Sensitivity Analysis Study

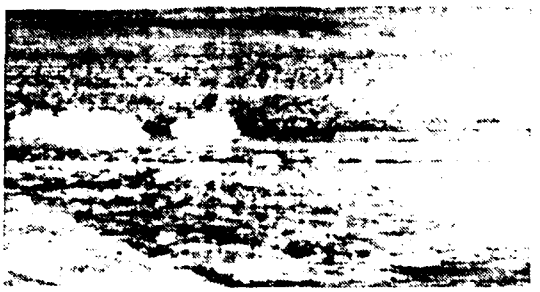

Figure 4-3. Second Frame from 29-Palm Used in the Sensitivity Analysis Study

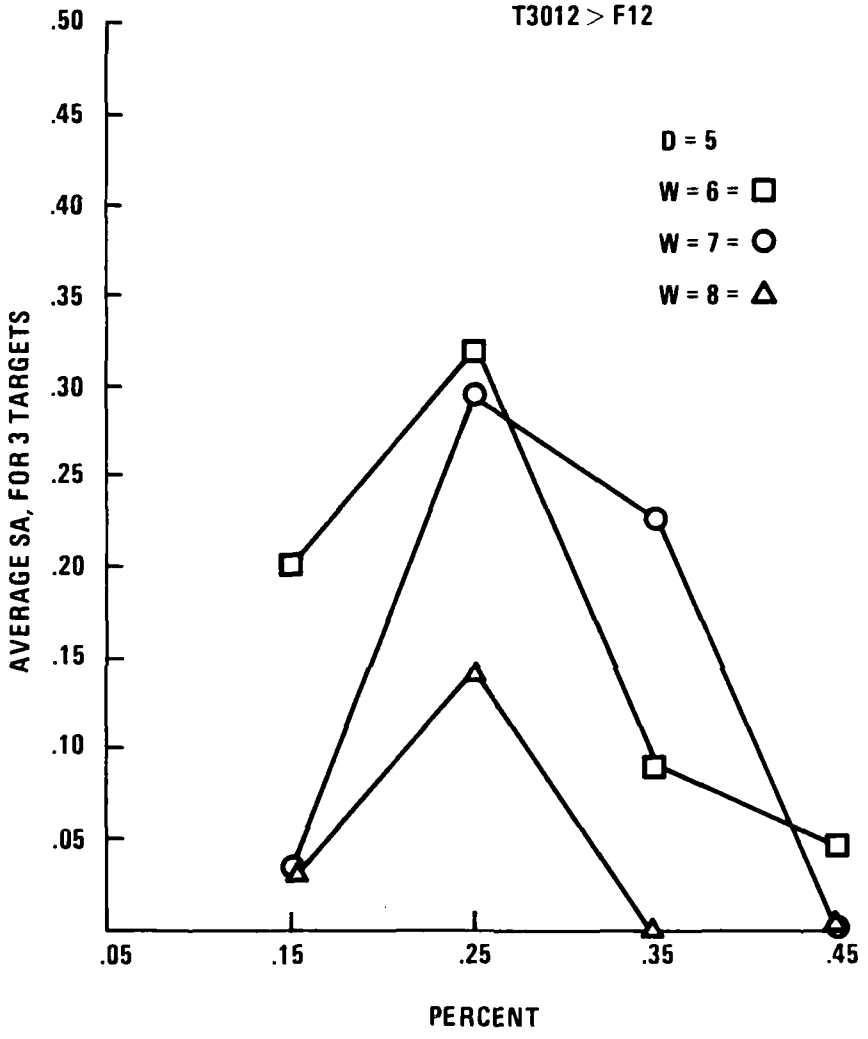

Figure 4-4. Variation of Mean SA as Percent Value p Varies for k=4 and n=w=6, 7, and 8

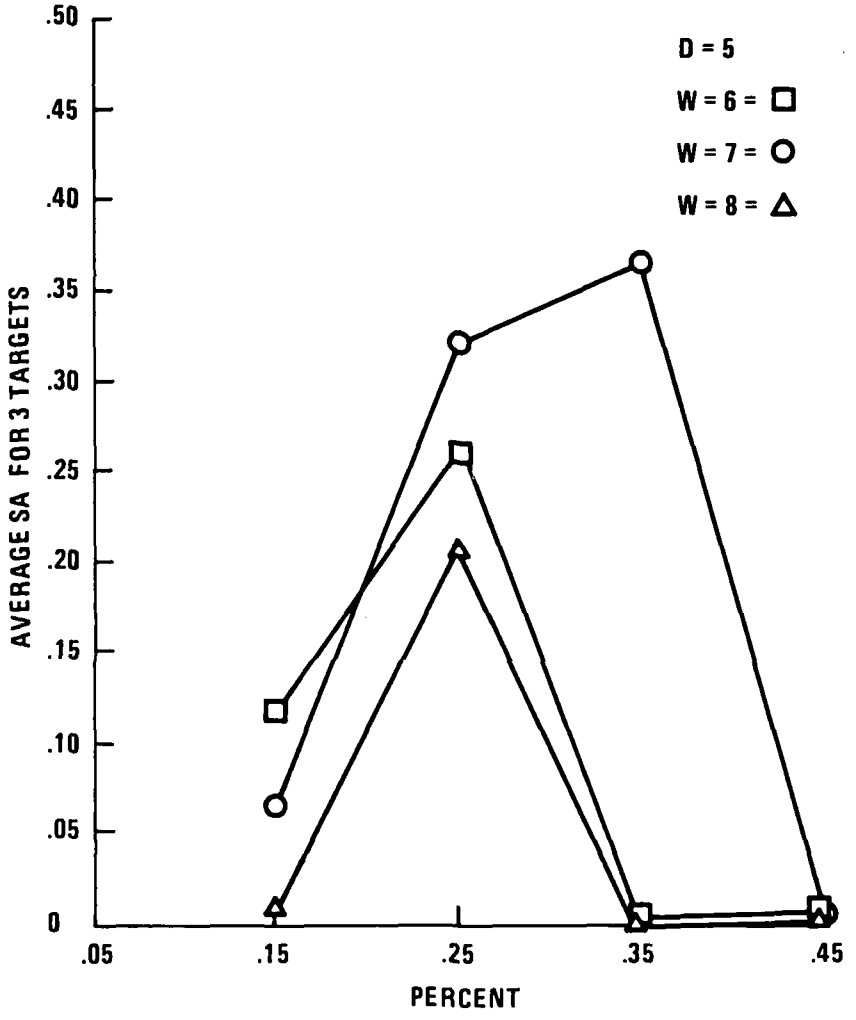

Figure 4-5. Variation of Mean SA as Percent Value p Varies for k=D=5 and n=w=6, 7, and 8

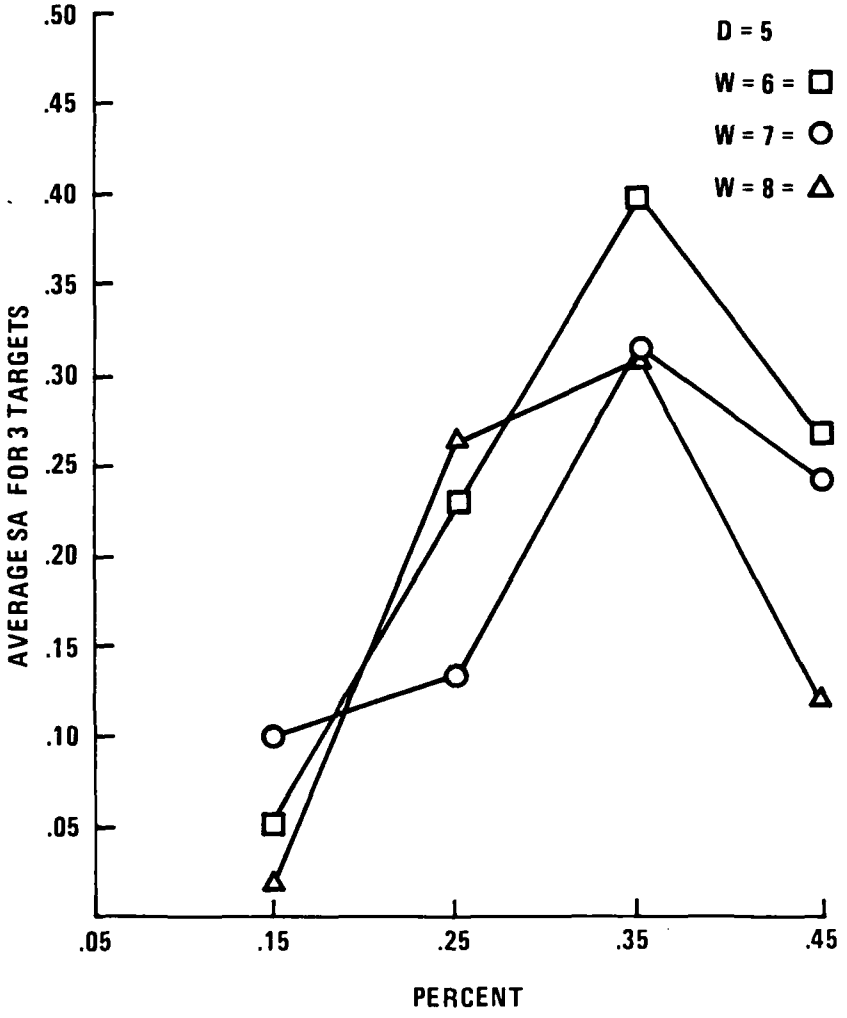

Figure 4-6. Variation of Mean SA as Percent Value p Varies for k=D=6 and n=6, 7, and 8

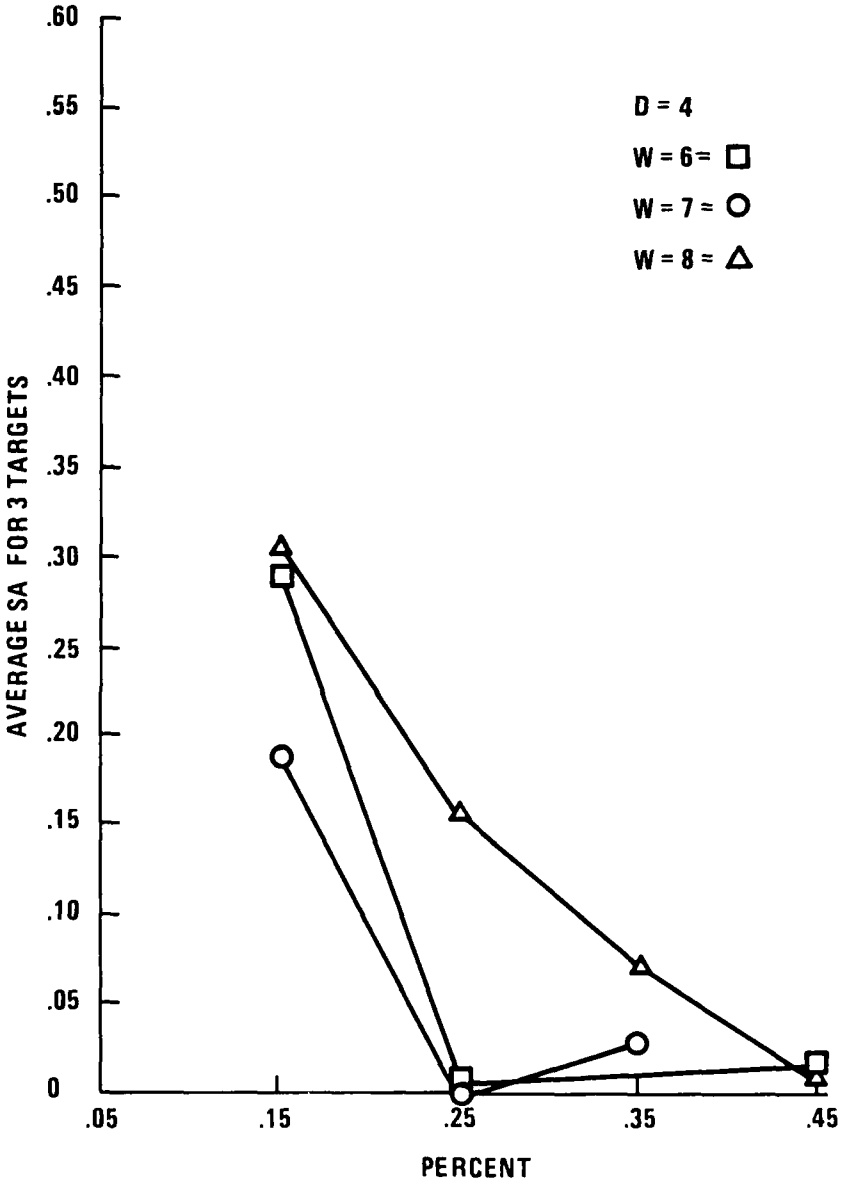

Figure 4-7. Variation of Mean SA as Percent Value p Varies for k=D=4 and n=w=6, 7, and 8

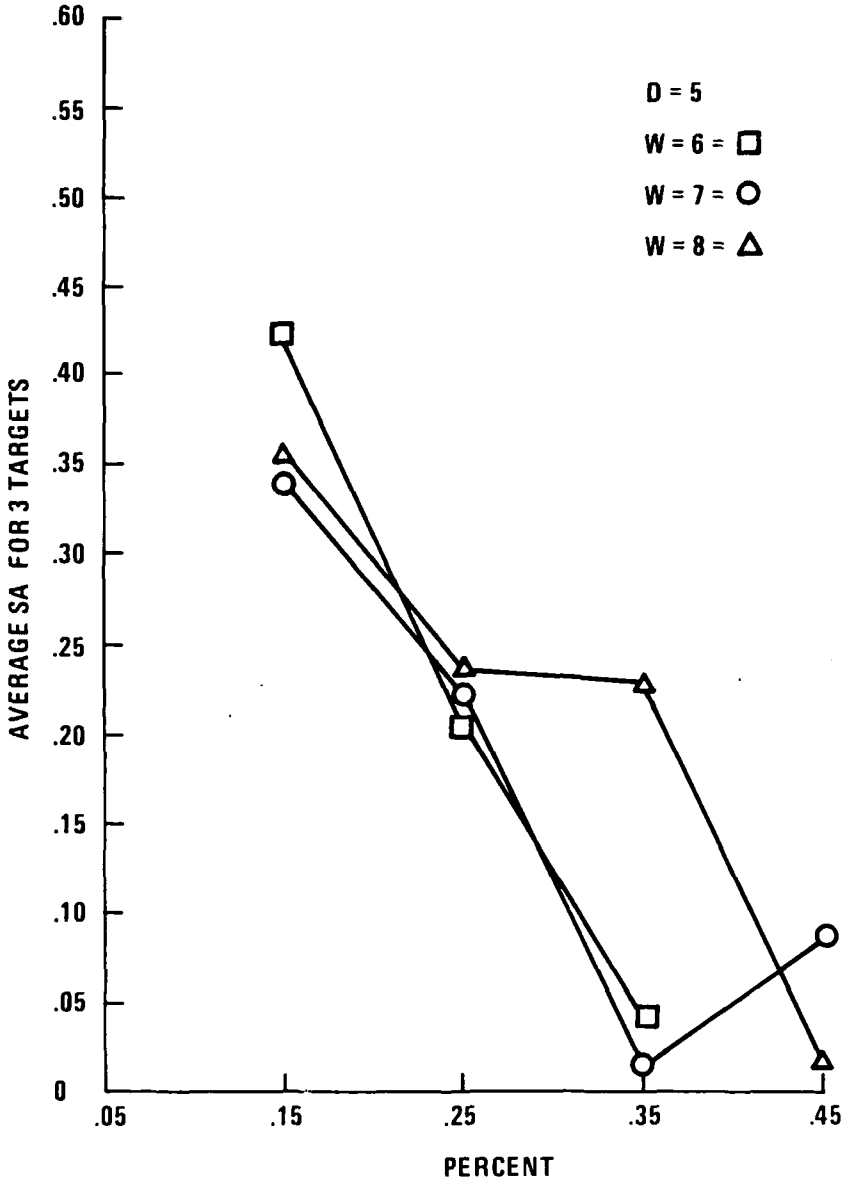

Figure 4-8. Variation of Mean SA as Percent Value p Varies for k=D=5 and n=w=6, 7, and 8

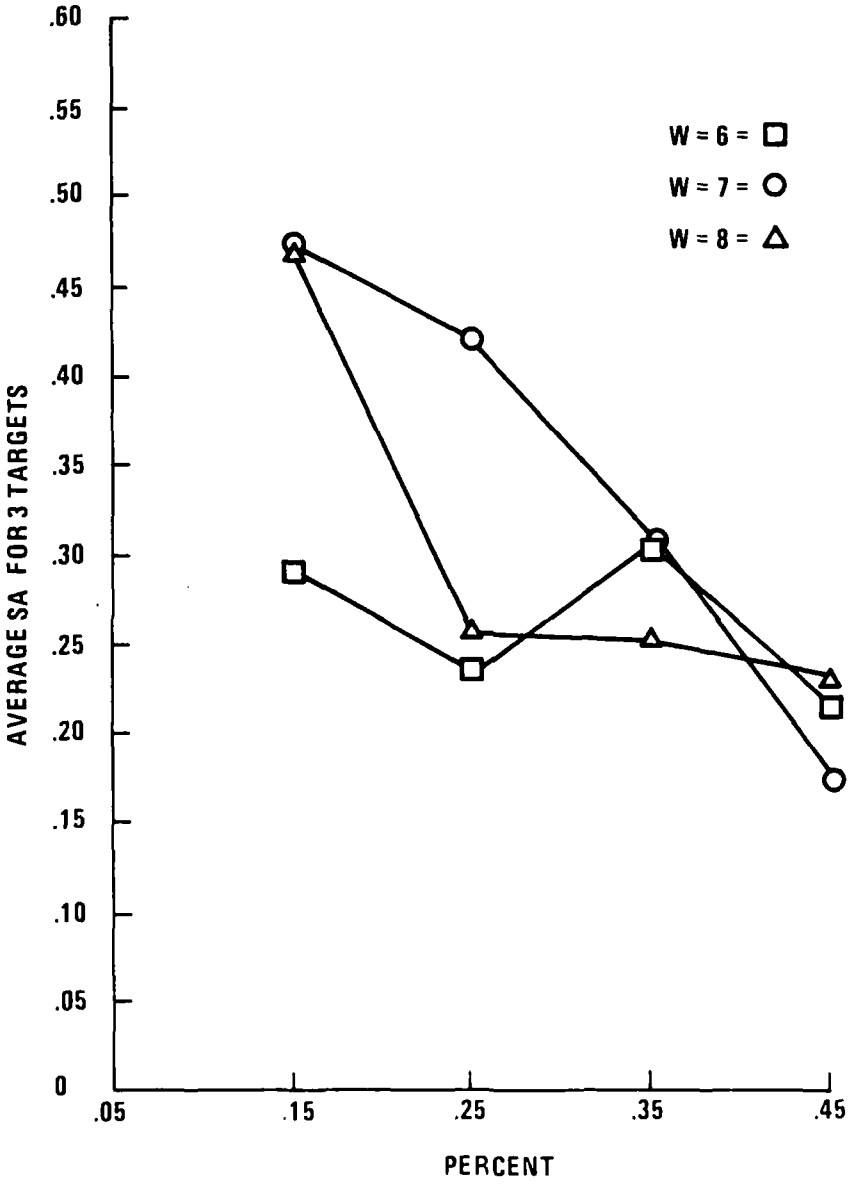

Figure 4-9. Variation of Mean SA as Percent Value p Varies for k=D=6 and n=w=6, 7, and 8

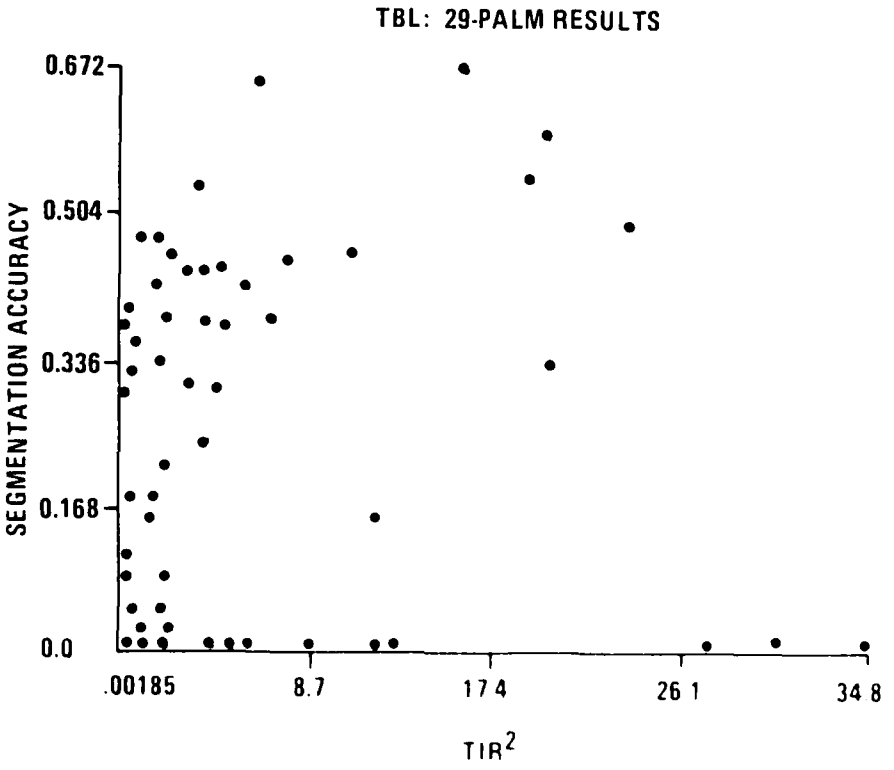

Figure 4-10. Variation of Segmentation Accuracy as TIR^2 Varies for 29 Frames from 29-Palm Data Base

AD-A188 698 PASSIVE AUTONOMOUS INFRARED SENSOR TECHNOLOGY(U) 2/2
HONEYWELL SYSTEMS AND RESEARCH CENTER MINNEAPOLIS MN
F SADJADI OCT 87 87SRC17 DAAL02-85-C-0134

UNCLASSIFIED F/G 17/5.1 NL

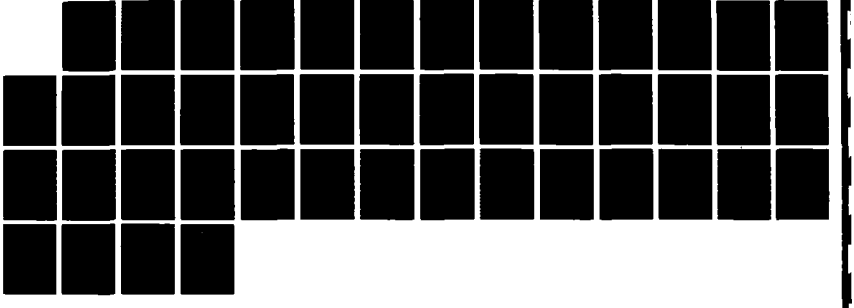

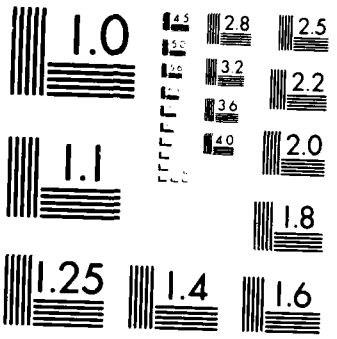

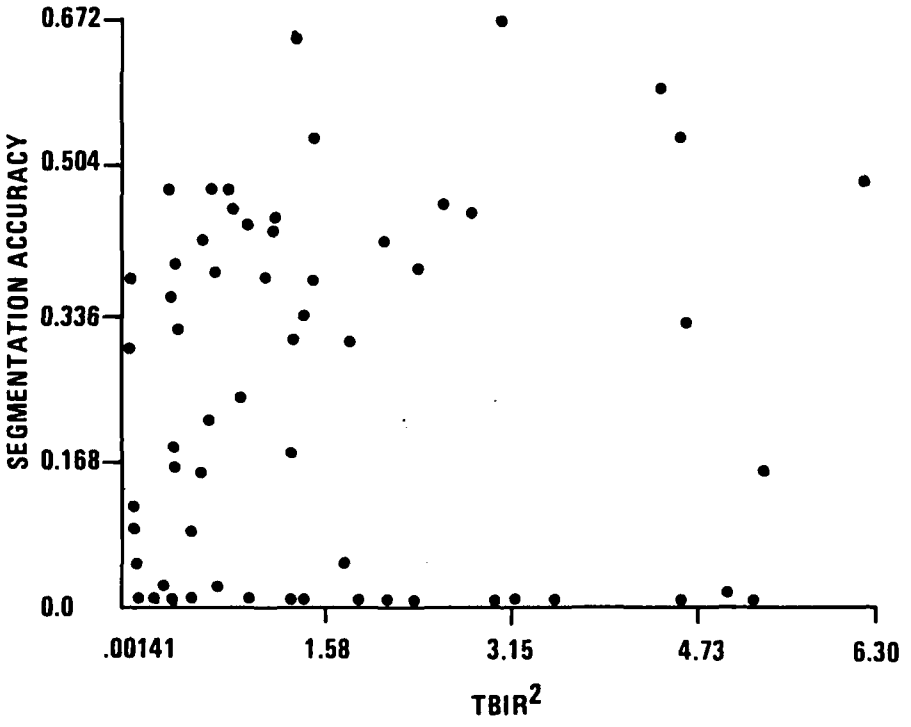

Figure 4-11. Variation of Segmentation Accuracy as $TBIR^2$ Varies for 28 Frames from 29-Palm Data Base

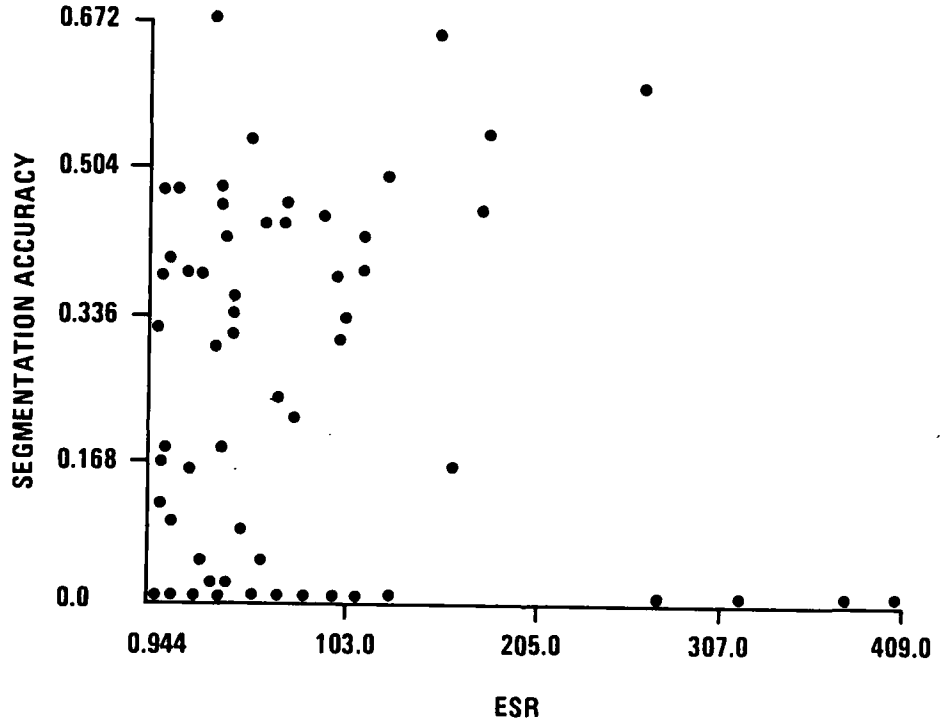

Figure 4-12. Variation of Segmentation Accuracy as ESR Varies for 28 Frames from 29-Palm Data Base

4.3.1 SA vs. TIR^2

As can be seen from Figure 4-10, for the TIR^2 values in the first bin ($0.00185<TIR^2<8.70$), SA has a mean value of 0.30. In the second bin ($8.7<TIR^2<0.7.4$), the SA average was 0.43. In the third bin ($17.4<TIR^2<26.1$), the SA average was 0.49. Finally, in the fourth bin ($26.1<TIR^2<34.0$), the SA average was 0.01, due to only one sample that produced this SA value.

4.3.2 SA vs. $TBIR^2$

Figure 4-11 shows the variations of SA vs. $TBIR^2$ metrics. In the first bin ($0.00141<TBIR^2<1.58$), the SA average was 0.29. In the second bin ($1.58<TBIR^2<3.15$), the SA average was 0.37. In the third bin ($3.15<TBIR^2<4.73$), the SA average was at 0.63. Finally, of the fourth bin ($4.73<TBIR^2<6.3$), the SA average was 0.31.

4.3.3 SA vs. ESR

Figure 4-12 shows the variations of SA vs. ESR metrics. In the first bin ($0.944<ESR<103$), the SA average was 0.30. In the second bin ($103<ESR<205$), the SA average was 0.41. In the third bin ($205<ESR<307$), the SA average was 0.30. Finally, in the fourth bin ($307<ESR<409$), there was only one sample due to one target that was not detected.

In the above analysis we have excluded the samples that produced SA values of 0 in the computation of average SA values.

4.4 TEXAS INSTRUMENT DATA BASE RESULTS

In this experiment, a total of 136 frames containing 372 targets were used. There were three different sets of data in the TI data base, which we refer to as T3002 to T3004. In the following, the results for each set are reported separately.

4.4.1 T3002 Set Results

Figure 4-13 shows the variations of SA as function of TIR^2. In the first bin ($0<TIR^2<37.5$), the average segmentation accuracy was 0.33. In the second bin ($37.5<TIR^2<75$), the average SA was 0.47. In the third bin ($75<TIR^2<113$), the average value of SA was 0.49. Finally, in the fourth bin, the average SA value was 0 due to the one target that was not detected.

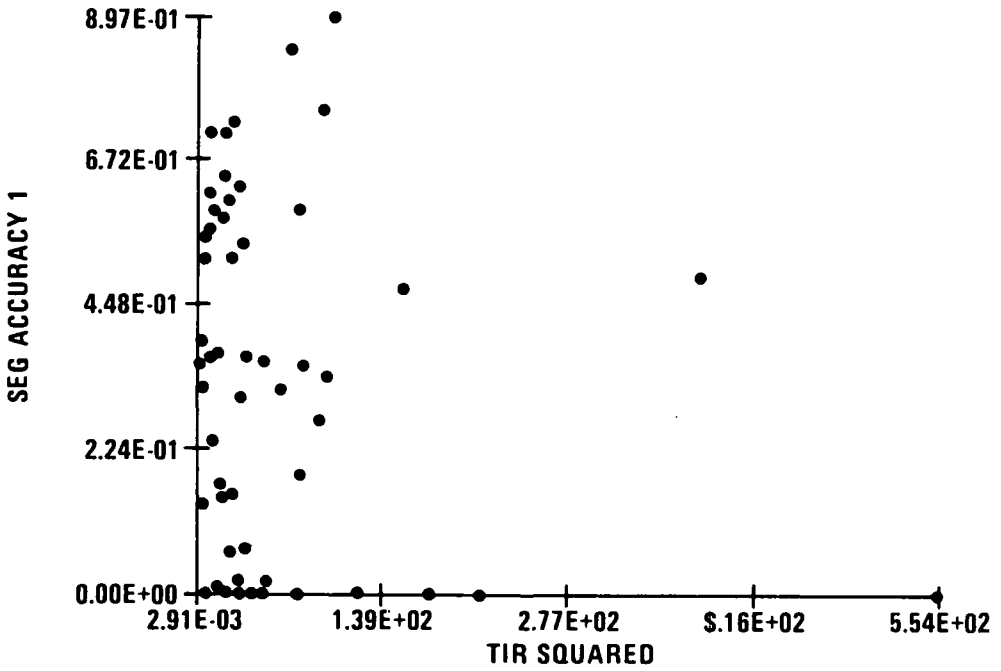

Figure 4-13. Variation of Segmentation Accuracy as a Function of TIR^2 for the T3002 TI Data Base

4.4.1.1 Variation of SA vs. $TBIR^2$–Figure 4-14 shows the variations of SA as a function of $TBIR^2$. In the first bin ($1.43x10\text{-}3<TBIR^2<7.17$), the average SA value was 0.33. In the second bin ($7.17\leq TBIR^2\leq 14.3$), the average SA value was 0.29. In the third bin ($14.3<TBIR^2\leq 21.5$), the average SA value was 0.69. Finally, in the fourth bin ($21.5<TBIR^2\leq 28.7$), the average SA value was down to 0.36.

4.4.1.2 Variation of SA vs. ESR–Figure 4-15 shows the variations of SA as a function of ESR. In the first bin ($0\leq ESR\leq 750$), the average SA was 0.33. In the second bin ($750<ESR\leq 1500$), the average SA was 0.61. In the third bin ($1500<ESR\leq 2250$), the average SA was 0.49 due to only one sample. Finally, in the fourth bin ($2250<ESR\leq 3000$), the average value of SA was 0 due to one sample that was not detected.

4.4.2 T3003 Set Results

4.4.2.1 Variation of SA vs. TIR^2–Figure 4-16 shows the variations of the SA as a function of TIR^2. In the first bin ($0\leq TIR^2\leq 32.5$), the average SA value was 0.36. In the second bin ($32.5<TIR^2\leq 65$), the average SA value was 0.43. In the third bin ($65<TIR^2\leq 97.5$), the average value of SA was 0.36. In the fourth bin ($97.5<TIR^2\leq 130$), the average SA value was 0.6.

4.4.2.2 Variation of SA vs. $TBIR^2$–Figure 4-17 shows the variation of SA as a function of $TBIR^2$. In the first bin ($3x19^{-6}<TBIR2\leq 25.5$), the average SA value was 0.36. In the second bin ($25.5<TBIR^2<51.1$), the average SA value was 0.60. In the third and fourth bin ($51.1<TBIR^2<100$), there was only one sample due to a target that was not detected.

4.4.2.3 Variations of SA vs. ESR–Figure 4-18 shows the variation of SA as a function of ESR. In the first bin ($4.06\leq ESR\leq 1770$), the average SA value was 0.36. In the second bin ($1770<ESR\leq 3520$), the average SA value was 0.33. In the third bin ($3520<ESR\leq 5250$), the average SA was 0.28 due to one sample. Finally, in the fourth bin ($5250<ESR\leq 7000$), the average SA value was 0.52.

By expanding the first bin in four sub-bins, one obtains the following results: in the first sub-bin ($0\leq ESR\leq 475$), the average SA value was 0.32. In the second sub-bin ($47<ESR\leq 950$), the average SA value was 0.45. In the third sub-bin ($960<ESR\leq 1430$), the average SA value was 0.56. Finally, in the fourth bin ($1430<ESR\leq 1900$), the average SA value was 0.43.

4.4.3 T3004 Set Results

4.4.3.1 Variation of SA vs. TIR^2–Figure 4-19 shows the variation of SA as a function of TIR^2. In the first bin ($3.74x10^{-3}\leq TIR^2\leq 76.5$), the average SA value was 0.38. In the second bin ($76.5<TIR^2\leq 153$), the average SA value

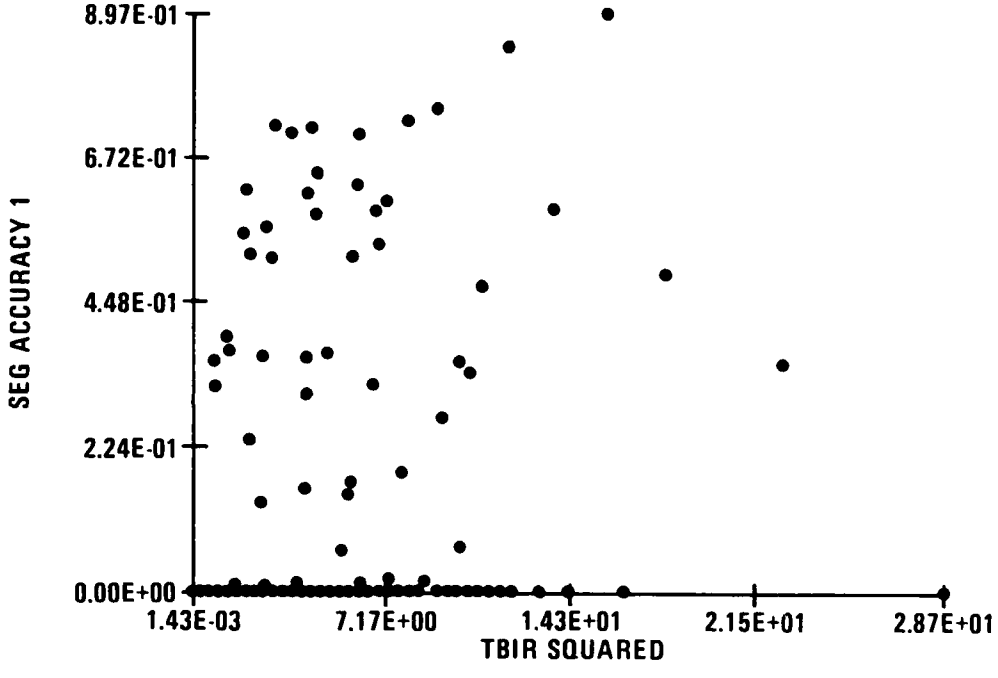

Figure 4-14. Variation of Segmentation Accuracy as a Function of $TBIR^2$ for the T3002 TI Data Base

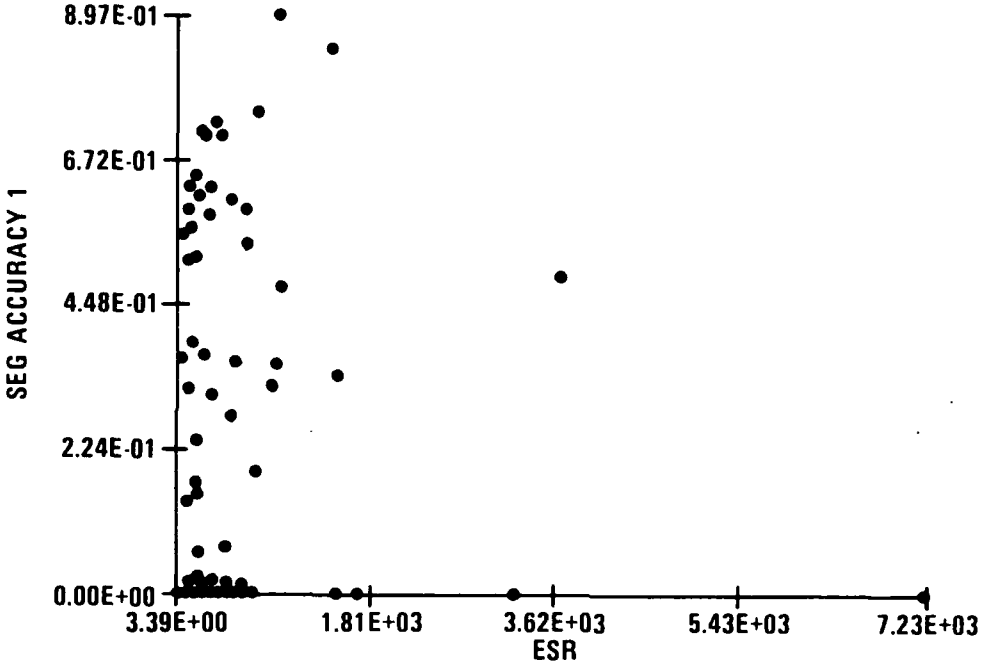

Figure 4-15. Variation of Segmentation Accuracy as a Function of ESR for the T3002 TI Data Base

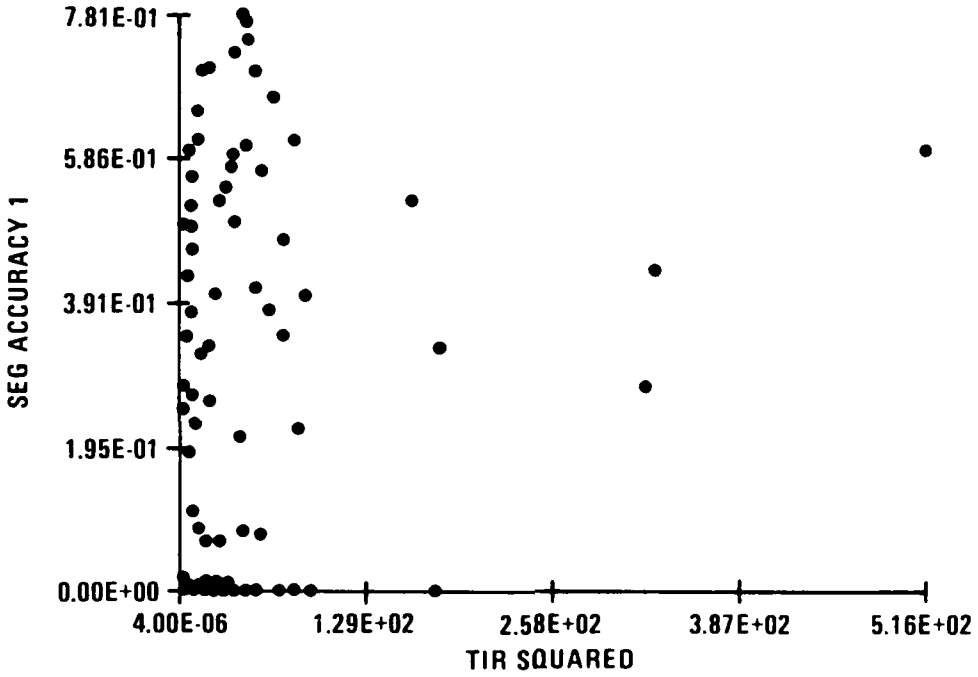

Figure 4-16. Variation of Segmentation Accuracy as a Function of TIR^2 for the T3003 TI Data Base

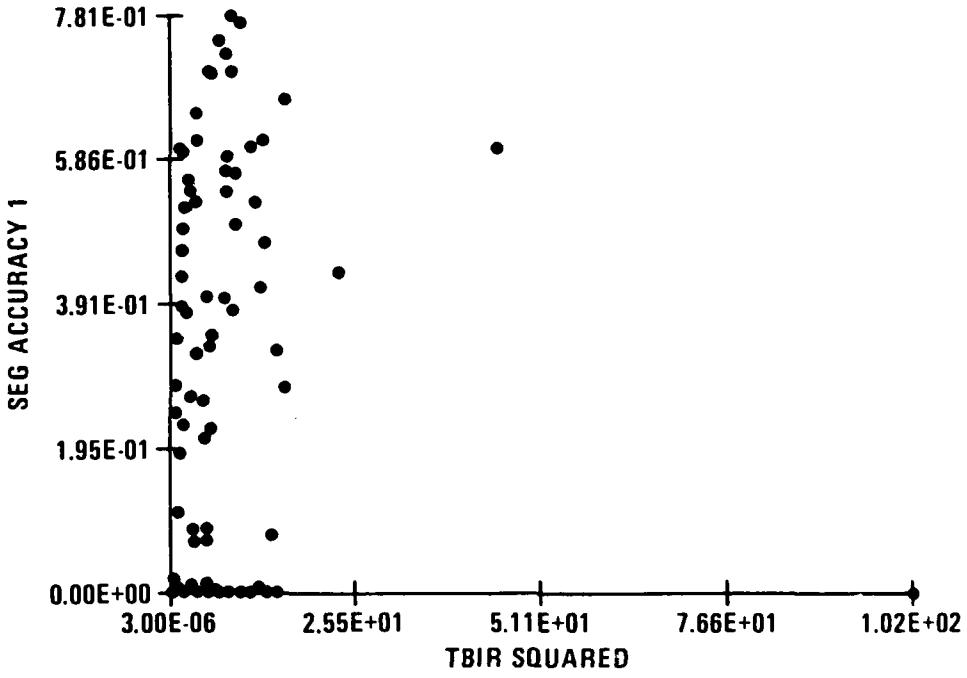

Figure 4-17. Variation of Segmentation Accuracy as a Function of $TBIR^2$ for the T3003 TI Data Base

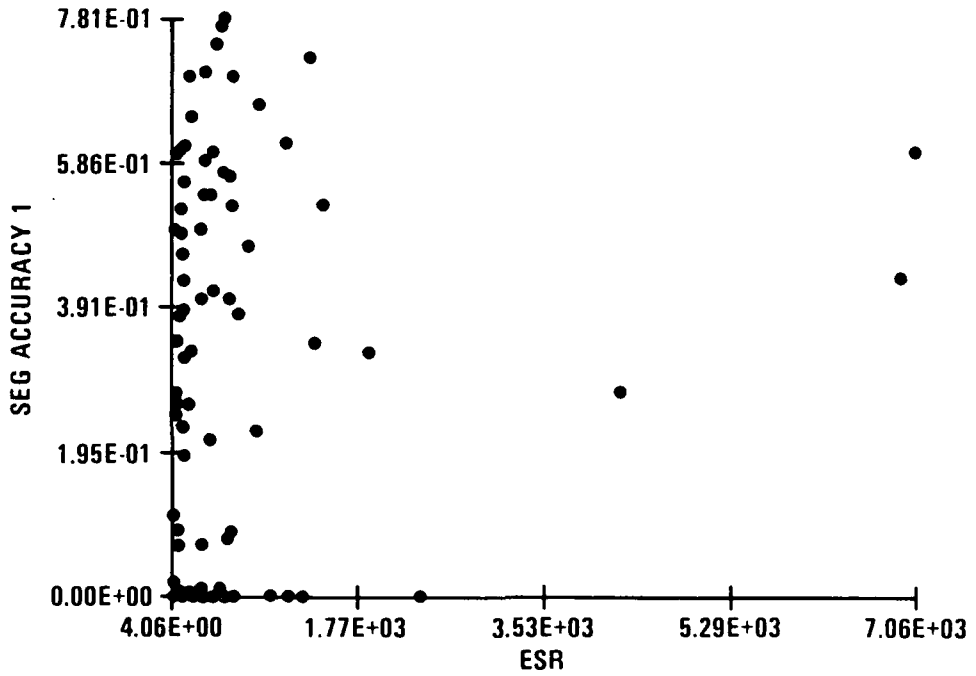

Figure 4-18. Variation of Segmentation Accuracy as a Function of ESR for the T3003 TI Data Base

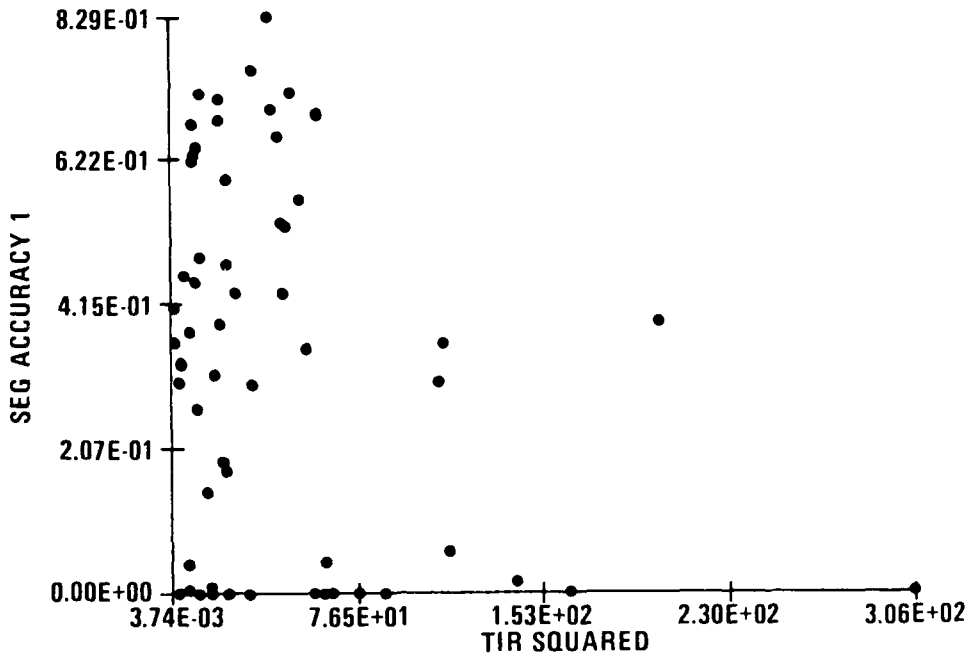

Figure 4-19. Variation of Segmentation Accuracy as a Function of TIR^2 for the T3004 TI Data Base

was 0.18. In the third bin ($153<TIR^2\leq230$), the average SA value was 0.39 due to only one sample. In the fourth bin ($230<TIR^2\leq306$), only one sample was located, which was due to one target that was not detected. By expanding the first two bins into four equal-size bins, one obtains the following results. In the first sub-bin ($0\leq TIR^2\leq37.5$), the average SA was 0.33. In the second sub-bin ($37.5<TIR^2\leq75.0$), the average SA was 0.55. In the third sub-bin ($75.0<TIR^2\leq113$), the average value of SA was 0.33. Finally, in the fourth sub-bin ($113<TIR^2\leq150$), the average SA value was 0.03.

4.4.3.2 Variation of SA vs. $TBIR^2$–Figure 4-20 shows the variation of segmentation accuracy as a function of $TBIR^2$. In the first bin ($4.10\times10^{-3}\leq TBIR^2\leq8.50$), the average SA value was 0.34. In the second bin ($8.50<TBIR^2\leq17.0$), the average SA value was 0.42. In the third bin ($17.0<TBIR^2\leq25.5$), the average SA value was 0.57. In the fourth bin ($25.5<TBIR^2\leq34.0$), there was only one sample due to one target that was not detected.

4.4.3.3 Variation of SA vs. ESR–Figure 4-21 shows the variation of SA as a function of ESR. In the first bin ($3.03\leq ESR\leq436$), the average SA value was 0.34. In the second bin ($436<ESR\leq860$), the average SA value was 0.43. In the third bin ($860<ESR\leq1300$), the average value of SA was 0.01 mainly due to one target.

4.4.4 Variation of SA vs. Range for TI and 29-Palm Data Bases

Figure 4-22 shows the variation of SA as a function of range for the T3002 data set. As can be seen, SA attains its highest values at ranges between 3000 to 5470 and then decreases. The highest SA is 0.897.

Figure 4-23 shows the variation of SA vs. range for the T3003 data set. In this data set, SA attains its highest values at ranges between 3010 to 5350 and then decreases. The highest value of SA is 0.781.

Figure 4-24 shows the variation of SA vs. range for the T3004 data set. SA attains its highest value of 0.825 at 3230. The highest SA value decreases to 0.6 at 5510 and then increases again to 0.72 at around 7000.

Figure 4-25 shows the variation of SA vs. range for the first 28 frames from 29-palm data base. There are three distinct ranges: 800, 1210, and 1770. In the highest SA occurs at 1770. At this range, the highest SA attains a value of 0.672.

4.5 PERFORMANCE OF TBL ON COMBINED DATA BASES OF TI AND 29-PALM

4.5.1 SA vs. TIR^2

Figure 4-26 shows the variation of SA as a function of TIR^2. In the first bin ($4.0\times10^{-6}\leq TIR^2\leq139$), SA has an average value of 0.35 and a standard deviation of 0.25. In the second bin ($139<TIR^2\leq277$), SA has an average

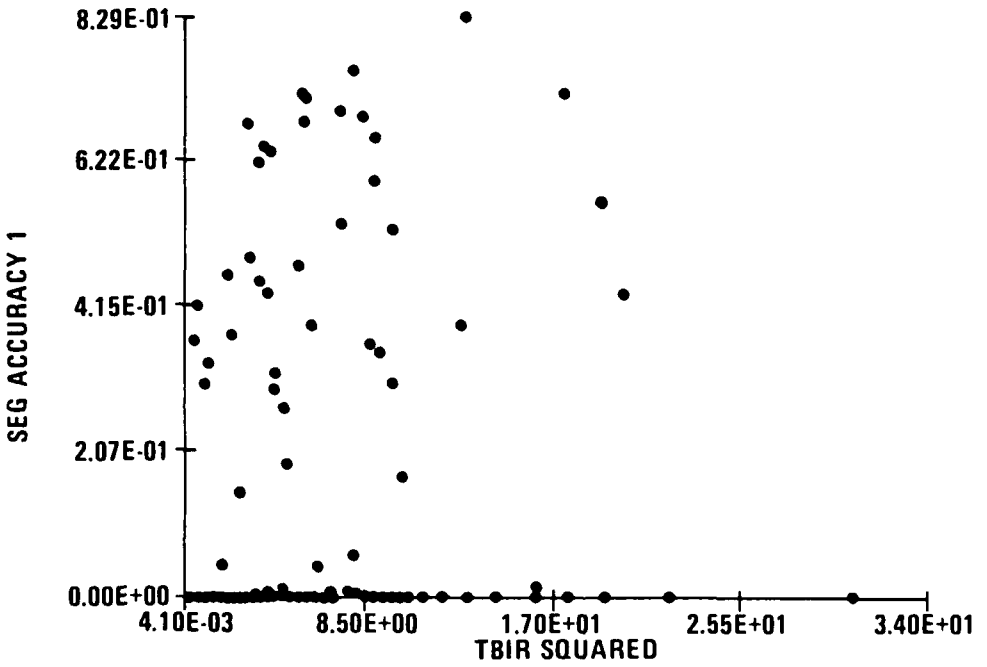

Figure 4-20. Variation of Segmentation Accuracy as a Function of $TBIR^2$ for the T3004 TI Data Base

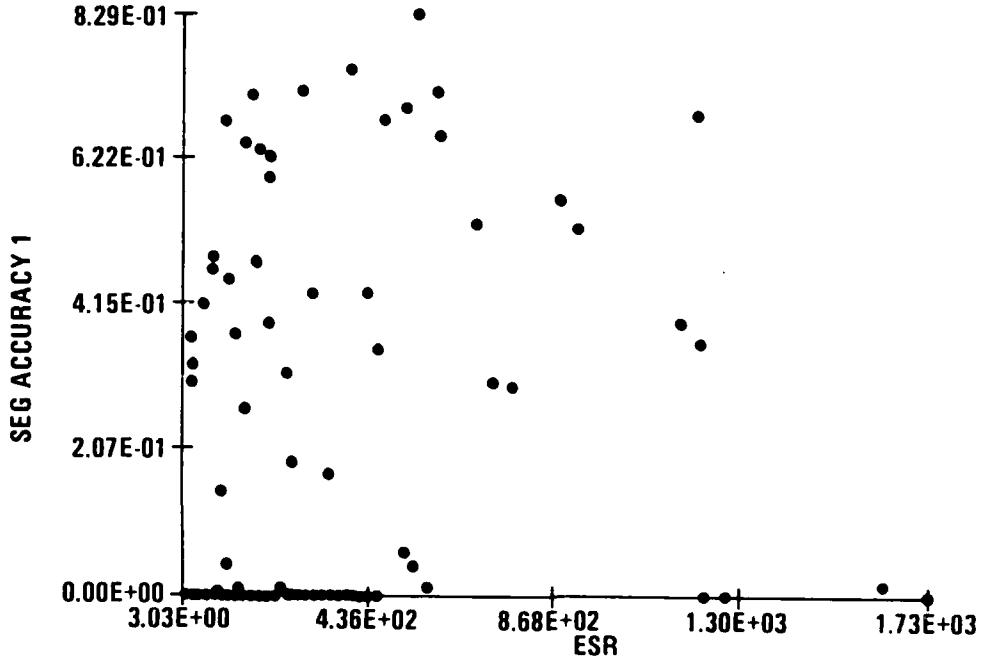

Figure 4-21. Variation of Segmentation Accuracy as a Function of ESR for the T3004 TI Data Base

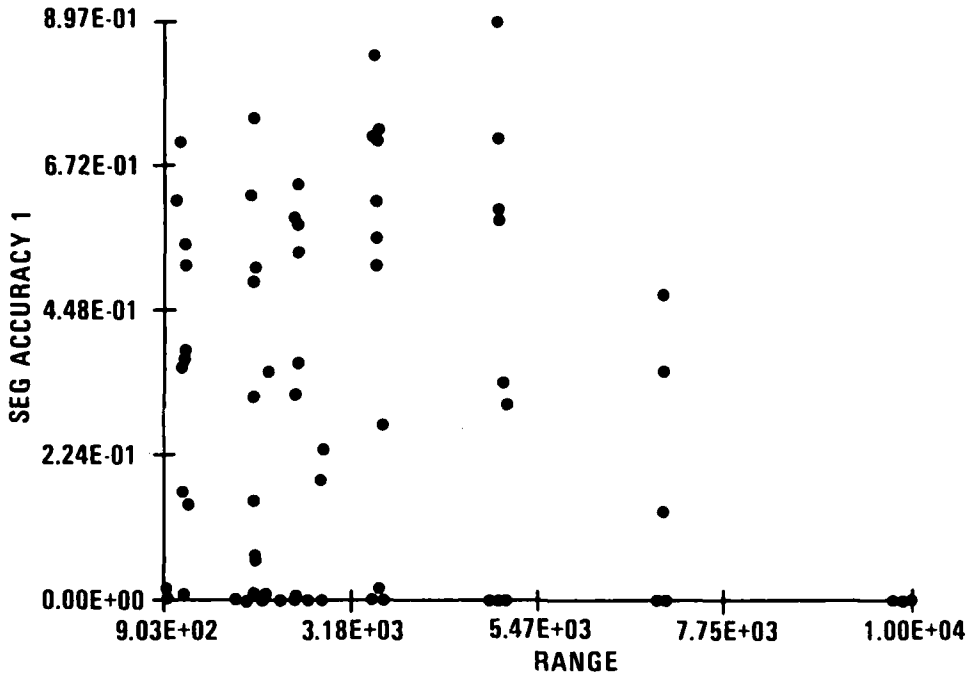

Figure 4-22. Variation of Segmentation Accuracy as a Function of Range for the T3002 Data Base

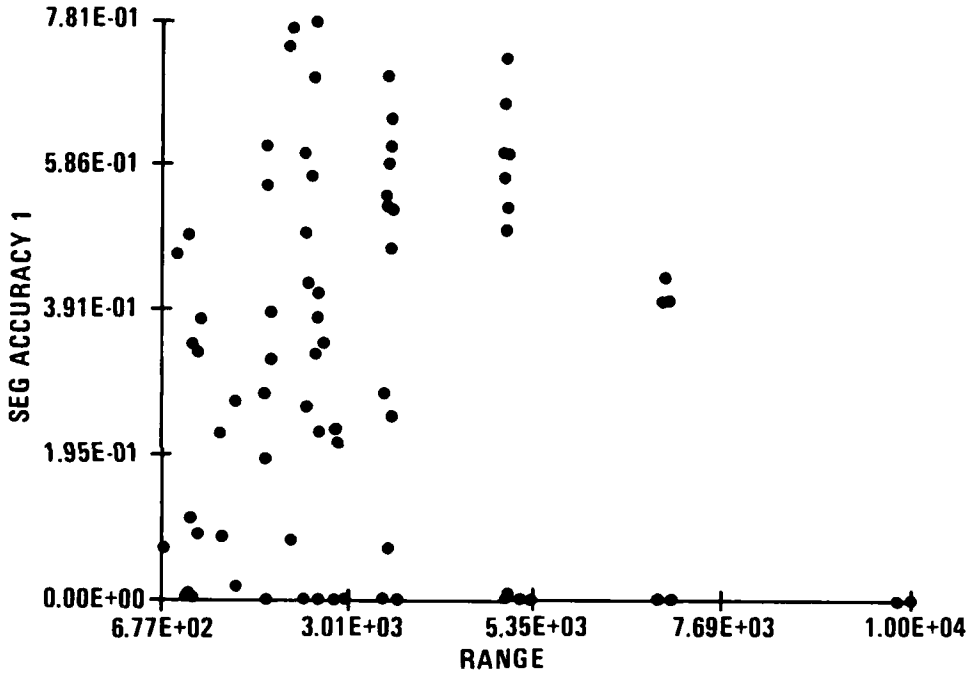

Figure 4-23. Variation of Segmentation Accuracy as a Function of Range for the T3003 TI Data Base

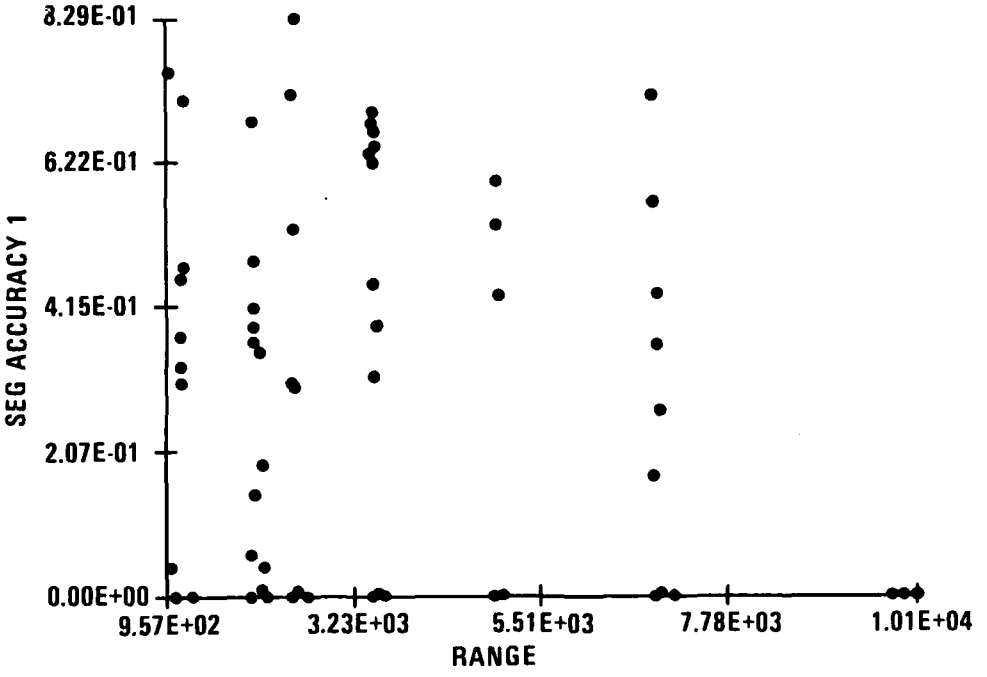

Figure 4-24. Variation of Segmentation Accuracy as a Function of Range for the T3004 TI Data Base

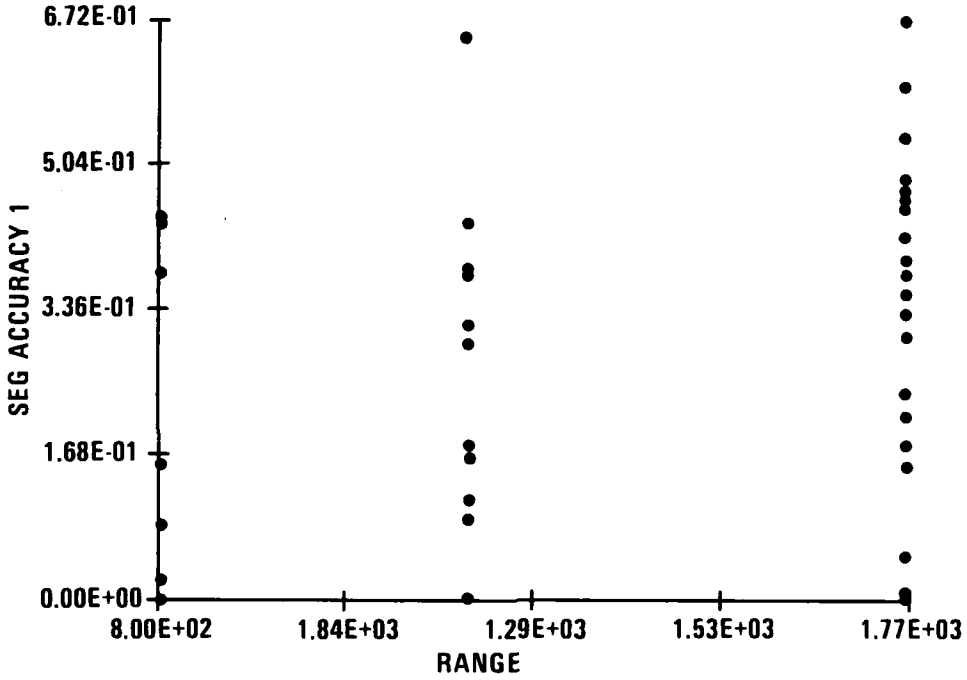

Figure 4-25. Variation of Segmentation Accuracy as a Function of Range for the 28 Frames from the 29-Palm Data Base

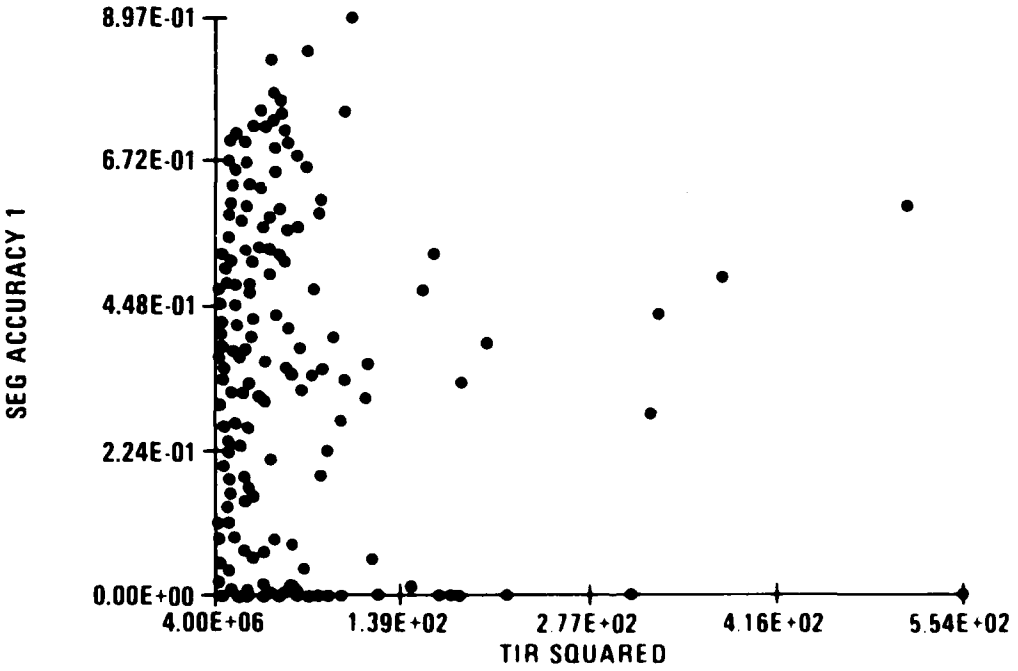

Figure 4-26. Variation of Segmentation Accuracy as a Function of TIR^2 for the Combined TI and 29-Palm Data Base

value of 0.35 and a standard deviation of 0.18. In the third bin ($277<TIR^2\leq416$), SA has an average value of 0.40 and a standard deviation of 0.09. In the fourth bin ($416<TIR^2\leq554$), SA has an average value of 0.60 and a standard deviation of 0 due to the only sample detected in this bin.

Figure 4-27 shows the variation of SA vs. TIR^2 for ($0\leq TIR^2\leq150$) only. By dividing this metric space into four equal and consecutive bins, one obtains the following results. In the first sub-bin ($0<TIR^2\leq37.5$), SA has an average value of 0.31 and a standard deviation of 0.24. In the second sub-bin ($37.5<TIR^2\leq75$), SA has an average of 0.49 and a standard deviation of 0.25. In third sub-bin ($75<TIR^2\leq113$), SA has an average value of 0.44 and a standard deviation of 0.21. In the fourth sub-bin ($113<TIR^2\leq150$), SA has an average of 0.03 and a standard deviation of 0.02 due to two detected targets.

4.5.2 SA vs. $TBIR^2$

Figure 4-28 shows the variation of SA as a function of $TBIR^2$. In the first bin ($3x10^{-6}\leq TBIR\leq25.5$), SA has an average value of 0.35 and a standard deviation of 0.24. In the second bin ($25.5<TBIR^2\leq51.5$), SA has an average value of 0.60 and a standard deviation of 0 due to the presence of only on sample in this bin. In the third bin ($51.1<TBIR^2\leq76.7$), no sample was available. In the fourth bin ($76\ 6<TBIR^2\leq102$), there was one target that was not detected. By expanding the values of $TBIR^2$ between 0 to 25, as shown in Figure 4-29, the following results are obtained. In the first sub-bin ($0\leq TBIR^2\leq6.25$), the SA has an average value of 0.32 and a standard deviation of 0.22. In the second sub-bin ($6.25<TBIR^2\leq12.5$), SA has an average value of 0.38 and a standard deviation of 0.28. In the third sub-bin ($6.25<TBIR^2\leq18.8$), SA has an average value of 0.46 and a standard deviation of 0.28. In the fourth sub-bin ($18.8<TBIR^2\leq25$), SA attains an average value of 0.45 and a standard deviation of 0.08.

4.5.3 SA vs. ESR

Figure 4-30 shows the variation of SA as a function of ESR. In the first bin ($0.944\leq ESR\leq1810$), SA has an average value of 0.35 and a standard deviation of 0.24. In the second bin ($1810<ESR\leq3620$), SA has an average of 0.33 and a standard deviation of 0 due to the presence of a single sample. In the third bin ($3620<ESR\leq5420$), SA has an average value of 0.39 and a standard deviation of 0.11. In the fourth bin ($5420<ESR\leq7230$), SA attains an average value of 0.52 and a standard deviation of 0.08. By expanding the ESR range between 0 to 1500, furthermore, as seen in Figure 4-31, one obtains the following: In the first sub-bin ($0\leq ESR\leq375$), SA has an average value of 0.32 and a standard deviation of 0.23. In the second sub-bin ($375<ESR\leq750$), SA has an average value of 0.40 and a standard deviation of 0.28. In the third sub-bin ($750<ESR\leq1130$), SA attains an average value of 0.52 and a standard deviation of 0.20. Finally, in the fourth sub-bin ($1130<ESR\leq1500$), SA has an average value of 0.56 and a standard deviation of 0.19.

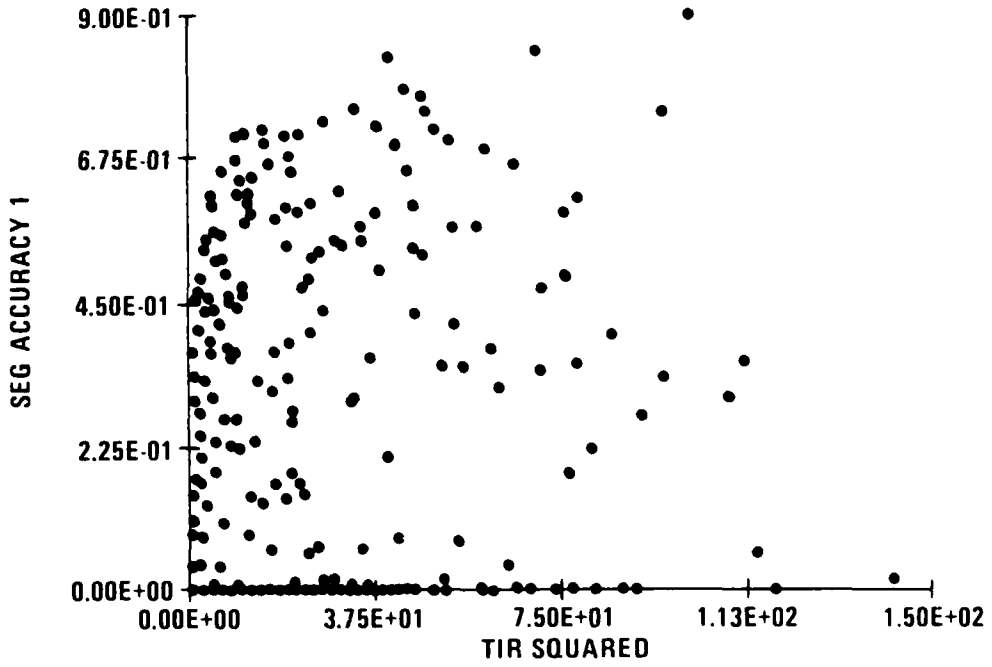

Figure 4-27. Variation of Segmentation Accuracy as a Function of TIR^2 for $TIR^2 \leq 150$ for the Combined TI and 29-Palm Data Base

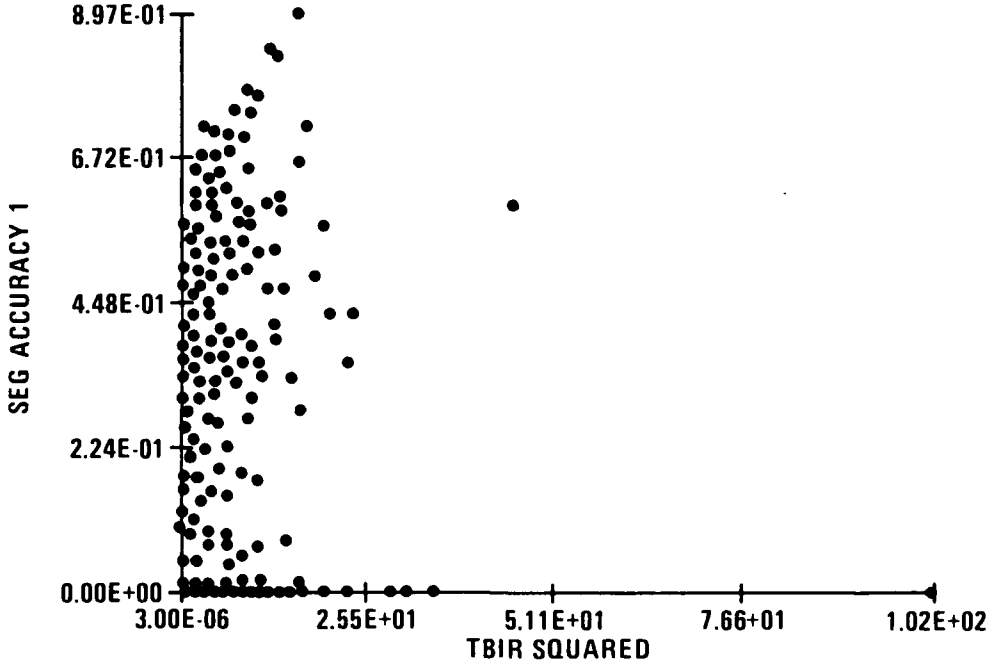

Figure 4-28. Variation of Segmentation Accuracy as a Function of $TBIR^2$ for Combined TI and 29-Palm Data Base

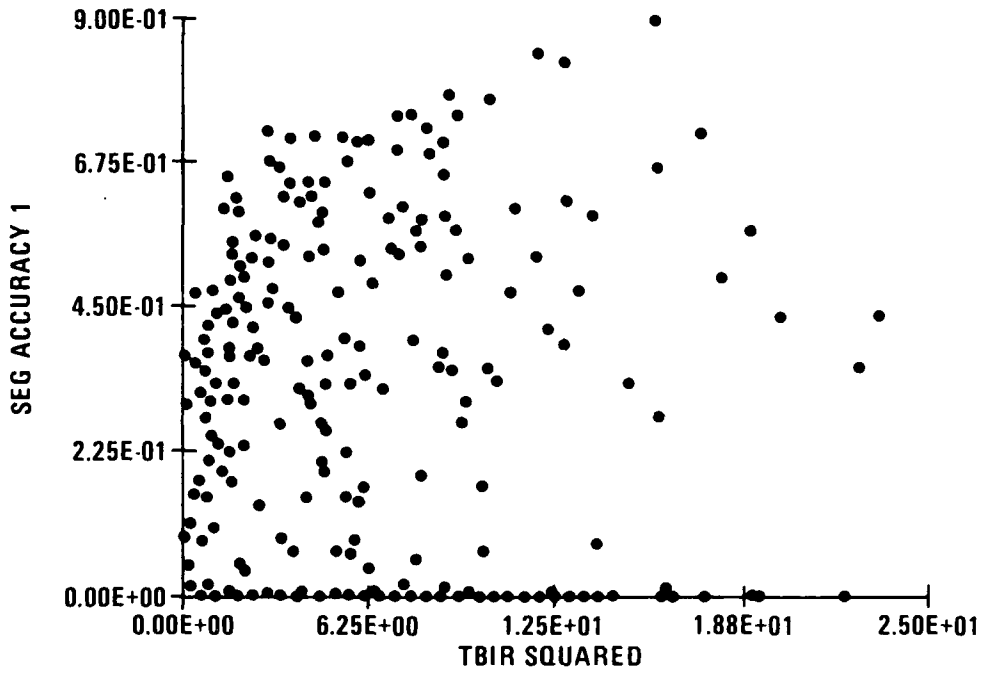

Figure 4-29. Variation of Segmentation Accuracy as a Function of $TBIR^2$ for $TBIR^2 \leq 25$ for the Combined TI and 29-Palm Data Base

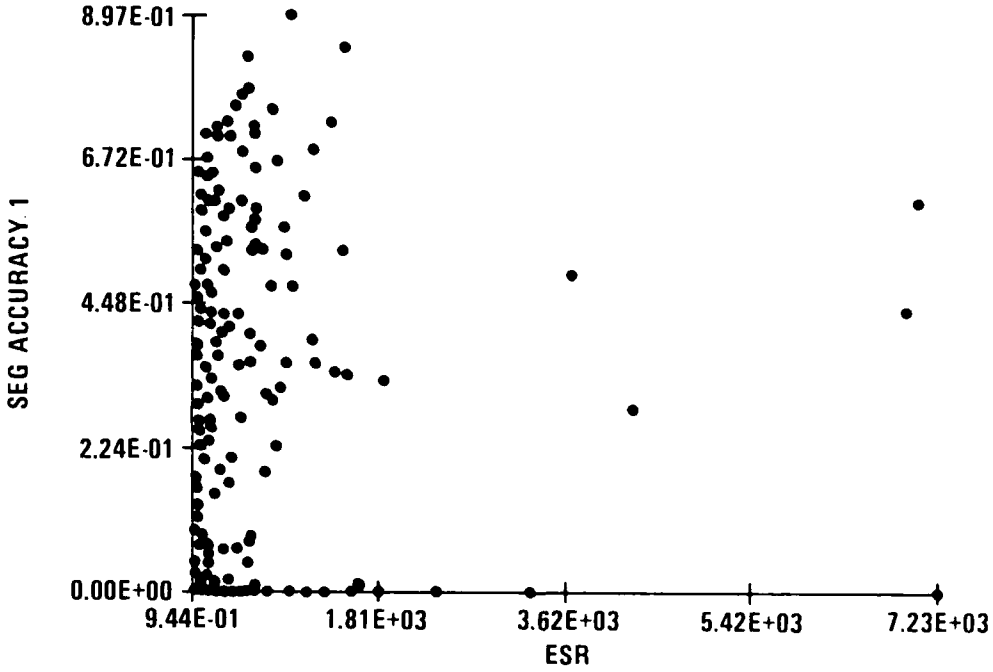

Figure 4-30. Variation of Segmentation Accuracy as a Function of ESR for the Combined TI and 29-Palm Data Base

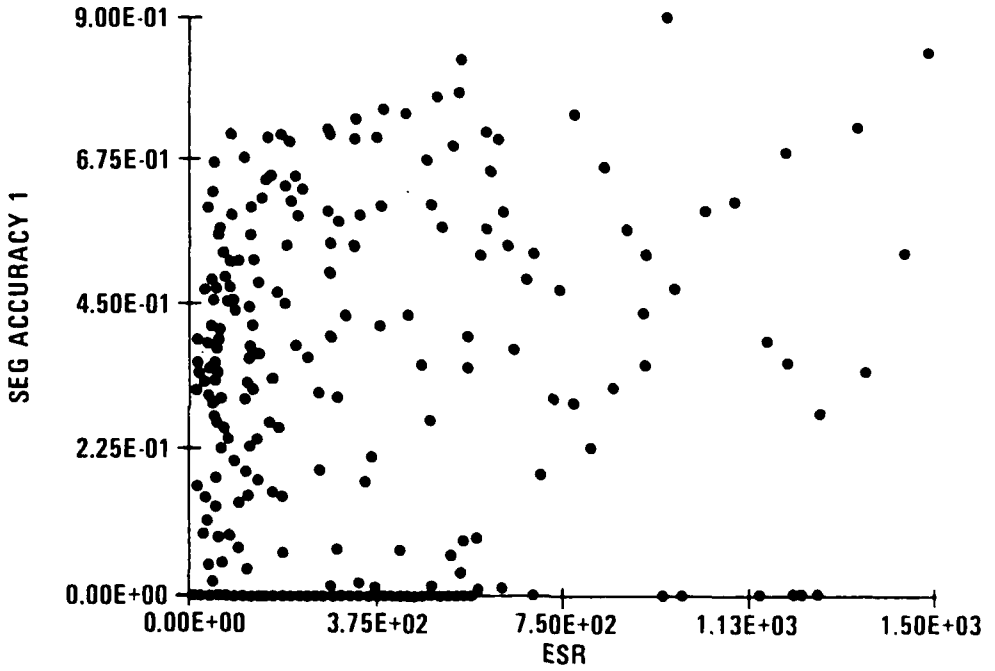

Figure 4-31. Variation of Segmentation Accuracy as a Function of ESR for ESR ≤ 1500 for the Combined TI and 29-Palm Data Base

4.5.4 SA vs. Range

Figure 4-32 shows the variation of SA as a function of range. SA attains its highest value of 0.897 at 5370 and then falls to around 0.7 at around 7000.

4.6 TBL's PROBABILITY OF POST-SEGMENT DETECTION VS. METRICS ON THE COMBINED TI AND 29-PALM DATA BASE

4.6.1 PD vs. TIR^2

Figure 4-33 shows the variation of P_D as a function of TIR^2. As TIR^2 increases P_D tends to increase and attain the value of 1 for most TIR^2 values higher than 350.

4.6.2 P_D vs. $TBIR^2$

Figure 4-34 shows the variation of P_D as a function of $TBIR^2$. As $TBIR^2$ increases P_D tends to increase. In the ranges of ($0 \le TBIR^2 \le 10$) the P_D average is 0.70 with a standard deviation of 0.21. For ($10 < TBIR^2 \le 20$), P_D has an average value of 0.56 and a standard deviation of 0.35. For ($20 < TBIR^2 \le 30$), P_D has an average value of 0.53 and a standard deviation of 0.50. For ($30 < TBIR^2 \le 110$), P_D has an average value of 0.5 and a standard deviation of 0.577.

4.6.3 P_D vs. ESR

Figure 4-35 shows the variation of P_D as a function of ESR. For values of ($0 \le ESR \le 50$), the average value of P_D was 0.61 and the standard deviation of 0.32. For values of ($50 < ESR \le 100$), the average value of P_D was 0.91 and a standard deviation was 0.12. For ($100 < ESR \le 1500$), the average value of P_D was 0.67 with the standard deviation of 0.4. For values of ($500 < ESR \le 7200$), the average P_D was 0.6 and the standard deviation was 0.459.

4.6.4 P_D vs. Range

Figure 4-36 shows the variation of P_D as a function of range. Worst P_Ds occur at the 9800 range. P_D has the maximum value of 0.53 at ranges between 1400 to 2100, P_D has a maximum of 1 and a minimum of around 0.66.

4.6.5 P_D vs. False Alarm Range for TBL

Figure 4-37 shows the variation of P_D per frame as a function of false alarm rate (FAR) performance. The numbers inside the parentheses are the numbers of samples having the same position on the graph. As can be seen, a large

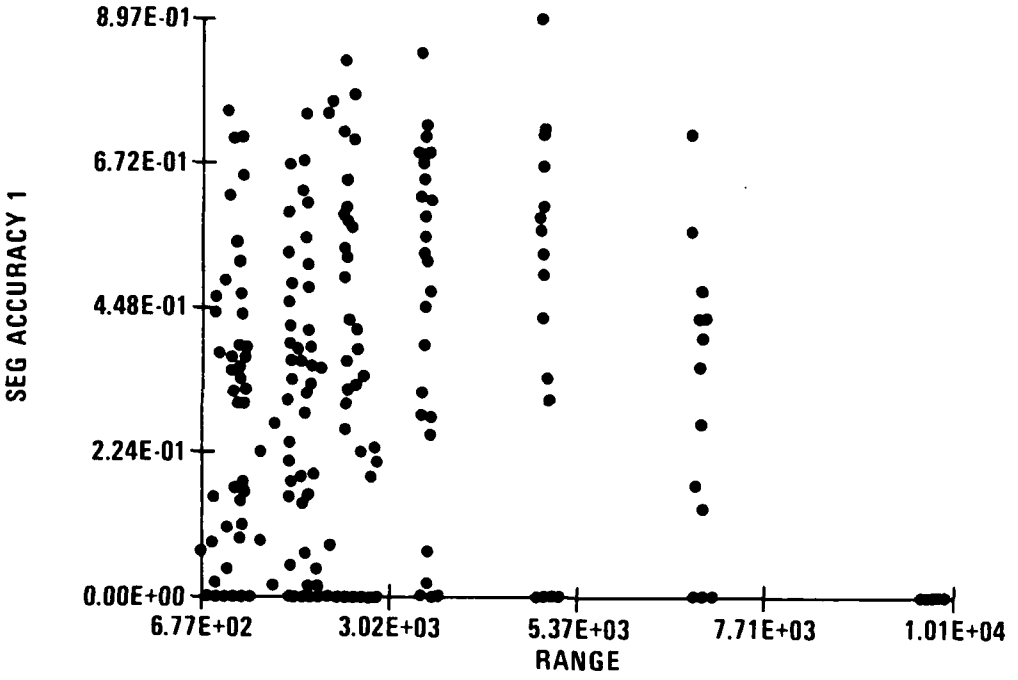

Figure 4-32. Variation of Segmentation Accuracy as a Function of Range for the Combined TI and 29-Palm Data Base

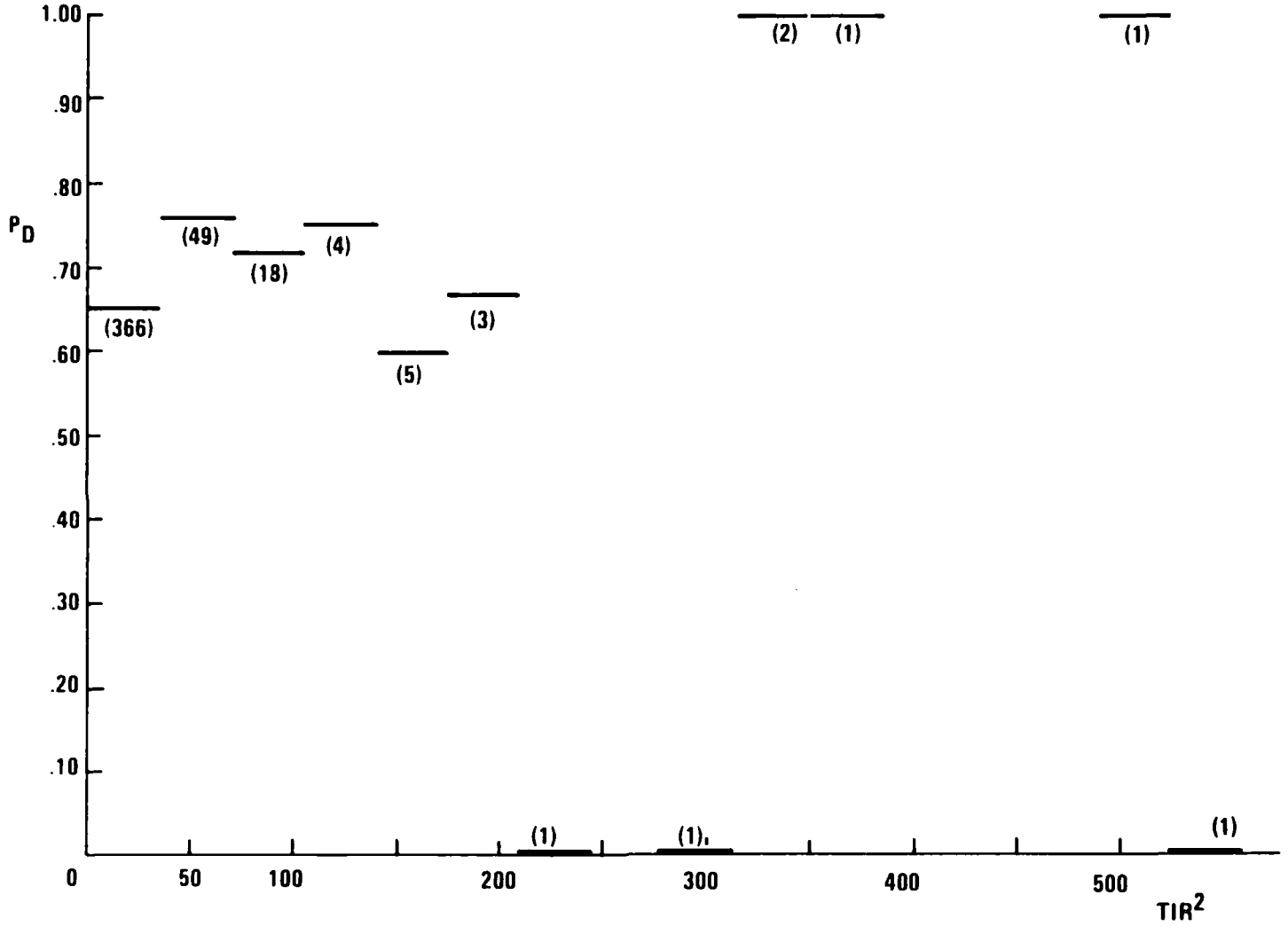

Figure 4-33. Variation of P_D as a Function of TIR^2 for the Combined TI and 29-Palm Data Base

87-CRG-574

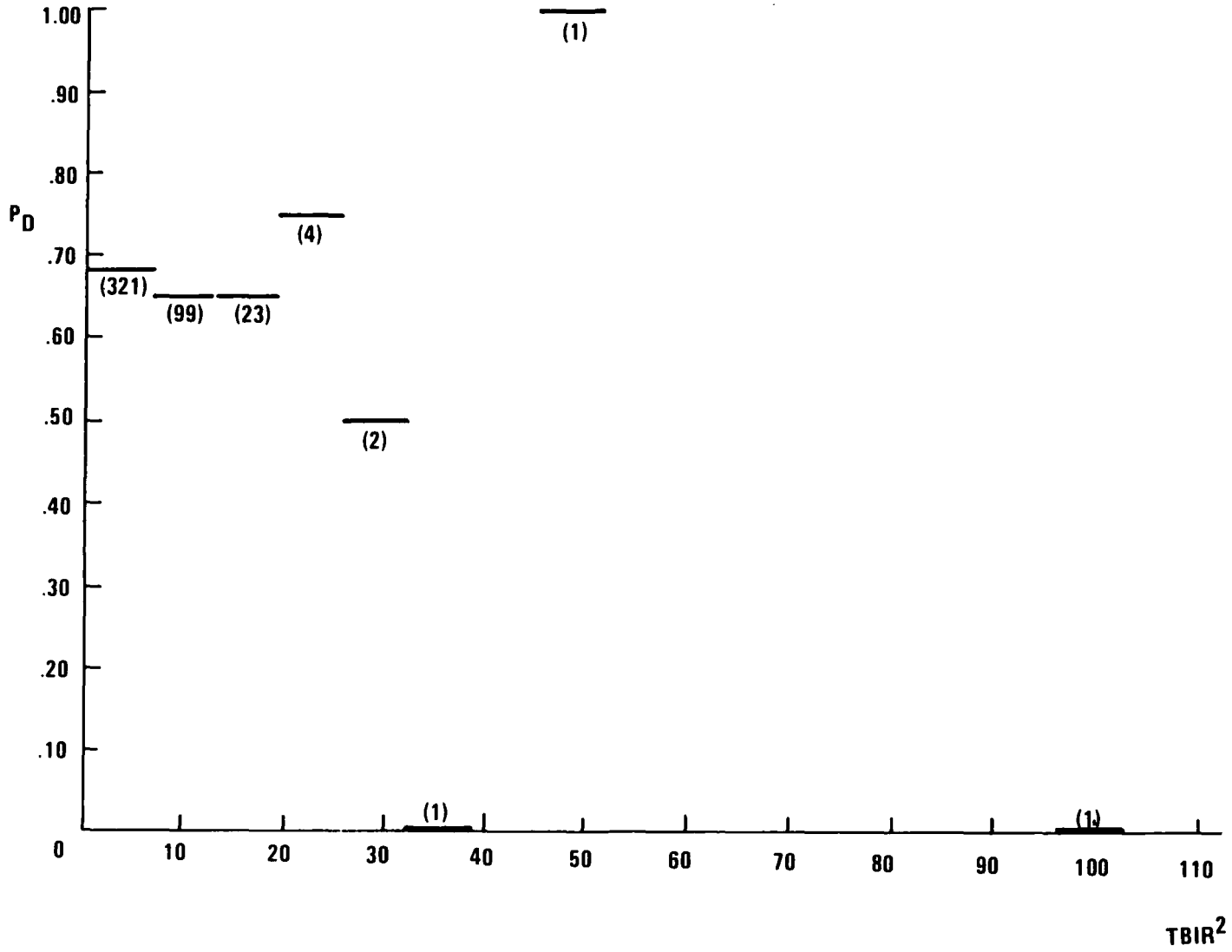

Figure 4-34. Variation of P_D as a Function of $TBIR^2$ for the Combined TI and 29-Palm Data Base

87-CRG-578

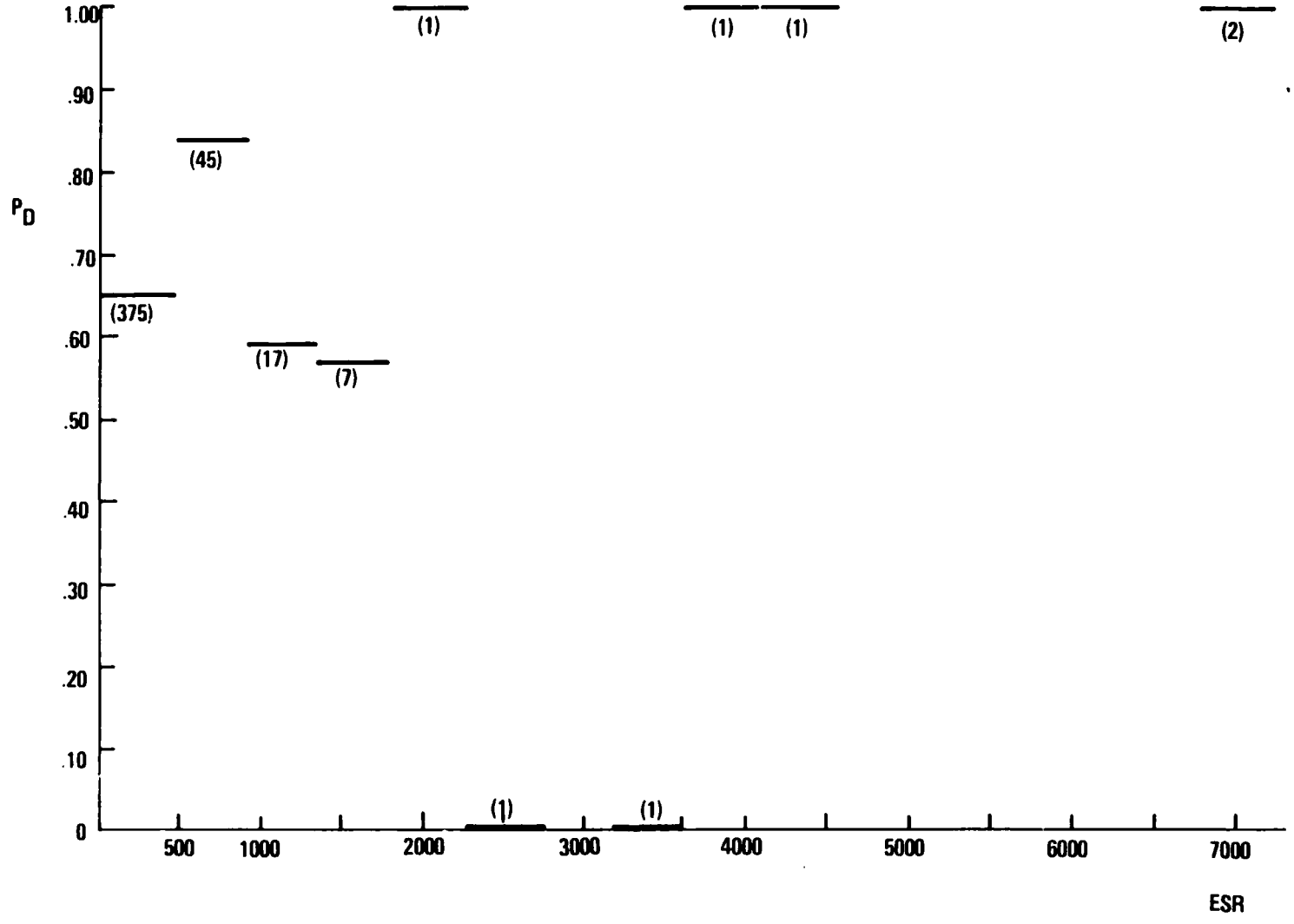

Figure 4-35. Variation of P_D as a Function of ESR for the Combined TI and 29-Palm Data Base

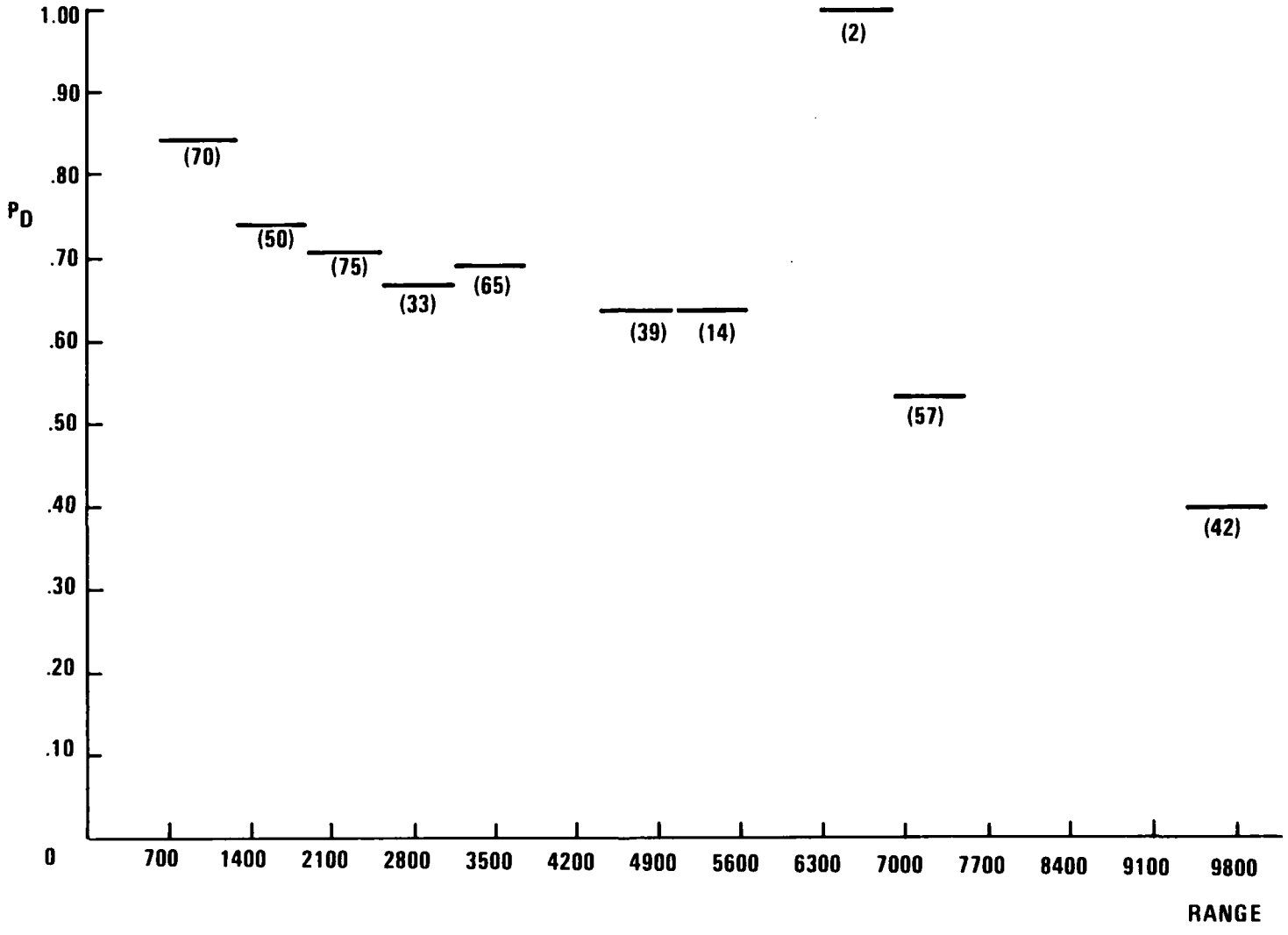

Figure 4-36. Variation of P_D as a Function of Range for the Combined TI and 29-Palm Data Base

87-CRG-586

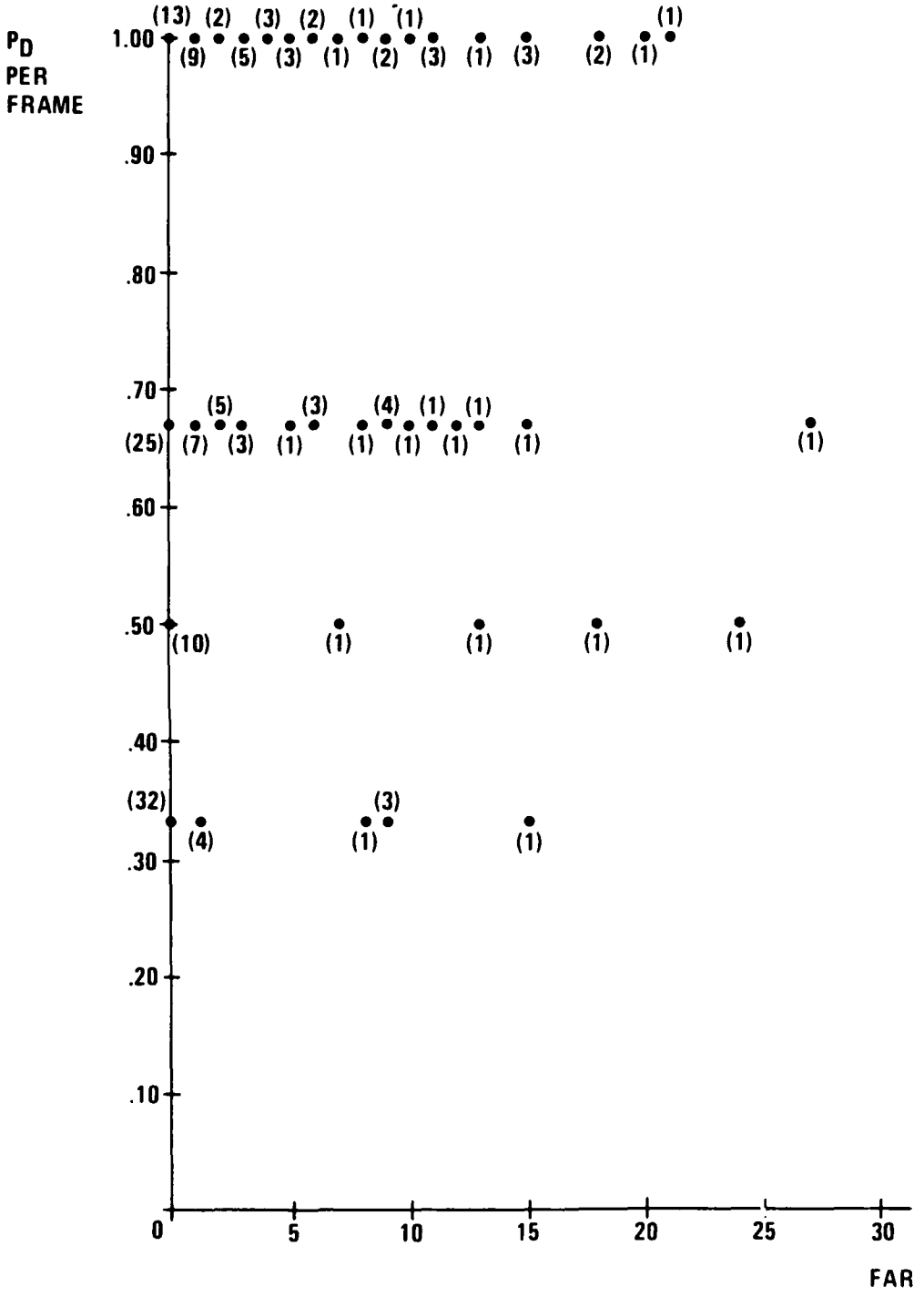

Figure 4-37. Variation of P_D per Frame as a Function of FAR per Frame for the Combined TI and 29-Palm Data Base

number of samples (53) have their P_D equal to 1. A total of 54 samples have P_D values around 0.67. The rest of the 55 samples have P_D values of 0.5 or smaller.

Figure 4-38 shows the variations of P_D per frame range coded: each sample is specified as to its range value. For P_D>0.90 and FAR<5, the samples of short range 625 to 1250 dominate. The following list shows the range values and their corresponding code name:

A = 625 - 1250	F = 3751 - 4375	K = 6875 - 7500
B = 1251 - 1875	G = 4376 - 5000	L = 7501 - 8125
C = 1876 - 1875	H = 5001 - 5625	M = 8126 - 8750
D = 2501 - 3125	I = 5626 - 6250	N = 8751 - 9375
E = 3126 - 3750	J = 6251 - 6875	O = 9375 - 10,000

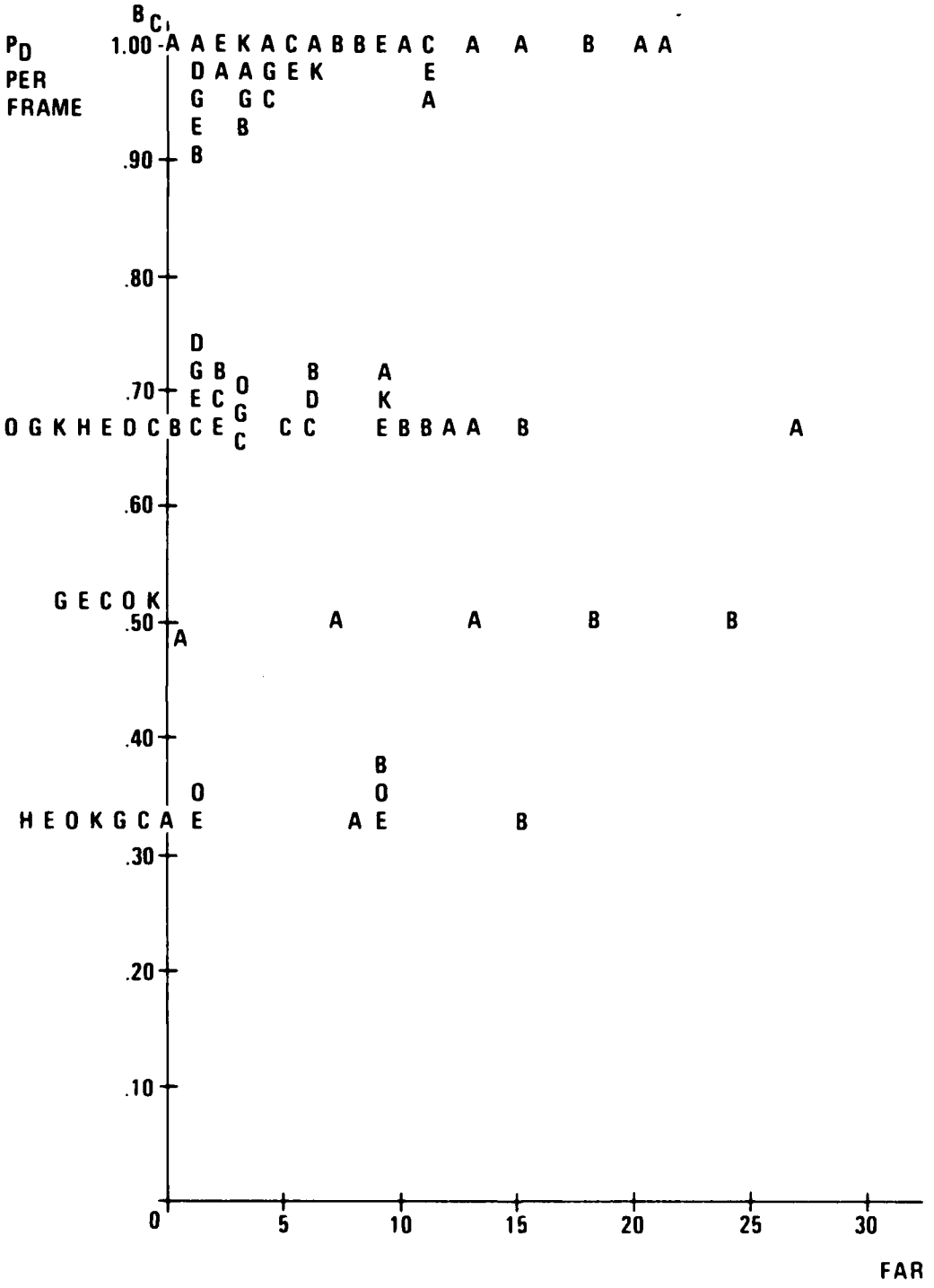

Figure 4-38. Variation of P_D per Frame as a Function of FAR per Frame, Range Coded, on the Combined TI and 29-Palm Data Base

SECTION 5

COMPARISON OF TBL AND BACORE

The objective of this task was to compare the performances of the BACORE and TBL on the same data base (29-palm and TI) and the same number of frames. In our comparison, 163 frames for both BACORE and for TBL were used. The division of frames was: 135 frames of TI data for each case, and 28 frames 29-palm data for each case.

Table 5-1 shows the results of the comparison of the average segmentation accuracy, probability of post segment detection, and false alarm rate per frame for the two algorithms. TBL performance in almost every aspect lags the BACORE performance. Table 5-2 shows the results for the TI data base and Table 5-3 show the 29-palm results.

Table 5-2 shows that BACORE has higher SA, higher P_D. However, for this data base FAR was lower for TBL than BACORE.

Table 5-3 shows that segmentation accuracy for BACORE was lower than the corresponding value for the TBL on the 29-palm data base. PD values for the two algorithms are similar. However, FAR was extremely higher for TBL (almost 6 times) than the corresponding value for BACORE at the output of the clutter rejection.

Overall BACORE outperforms TBL, even though the strength of BACORE is in multi-frame processing and not in single-frame processing.

Table 5-4 shows a comparison of TBL, BACORE single-frame, and BACORE multi-frame processors. The BACORE multi-frame processor is seen to outperform to a much higher degree the performances of TBL and single frame BACORE, especially in the area of FAR. It should be noted, however, that the data base used for multi-frame BACORE was different from those of the others.

TABLE 5-1. COMPARISON OF BACORE AND TBL ON COMBINED TI AND 29-PALM DATA BASE

	BACORE–Single Frame	TBL
SA (mean, standard deviation)	.37, .24	.35, .24
P_D	P_D (ROI) = .907 P_D (post segment) = .847 P_D (post segment and clutter rejection) = .518	P_D (post segment) = .66
FAR/frame	FAR (ROI) = 26.16 FAR (post segment) = 13.27 FAR (post segment and clutter rejection) = 2.87	FAR (post segment) = 3.44
No. of Frames Used	163	163
No. of Targets Used	488	448

87-CRG-478

TABLE 5-2. COMPARISON OF TBL AND BACORE ON THE TI DATA BASE

	BACORE	TBL
SA (mean, standard deviation)	.39, .24	.37, .31
P_D	P_D (ROI) = .923 P_D (post segment) = .872 P_D (post segment and clutter rejection) = .620	P_D (post segment) = .649
FAR/frame	FAR (ROI) = 19.14 FAR (post segment) = 9.80 FAR (post segment and clutter rejection) = 2.88	FAR (post segment) = 1.71
No. of Frames Used	135	135
No. of Targets Used	372	372

87-CRG-479

TABLE 5-3. COMPARISON OF TBL AND BACORE ON THE 29-PALM DATA BASE

	BACORE	TBL
SA (mean, standard deviation)	.27, .21	.32, .18
P_D	P_D (ROI) = .829 P_D (post segment) = .724 P_D (post segment and clutter rejection) = .013	P_D (post segment) = .750
FAR/frame	FAR (ROI) = 60 FAR (post segment) = 30 FAR (post segment and clutter rejection) = 2.77	FAR (post segment) = 17.5
No. of Frames Used	28	28
No. of Targets Used	76	76

87-CRG-480

TABLE 5-4. COMPARISON OF TBL, BACORE SINGLE-FRAME, AND BACORE MULTI-FRAME

	BACORE–Single Frame	BACORE–Multiple Frame	TBL
SA (mean, standard deviation)	.37, .24	.68, .38	.35, .24
P_D (segment P_D)	Before clutter rejection .84 After clutter rejection .518	P_D = .72 (after clutter rejection)	.66
FAR (segment FAR)	After clutter rejection .28/frame	1.34/frame (after clutter rejection)	3.44/frame
No. of Frames Used	163	120	163
No. of Targets Used	448	700	448

87 CRG 481

SECTION 6

TEST EXPERIMENTS FOR BACORE SEGMENTATION AND DETECTION ALGORITHMS

As an important part of the PAIRSTECH Project, we used two data bases that were supplied by ERIM (see Section 2.3) to test the detection and segmentation modules of BACORE.

6.1 DETECTION TEST EXPERIMENTS

We ran our BACORE detector on a total of 200 frames of unground truthed images. We mailed the detected regions of interest (ROIs) to ERIM as required.

Honeywell's MTAP is an integrated system that, when broken into isolated parts, may produce suboptimum results. In our integrated system, for the purpose of having high P_D, we allow a large number of false alarms that will be dealt with at the intermediate level and higher levels. However, this fact is not transparent at the end of the detection modules. Consequently, we anticipate that, for our detection algorithm, FAR will be relatively very high.

The detection experiment was done at five different ranges. A total of 1000 runs were made.

6.2 SEGMENTATION TEST EXPERIMENT

ERIM supplied us with four or five different ROI detection seeds per frame to be used on 200 frames of unground truthed data. The experiment was done at five different ranges for each frame. This experiment presented some difficulties for the BACORE segmentor. This is an integrated system; the result of separating the segmentor from the detector was unpredictable and potentially could lead to nonoptimum performance results. For example, the BACORE uses the ROI region, obtained from the detector, at the last stage of the segmentation to separate clutter from the true target regions. This is done by keeping only those regions whose overlap area with the ROI is not zero. Since, for the test experiment, the ROI consists of only one single point, the output of the segmentation, in many cases, tended to be zero, simply because of the large possibility that exists for the seed to be nonoverlapping with the segmented region, especially in bimodal targets. Removing the last stage of the segmentation, however, can potentially lead to the admittance of some clutter regions. We used this last step occasionally in our test experiment. The segmented images were put in proper formats and mailed to ERIM for their evaluation.

The results of the evaluation of the detection and segmentation test experiment are not available yet and will be published by ERIM at a later time.

SECTION 7

CONCLUSION AND SUMMARY OF RESULTS

In this study we investigated the detection and segmentation performances of Honeywell BACORE and TBL algorithms. The measures of performance were probability of detection (P_D), false-alarm rate (FAR), and segmentation accuracy (SA).

As part of this study we characterized and ground truthed six sequences of multi-frame sequential data. The image characterization was in the form of evaluating them in terms of several image metrics, among them the TIR^2, $TBIR^2$ and ESR. ERIM supplied us with ground truthed and similarly characterized single frame data.

All of the performance measures were tabulated in terms of the image metrics for a total of 163 frames and 448 targets for the single-frame evaluations. For the multi-frame evaluations a total of 120 frames containing 700 targets were used. For BACORE multi-frame, seven models were generated relating the performance measures to the TIR^2, $TBIR^2$, ESR and range metrics. These models are to be used in performance prediction.

The results of the study show that the performance of both BACORE and TBL on single-frame data is relatively similar, with BACORE performing mostly better than TBL. Segmentation accuracy values of both TBL and BACORE single-frame were relatively low, smaller than 0.4. This was partly due to the inadequate way the ATRWG measures of segmentation performance are defined and partly due to the way the ground truth data were prepared by ERIM. In the ERIM ground truth data base, targets were represented by a wire-frame model with no consideration paid to their thermal characteristics.

The study showed that there were not significant correlations between TIR^2, $TBIR^2$, and ESR and the performance measures of BACORE and TBL. Moreover, most of the imagery were clustered around low values of TIR^2, and $TBIR^2$ and this made the study meaningful only for a small region of metric space.

The study showed that generally, as TIR^2, $TBIR^2$ and ESR increase, at least in t he lower domains of metric space, performance measures increase. However, for higher domains of metric space, the behavior of algorithms was different. This is partly due to the lack of sufficient data in this domain and consequently relying on few samples.

The study of multi-frame BACORE showed a marked improvement in performance over single-frame BACORE. This study also showed the significance of the clutter rejection module in the BACORE algorithm for reducing FAR. On every data base that we used, clutter rejection reduced FAR by almost four to six times. However, this was accompanied by reduction in the values of the detection probabilities.

As part of this study, we gained significant insight into the BACORE and TBL algorithm parameter selection. For BACORE, the number of parameters that had significance on performance measures found to be nine out of a total of 18. For TBL, the three parameters were found to be functions of the image metrics and were set to provide optimum quantitative performance.

Setting of the parameters of algorithms was found to be crucial in the overall performance of both TBL and BACORE. In particular, our sensitivity studies of TBL showed that, in any cases, performance measures are very sensitive to the values of the algorithm parameters.

REFERENCE

1. Honeywell Systems and Research Center, "Bandwidth Reduction Intelligent Target Tracker (BRITT) Demonstrator," second quarterly report, March 1985.

END

FILMED

MARCH, 1988

DTIC